Noble Gases as Mean Ocean Temperature Proxies in Preindustrial and Last Glacial Maximum Simulations

Master Thesis
Faculty of Science
Universität Bern

Zhijun Liu

2021

Supervisor
Prof. Dr. T. F. Stocker
University of Bern, Climate and Environmental Physics

Acknowledgements

My deepest gratitude goes to my supervisor, Professor Thomas F. Stocker, who provided me with this great research opportunity and led me into the field of climate modelling. He has been a truly inspiring supervisor, providing rich research ideas and encouraging me to explore them all along the project. He has always been there to provide thoughtful feedbacks on my results and writing, and also greatly supported me in my career planning.

My special and great thanks go to Dr. Frerk Pöppelmeier, for his great patience in advising me and generosity in sharing his knowledge and ideas unreservedly. The discussions with and feedbacks from him were invaluable in formulating the research questions and the final thesis.

I would like to thank everyone at office 014 and 015 of the Climate and Environmental Physics (CEP) division, for creating a lovely working environment with many joyful memories. They have offered me many technical supports, valuable advices and all sorts of help. I want to specially thank Jeemijn Scheen, Dr. Aurich Jeltsch-Thömmes and Professor Fortunat Joos. I would like to thank the kind ice-core experimentalists, Prof. Hubertus Fischer, Dr. Daniel Baggenstos, Markus von Grimmer and Lucas Borges da Silva, who were always willing to share their knowledges and work on ice core measurements, and providing helpful insights.

I would like to extend my gratitude to everyone I have worked with at the CEP and the Oeschger Centre for Climate Change Research (OCCR). They have helped me in various ways, be it academic, technical, administrative or personal. It has been a great pleasure to work with them and I thank them for all the lovely time of seminars, workday break and aperos.

Last but not least, I would like to thank my friends and family for their support to my past study and continuation into future study. I want to specially thank Sidharth Sivaraj, my flatmate and batchmate at the OCCR, for his great support during the past two years.

It had been an unforgettable year of research experience and it was much more than academic knowledge that I have gained during this year. I could not have asked for a better environment for my master study than what I had here.

Abstract

The global mean ocean temperature (MOT) is an important measure for the state of Earth climate as it reflects the global energy balance. The potential of using noble gases as MOT proxies in was seen due to their unique properties: they are chemically inert and their solubility is temperature-dependent. The solubility of noble gases in seawater decreases with increasing ocean temperature, and thus a lower MOT should result in a lower atmospheric inventory. This change can be measured in the noble gas mixing ratios from air bubbles trapped in ice cores.

This thesis aims to examine with the climate modelling approach the relation between the atmospheric Krypton mixing ratio anomaly ($\delta\mathrm{Kr}_{atm}$) and the MOT anomaly (ΔMOT) under various boundary conditions. Sensitivity tests were performed with the Bern3D 2.0 Earth system model of intermediate complexity, which allows simulations to run on multi-millennial time-scale. Different boundary conditions were achieved by varying atmospheric CO_2 concentration, diapycnal diffusivity and wind stress. A new 5-box model was developed to further understand some results from the Bern3D model in a highly simplified setting.

Simulation results show that two factors, the sea ice and the state of the Atlantic Meridional Overturning Circulation (AMOC), have influence on noble gases responses to MOT change via air-sea gas exchange. Depending on the dominant factor in each simulation, $\delta\mathrm{Kr}_{atm}$'s response to MOT change can be divided into three regimes.

In simulations with ΔMOT>1.3°C, very little or zero sea ice exists in the Southern Ocean, resulting in a global mean Kr saturation ratio of higher than 98.5%. $\delta\mathrm{Kr}_{atm}$ holds a relation with the MOT signal as directly calculated from the temperature-dependent solubility equation.

In the second regime where ΔMOT<1.3°C, the impact of sea ice becomes non-negligible on the $\delta\mathrm{Kr}_{atm}/\Delta$MOT relation. By blocking surface air-sea gas exchange, sea ice over the Antarctic Bottom Water (AABW) formation region can result in undersaturation in the deep ocean. This decouples $\delta\mathrm{Kr}_{atm}$ from deep ocean temperature, and hence from the MOT signal. The global mean Kr saturation ratio decreases proportionally as sea ice expands over the Southern Ocean. Once the Southern Ocean is fully covered by sea ice, global mean Kr saturation ration remains stable even when sea ice expands further in other regions.

Sensitivity tests in both the Bern3D 2.0 model and the new 5-box model show that $\delta\mathrm{Kr}_{atm}$ responds non-linearly to ice leak change. This justifies the omission of sea ice when converting ice-core measured $\delta\mathrm{Kr}_{atm}$ to MOT anomalies in current research. Although, this could lead to a constant offset of 0.1‰ to 0.2‰ in the expected $\delta\mathrm{Kr}_{atm}$ at a certain ΔMOT.

The third regime appears when AMOC is collapsed with wind stress lower than 70% of the control simulation. With sea ice over the Southern Ocean, a tropical-centralised surface heat distribution under weak wind stress leads to the result that only warm temperature signals are recorded by $\delta\mathrm{Kr}_{atm}$. As a result, $\delta\mathrm{Kr}_{atm}$ is further decoupled from the MOT signal.

While proxy studies suggest that a collapsed AMOC existed in the past, the Bern3D 2.0 model was not able to reproduce it in LGM conditions, neither has there been strong disagreement between the current noble gas reconstructed MOT records and other temperature proxy reconstructions. Overall, noble gases can be used as reliable proxies for the past 800 kyr MOT reconstructions, although sea ice may cause small deficit by partially blocking the air-sea gas exchange and generating undersaturation. Rare situations are discussed when proxy reliability is compromised by shutdown of AMOC.

Contents

1 Introduction

Studying the past is crucial for understanding the present and future climate on the Earth. The measurements and modelling of the past climate help to quantitatively understand how the Earth system responds to various climate forcings (Masson-Delmotte et al., 2013) and hence improve future projections. Climate variations on the Earth are determined by the planetary radiative imbalance between incoming solar radiation and outgoing radiation emitted by the planet. According to the conservation law of energy, the net radiation flux at the top of the atmosphere is equal to the sum of the rate of change of the heat content of all heat reservoirs on the Earth (Baggenstos et al., 2019). To obtain an overall picture of the climate state at a past period, it is central to understand the heat content changes of all major climate system components.

The ocean as a major heat reservoir of the Earth system has absorbed over 90% of the excess heat induced from human activities (Masson-Delmotte et al., 2021). The global mean temperature of the ocean is an important quantity in climate as it reflects the global ocean heat content (Bereiter et al., 2018b). A reliable paleo-reconstruction of the global mean ocean temperature (MOT) provides a quantitative estimate on the past global radiative balance.

Multiple efforts have been made on obtaining direct measurements of the ocean temperature, from the nineteenth-century Challenger expedition to the more recent Argo float array project (Gleckler et al., 2016). Due to formidable technical challenges, records from the deep ocean (below 2,000 m depth) and measurements before the twentieth century are sparse, generating uncertainties in the MOT estimates (Roemmich et al., 2015; Gleckler et al., 2016). The large volume of oceans and the heterogeneity of temperature inside them make it impractical to obtain the global MOT from direct measurements precisely (Haeberli et al., 2020).

Many proxies have been proposed for the paleoclimatic reconstruction of the ocean temperature, for instance, the ratio of magnesium to calcium in benthic foraminiferal species (Bryan and Marchitto, 2008), heavy oxygen isotope content of fossils or carbonate rocks, and Sr to Ca ratio in the corals (Lea, 2014). However, these proxies carry strong local temperature signals instead of representing the global mean and also involve chemical and biological processes that are not fully understood yet (Ritz et al., 2011). It is therefore necessary to have a reliable proxy with only physical processes involved representing the global mean temperature.

Given the inert nature of noble gases, Headly and Severinghaus (2007) first suggested the potential of using $\delta Kr/N_2$ measured from air bubbles trapped in the ice cores as the proxy to reconstruct the MOT during the Last Glacial Maximum (LGM). Owing to the similarities in their chemical properties, $\delta Ar/N_2$ and $\delta Xe/N_2$ have also been used as MOT proxies in later research. The validity of using these noble gas mixing ratios to infer MOT in paleo-reconstructions have been examined in both ice core measurements and Earth system modelling studies (Ritz et al., 2011; Bereiter et al., 2018a,b; Shackleton et al., 2019; Haeberli et al., 2020).

Reconstruction of the MOT during glacial-interglacial cycles is particularly important because of the on-going debate about the extent of anthropogenic impacts on the climate system. This requires us to have a better understanding on the extent, rate, and frequency of climate changes before human activities exerted an non-negligible influence (Mix et al., 2001). There are only limited and discrete MOT records from recent-year noble gas reconstructions, and the Last Glacial Maximum (LGM) period has been most commonly

measured. In this thesis, noble gas and climate state during LGM are studied as an example of the proxy reliability in glacial period climate.

In this project, dynamics of noble gases are simulated in an intermediate complexity climate model and a box-model. The aim is to observe noble gas proxies responses to different boundary conditions, and thus obtain a better understanding on mechanisms and factors that could potentially affect the reliability of noble gases as MOT proxies. The first section of this thesis introduces the background theory and applications of noble gases as MOT proxies in ice core studies. In the second section, two climate models, the Bern3D 2.0 model and a newly formulated 5-box model, used to run simulations are described. In the result section, dynamics of noble gases in the climate system is explained with results from the two models. From sensitivity test results, the impacts of sea ice and ocean circulation state are further analysed. Moreover, modelled LGM simulations are compared with ice-core LGM reconstructions to understand the difference between modelling and measurement, and to determine the applicability of modelling studies on interpreting measurement bias. Finally, based on these results analysis and discussion, the reliability of noble gases as MOT proxies is discussed.

2 Theory and Background

2.1 The Ocean

The oceans cover around 71% of the surface area of the Earth (Talley et al., 2011) with a volume of 1.34×10^{18} m^3 (Stocker, 2013). Together with the high heat capacity of water, these enable the ocean to store and transport large amounts of heat, water and carbon, and thus influences climate through the air-sea exchange of these properties (Rhein et al., 2013).

The global ocean circulation consists of two main parts: the wind-driven circulation dominating the surface ocean and the density-driven thermohaline circulation dominating the deep ocean (Stockli et al., 2008). Surface ocean with divergent currents have upwelling water masses and convergent regions have downwelling water, which links the surface and deep ocean. In the deep ocean, the large and slow (1000-year scale) thermohaline circulation drives a global-scale current system (Fig. 1), namely 'the global conveyor belt' (National Oceanic and Atmospheric Administration, 2021).

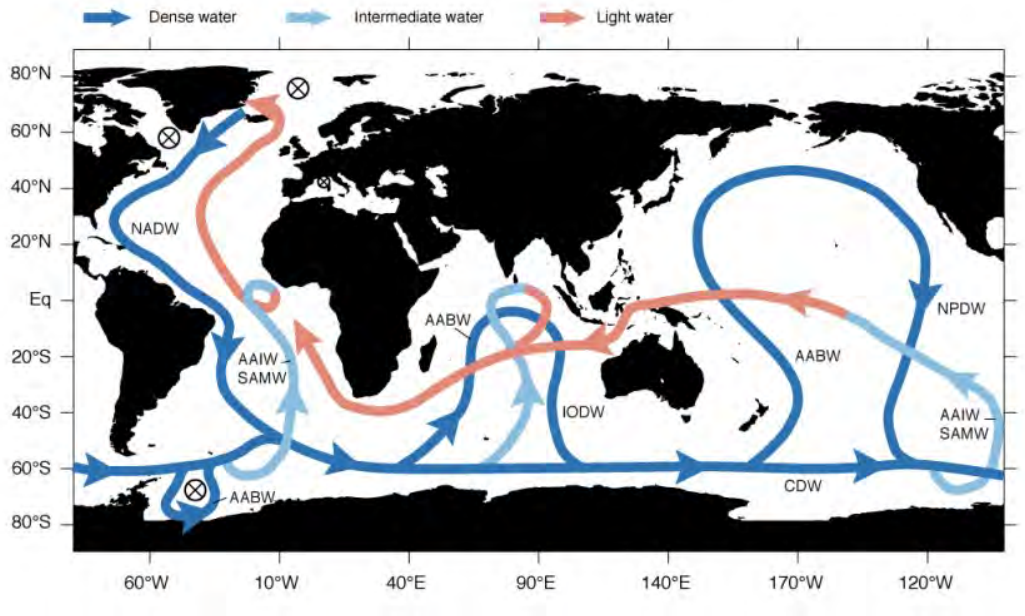

Figure 1: A simplified conceptual schematic of global thermohaline circulation. Crosses in circles indicate the regions of deep water formation. AABW: Antarctic Bottom Water. AAIW: Antarctic Intermediate Water. SAMW: Subantarctic Mode Water. NADW: North Atlantic Deep Water. NPDW: North Pacific Deep Water. IODW: Indian Ocean Deep Water. CDW: Circumpolar Deep Water (Sarmiento and Gruber, 2006).

The conveyor belt starts with warm surface water losing heat to the polar atmosphere around the Nordic Seas and Labrador Sea, and becoming dense cold water, which sinks to the deep ocean. This process describes the formation of the North Atlantic Deep Water (NADW), which is the most salient feature of the conveyor belt due to its huge impact on the Atlantic climate (Broecker, 1991). As the cold water flows southward in the deep ocean to make space for the continuously incoming water from the surface, this forms the Atlantic Meridional Overturning Circulation (AMOC). The AMOC transports massive amounts of water and heat from the tropical to the mid and high-latitudes in the Atlantic basin (Schmittner et al., 2007). This bottom water flows all the way south

and joins the Antarctic circumpolar current (ACC) at the Southern Ocean, where it gets mixed with different deep water masses which form the Circumpolar Deep Water (CDW). Some of the bottom water in the Antarctic further reaches into the Indian ocean and the Pacific. Eventually, these deep water masses rise to the surface ocean through mixing and upwelling (Schmittner et al., 2007).

Deep and bottom waters are mostly formed in two regions: NADW in the Northern Atlantic and AABW around the coast of Antarctica. The subduction in the North Atlantic is mainly caused by the heat loss to the atmosphere at the high latitudes, whereas the bottom water formation around Antarctica is more related to brine rejection (Schmittner et al., 2007). Brine rejection refers to a process in which salt is expelled when seawater reaches the freezing point and forms ice (Lake and Lewis, 1970). The difference in formation processes leads to the consequence that AABW is much fresher and colder compared to NADW (Schmittner et al., 2007). The formation of deep and bottom water lays an important role in determining the global MOT as it connects the surface ocean and the deep ocean, which takes up the majority of the global ocean volume.

2.2 Noble Gases

Noble gases refer to elements of group 18 in the periodic table. With the outermost electronic shells being completely filled, noble gases exhibit chemical inertness (Pan et al., 2013). Apart from Helium, which can escape from the Earth's gravity, and Radon, which is radioactive, the other four noble gases - Neon, Argon, Krypton and Xenon have no essential sinks or sources and therefore have conserved total inventories in the Earth system (Bereiter et al., 2018b). This constraint of the mass conservation of any specific noble gas can be expressed as

$$I_{tot} = I_{atm} + I_{ocn}, \tag{1}$$

where I_{atm} and I_{ocn} are their oceanic and atmospheric inventories. This equation also holds for nitrogen, as the change of N_2 inventories (nitrification and denitrification) in nature is negligible for the total inventories (Gruber, 2004; Schlesinger, 1997).

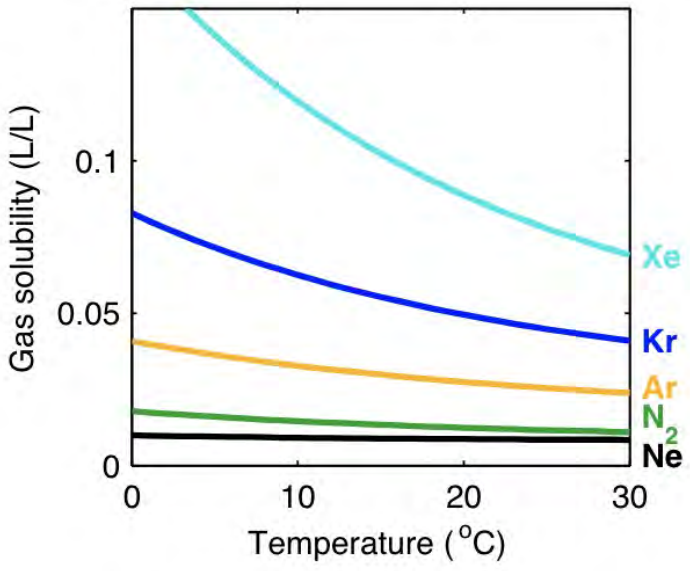

Figure 2: Noble gases temperature dependant solubility in seawater, solubilities in Bunsen coefficient (Hamme and Severinghaus, 2007).

Gases with heavier molecular weights are more soluble (Fig 2). The solubility of the lighter noble gas (Ne) responds relatively insensitively to temperature change, whereas solubilities of the heavier noble gases (Ar, Kr and Xe) in seawater exhibit strong and non-linear temperature dependencies (Wood and Caputi, 1966; Weiss and Kyser, 1978; Hamme and Emerson, 2004). Hereafter, in this thesis, the word 'noble gases' are used to refer to Ar, Kr and Xe.

Similar to noble gases, ocean temperature can also be seen as a passive tracer as there are no essential sinks or sources inside the ocean (Ritz et al., 2011). Heat change inside the ocean due to glacial meltwater or geothermal flux is negligible compared to the surface heat flux (Loose and Jenkins, 2014). This global net heat flux change at the air-sea interface is reflected in the change of MOT. This means any change in ocean heat content will induce heat fluxes at the surface and hence the signals will be recorded by noble gas exchange at the surface, and the internal transport of noble gases or temperature does not affect the proxy reliability.

Oceanic inventories of noble gases are not influenced by any biological or chemical processes and are only temperature dependent. Noble gases are more soluble in colder ocean, leading to lower atmospheric inventories. Conversely, when less noble gases get dissolved in warmer oceans, concentrations are higher in the atmosphere (Craig and Wiens, 1996).

The oceanic concentration C^* of gases is determined by the abundance in the atmosphere above the ocean surface and is governed by Henry's Law:

$$C^* = S \cdot p_a, \tag{2}$$

where S is the solubility in seawater and p_a the pressure of the atmosphere at sea surface. Since sea level pressure and ocean volume at a steady state can be considered to be constant, the oceanic abundances of noble gases and N_2 are proportional to their solubilities. According to Eq 1, their atmospheric abundances are negatively correlated.

It is impractical to measure the atmospheric inventory of noble gases directly. Instead, the mixing ratio of noble gases to N_2 was proposed (Bereiter et al., 2018b), as N_2 does not have a strong temperature dependence in solubility (Fig 2). The anomaly of the sample mixing ratio at a certain period to the reference value at pre-industrial time reflects the MOT anomaly between these two periods. The atmospheric Kr-to-N_2 mixing ratio anomaly is defined as (Headly and Severinghaus, 2007)

$$\delta Kr_{atm} = \left(\frac{(I^{Kr}_{atm}/I^{N_2}_{atm})_{sample}}{(I^{Kr}_{atm}/I^{N_2}_{atm})_{reference}} - 1 \right) \cdot 1000‰. \tag{3}$$

Similarly, mixing ratios of other noble gases (δXe/N_2, δAr/N_2 and δXe/Kr) can also be used as MOT proxies (Bereiter et al., 2018a). The temperature range that is of the concern for MOT reconstructions can be safely limited to below 10°C. In this low temperature range, Kr and Xe have higher solubilities in seawater and respond more sensitively to temperature changes than Ar (Stanley et al., 2009). For this reason, δKr/N_2, δXe/N_2 and δXe/Kr are more often used as MOT proxies than Ar mixing ratios. Considering the similarities between these noble gases, this thesis examines the reliability of noble gases by focusing on δKr/N_2 response to MOT changes.

Based on the relationship in Fig 2 of Kr solubility to temperature change below 10°C, δKr/N_2 to MOT anomaly is expected to also have a close-to-linear relation with MOT. However, this assumption is based on the prerequisite that surface ocean is always saturated with noble gases, so that the actual surface ocean concentration is equal to the

saturated concentration in theory under given conditions and records surface heat exchange faithfully. Mechanisms or factors that can lead to large volume of undersaturated or supersaturated water bodies could potentially compromise the reliability of noble gases being used as MOT proxies.

2.3 Ice Core Measurements

Polar ice cores is a powerful tool in retrieving past climate data. The use of ice cores in paleoclimate study was first proposed in 1950s by Willi Dansgaard (Winckler and Severinghaus, 2013). Currently the oldest ice core can trace back to 800,000 years ago (Lüthi et al., 2008), covering eight complete glacial-interglacial cycles.

In polar regions, snow keeps accumulating every year on the continental ice sheet, forming a permeable layer called firn (Fig 3). The firn layer is about 50-100m deep (Schwander, 1996), and it may take up to 3 kyr (1 kyr = 1000 years) before the air bubble enters the close-up depth (Winckler and Severinghaus, 2013).

The bubbles in the ice cores are essentially trapped air from the past and carry atmospheric information from that time (Winckler and Severinghaus, 2013). For ice cores from EPICA Dome C, the gas age is given according to AICC 2012 (Veres et al., 2013). For ice cores at WAIS Divide, the gas age is according to Sigl et al. (2019).

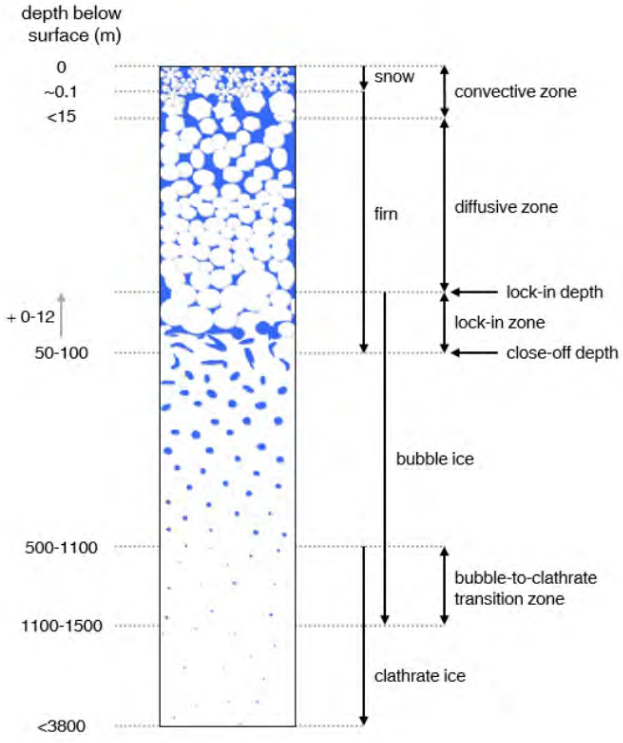

Figure 3: Vertical structure of the ice sheet. Schematic of the ice sheet where ice cores are drilled (Nehrbass-Ahles, 2017).

The timescale for mixing processes in the atmosphere is from about a few months to a year. Thus, due to the relatively fast atmospheric circulation, atmospheric noble gas concentrations integrate globally. This fast mixing of gas in the atmosphere in comparison to the relatively large gas age range makes noble gases good proxies with no delay or

further low-pass filtering behaviours (Bereiter et al., 2018b). And the time resolution of mixing ratio measurements from ice cores vary from 100 year to 1000 years (Bereiter et al., 2018b; Haeberli et al., 2020).

The LGM refers to the most recent interval when the ice sheets on Earth had the maximum extent (Clark et al., 2009), which was the period around 19 kyr to 21 kyr before the modern time (Masson-Delmotte et al., 2013). Recent ice-core studies show that MOT during LGM is around 2 to 4°C colder than during the Holocene (Bereiter et al., 2018a,b; Haeberli et al., 2020). Reconstructed LGM MOTs from different ice core samples are in general agreement, overlapping each other within their uncertainty ranges.

Headly and Severinghaus (2007) measured $\delta Kr/N_2$ in ice core samples from Greenland (GISP2). The MOT difference between LGM and today interpreted with a mass balance model is 2.7±0.6°C.

Bereiter et al. (2018b) measured noble gas concentrations trapped in the West Antarctic Ice Sheet (WAIS) Divide ice cores to establish an MOT record over 24 kyr. Based on $\delta Kr/N_2$, $\delta Xe/N_2$ and $\delta Xe/Kr$ measurements, the temperature change over the last glacial transition (20 kyr to 10 kyr BP) is –2.57±0.24°C.

Haeberli et al. (2020) measured noble gases from the European Project for Ice Coring in Antarctica (EPICA) Dome C ice cores and obtained an MOT record over the last 700 kyr. The MOT records reconstructed using $\delta Kr/N_2$, $\delta Xe/N_2$ and $\delta Xe/Kr$ ice core measurements are shown (Fig 4). The MOTs obtained from different noble gases are generally consistent, with higher consistency near present and more inconsistency in MOTs earlier than 300 kyr. The reconstructed LGM MOT anomalies are –2.9±0.4°C, –3.3±0.4°C and –3.6±0.4°C respectively, for $\delta Kr/N_2$, $\delta Xe/N_2$ and $\delta Xe/Kr$.

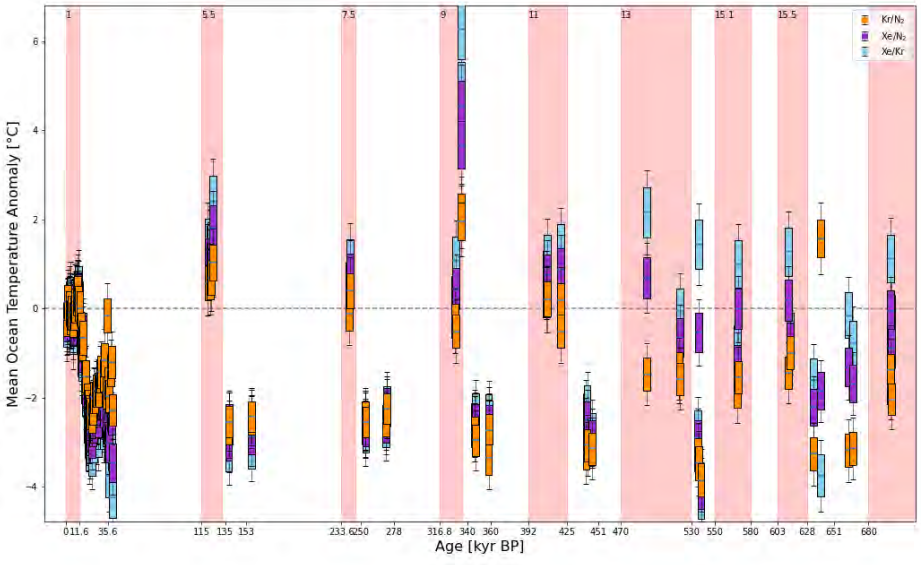

Figure 4: MOTs during glacial-interglacial cycles. Converted from noble gas mixing ratios trapped in EPICA Dome C ice cores (Haeberli et al., 2020).

An ocean-atmosphere 4-box model proposed by Bereiter et al. (2018b) has been most commonly used for converting Antarctic ice core noble gas mixing ratios to MOTs (Baggenstos et al., 2019; Shackleton et al., 2019; Haeberli et al., 2020). This model consists of four boxes: the atmosphere, AABW, NADW, and the rest as the residual ocean.

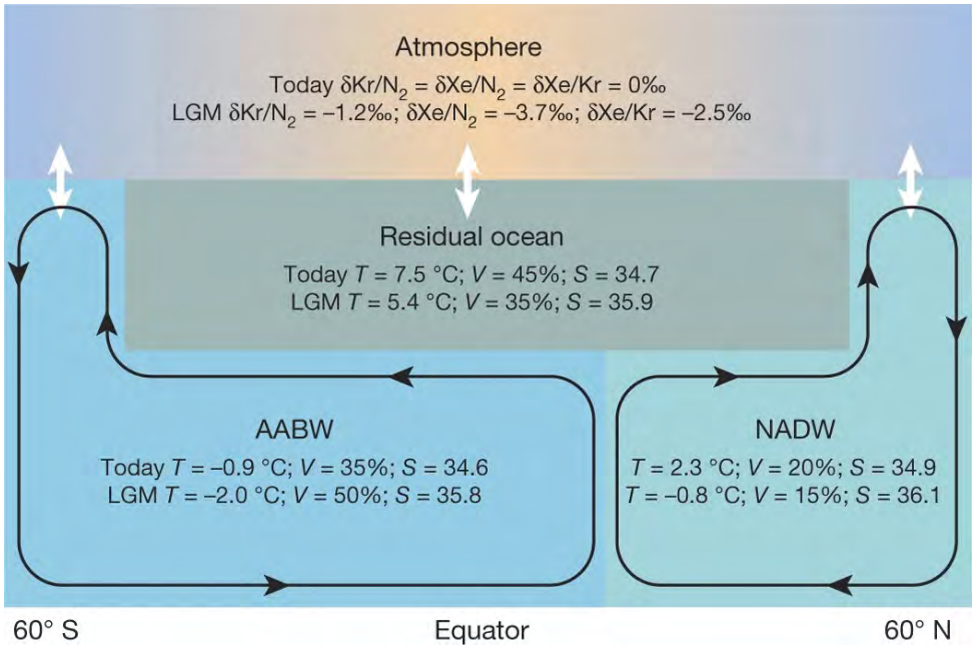

Figure 5: Schematics of the 4-box model with present day and LGM features. White arrows indicate the noble gas air-sea exchange (Bereiter et al., 2018b).

The 4-box model prescribed average values for the global ocean, with temperature T=3.53°C, salinity S=34.72 psu and total volume V=1.34 × 10^{18} m^3 (Bereiter et al., 2018b). The present day characteristics of AABW and NADW are set according to Johnson (2008). The residual ocean is set so that the total ocean budget is closed. The model is constrained by the mass conservation where the total masses of noble gas or N_2 in the ocean and the atmosphere is the same at present and at the LGM.

Given the sea level change, MOT and the volume of AABW as inputs, the 4-box model calculates the corresponding atmospheric mixing ratios of noble gases. 12,000 Monte Carlo MOT realisations were calculated for each gas (N_2, Kr, Xe). All 36,000 realisations were combined to one best-estimate MOT record to reduce uncertainties from the sea-level record, the degree of gas saturation, the firn thermal correction and analytical uncertainties.

Some factors that may have led to MOT uncertainties were discussed by Bereiter et al. (2018b), including changes induced by sea level change to ocean volume, salinity and sea surface pressure. Other factors including AABW salinity anomaly, gigantic floating ice shelf, and Xe solubility function correction were quantified but deemed to be negligible comparing to the overall uncertainty. The influence from sea ice is completely omitted in this model as its impact on dissolved Kr in ocean was thought to be overestimated in the study by Ritz et al. (2011) (Bereiter et al., 2018b). However, evidence is not strong enough to claim this impact is negligible and it is therefore questionable to completely exclude the sea ice from the model when interpreting proxy measurements.

Physical processes that could have an influence on the reliability of ice core noble gas mixing ratios include the air-sea gas exchange, the atmospheric mixing process, and the air-bubble formation in ice cores (Bereiter et al., 2018b). In this thesis, I focus on the possible deviation of noble gas to MOT relation that could occur during the air-sea gas exchange process by modelling the ocean circulation in the climate system.

3 Methods: A Hierarchy of Climate Models

Climate modelling is a powerful tool for understanding the Earth system and climate change. They are built on fundamental physical principles including conservation of mass, energy and momentum, and parameters are tunned to best fit observational data. Climate models have been proven to be able to produce observed climate features (Randall et al., 2007; Masson-Delmotte et al., 2013).

Many models have been developed for different needs. Atmosphere-Ocean General Circulation Models (AOGCMs) are considered to be comprehensive climate models suitable for climate projections at continental or larger spatial scales. However, AOGCM simulations are usually only run on multi-decadal scales due to their high dynamical complexity and computational cost (Randall et al., 2007). On the other side of the modelling spectrum are the conceptual models, which simulate the climate in highly simplified setups. They serve the purpose of qualitatively extending results from comprehensive models to a wider range of boundary conditions (Claussen et al., 2002).

The concept of Earth system models of intermediate complexity (EMICs) was developed in the 1990s to fill the gap between comprehensive and conceptual models on the hierarchy of climate models (Stocker et al., 1992). EMICs are models that are designed to include most processes of AOGCMs in a more parameterised form. This approach reduces computational costs by orders of magnitudes and allows simulations over multiple glacial-interglacial cycles (Claussen et al., 2002).

This thesis tries to reveal factors and mechanisms that have impacts on noble gases as MOT proxies through the approach of climate modelling. A simple 5-box model was developed for qualitatively understanding noble gas (Kr) dynamics in the global ocean circulation. The Bern3D 2.0 Earth system model of intermediate complexity is used for sensitivity studies and the LGM state simulations. The basic features and simulation set-ups of these two models are introduced in this section.

3.1 The Bern3D Model

3.1.1 General Description

The Bern3D model is a powerful and comprehensive tool in modelling the past climate on a global scale with its reduced complexity and various prognostically formulated tracers. The core physics of the ocean dynamics of the Bern3D model was originally developed by Edwards et al. (1998), and the first complete version of the Bern3D model can be found in the study by Müller et al. (2006).

In 2012, updates were made on the grid sizes for more flexible cell discretisation, with which the cell size can be chosen individually for every latitude and longitude (Ritz, 2013). Meanwhile, the Bern3D model was re-gridded from a horizontal resolution of 36×36 to a new version of 41×40, now referred to as the Bern3D 2.0 model. In z-direction, both versions have the same 32 depth layers logarithmically distributed over 5000 m total depth, with finer resolution at surface ocean and coarser resolution at bottom (Fig 7) (Müller et al., 2006). Other updates on the model regarding processes parameterisation and tuning on parameters are recorded in the PhD thesis by Roth (2013).

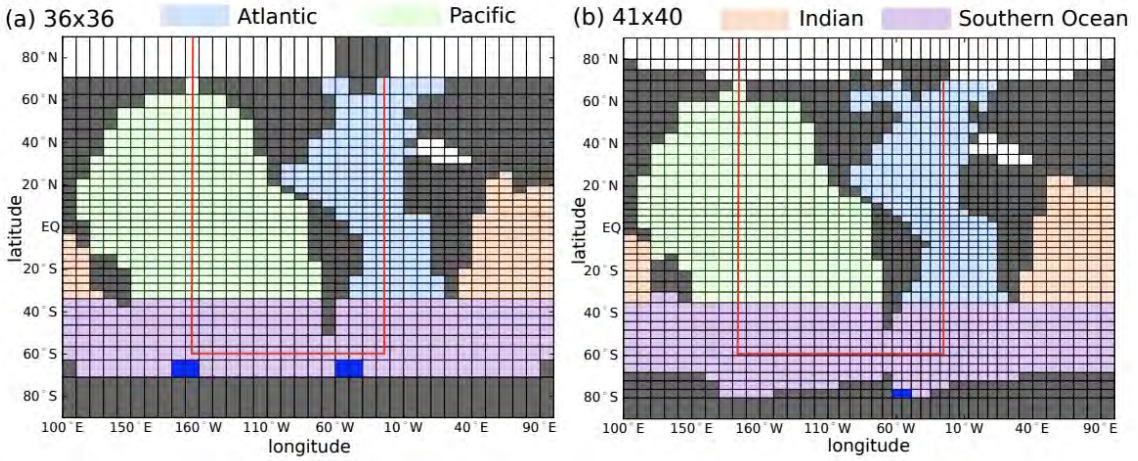

Figure 6: Horizontal maps of the Bern3D model grid (2011) and the Bern3D 2.0 model grid. Blue cells near Antarctic coast represent freshwater removal locations. In the Bern3D 2.0 model, high latitudes are defined with finer grids and therefore represents the land outlines better, particularly enhancing the ocean circulation dynamics around Greenland and the North Atlantic (Roth, 2013).

The Bern3D 2.0 model used in this project has a 3D ocean component and a 2D atmosphere component. Both the atmosphere and the ocean have 41 boxes meridionally and 40 boxes zonally. The ocean component is governed by a seasonally forced geostrophic-frictional model and the atmosphere component governed by the energy and moisture balance (Roth, 2013; Ritz et al., 2010). Detailed equations describing the dynamics of the ocean, atmosphere, sea ice and tracer transport in the Bern3D 2.0 model are documented in Ritz (2013) and published by Ritz et al. (2010).

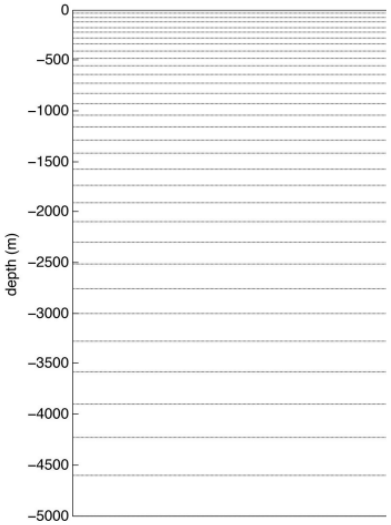

Figure 7: Vertical grid of the Bern3D 2.0 model (Brugger, 2013).

In the Bern3D 2.0 model, one simulation year is divided into 96 time steps. The 2D atmosphere and parameterisation of processes in the Bern3D model allow simulations to be run up to 800 kyr. With only the temperature and salinity tracers enabled, the Bern3D model can simulate roughly 50 kyr per day on a single personal computer CPU

(Ritz et al., 2010). The computational time is proportional to the number of tracers enabled in each simulation.

For this study, eight tracers were particularly of concerns, including temperature, salinity, three noble gases, N_2 and two dye tracers. With these tracers, main features including ocean heat content distribution, noble gas saturation and deep water formation can be analysed to understand the noble gas dynamics and the corresponding ocean state under different boundary conditions.

3.1.2 Noble Gas Implementation

Noble gas tracers were first implemented in the Bern3D model by Ritz et al. (2011). There are two approaches to model noble gas inventories in the climate system: one is to simulate only the ocean component, and the other is to simulate tracers in both, the atmosphere and ocean, and their integrity. For the latter approach, impacts from ocean volume and sea-level pressure change are not considered due to the rigid-lid formulation of the ocean component. The total ocean volume in all Bern3D 2.0 model simulations is 1.3545 $\times 10^{18}$ m^3. Sea level during the LGM was around 120 m lower than present day (Lambeck et al., 2014). For LGM simulations, the influence of this volume difference is accounted for by a virtual flux in the model that adjusts the oceanic inventories accordingly.

With the ocean-only approach, it is assumed that the surface ocean is always approaching full saturation owing to the large atmospheric abundances of the gases (Ritz et al., 2010) For present-day condition, the atmosphere-to-ocean distribution ratio of Kr is roughly 49:1 and 199:1 for N_2 (Weiss and Kyser, 1978). Therefore, the air-sea exchange fluxes of noble gases can be expressed as

$$F_{as} = k(C_s^* - C_s) \tag{4}$$

where k is the gas transfer velocity in m s^{-1}, C_s^* is the saturation concentration of gas in mol m^{-3}, C_s is the concentration at sea-surface in mol m^{-3}. In the Bern3D 2.0 model, k is interpreted with a linear relationship to the surface wind speed (Roth, 2013):

$$k = k_{scale}^{gas} \cdot (1 - F_{ice}) \cdot 7.798 \cdot 10^{-6} \cdot |u|_{NCEP} \cdot \left(\frac{Sc}{660}\right)^{-\frac{1}{2}}, \tag{5}$$

where k_{scale}^{gas}=0.81 is a scaling factor implemented for the radiocarbon tracer to match observational data (Mueller et al., 2008), F_{ice} is the fractional sea ice area of the grid and varies between 0 and 1. Sc is the Schmidt number and u is the wind speed. In the Bern3D 2.0 model, both wind speed and wind stress at sea surface are prescribed according to the monthly climatology from the National Centers for Environmental Prediction (NCEP) and the National Center for Atmospheric Research (NCAR) (Kalnay et al., 1996).

The Schmidt number determines the transfer velocity of gas and is calculated as the water kinematic viscosity over the gas diffusion coefficient (Wanninkhof, 2014). The gas specific Schmidt number has dependency on both temperature and salinity but predominantly on the temperature. Coefficients of the empirical fit of Schmidt number were given by Wanninkhof (2014) with an applicable temperature range between –2 °C to 40 °C:

$$Sc = A_{Sc} + B_{Sc}t + C_{Sc}t^2 + D_{Sc}t^3 + E_{Sc}t^4 \tag{6}$$

where t is seawater temperature in °C.

Table 1: Coefficients of Schmidt number least square fit for different gases in the Bern3D 2.0 model. Applies to seawater of 35‰ salinity (Wanninkhof, 2014).

Gas	A_{Sc}	B_{Sc}	C_{Sc}	D_{Sc}	E_{Sc}
N_2	2304.8	–162.75	6.2557	–0.13129	0.0011255
Ar	2078.1	–146.74	5.6403	–0.11838	0.0010148
Kr	2252.0	–147.33	5.1729	–0.10141	0.00083242
Xe	2975.2	–201.06	7.2057	–0.14287	0.0011798

With justification made by Ritz et al. (2011) on ignoring the bubble injection impact (Stanley et al., 2009), the Kr solubility function in the Bern3D 2.0 model takes the form from Weiss and Kyser (1978), where

$$lnC_s^* = A_1 + A_2\,(100/T) + A_3 ln\,(T/100) + A_4\,(T/100) + S\left[B_1 + B_2\,(T/100) + B_3\,(T/100)^2\right]. \quad (7)$$

N_2 and Ar have the same form of the solubility function in the Bern3D 2.0 model given by Hamme and Emerson (2004):

$$lnC_s^* = A_1 + A_2 T_s + A_3 T_s^2 + A_4 T_s^3 + S(B_1 + B_2 T_s + B_3 T_s^2) \quad (8)$$

with

$$T_s = ln\left(\frac{298.15K - t}{273.15K + t}\right). \quad (9)$$

Xe solubility function was fitted by Ritz et al. (2011) according to the data from Wood and Caputi (1966):

$$lnC_s^* = A_1 + A_2 T_s + A_3 T_s^2 + S(B_1 + B_2 T_s) + ln0.98. \quad (10)$$

For the solubility functions above, t is temperature in degree celsius, T is temperature in Kelvin, values of coefficients involved are listed in Section **??** Table 5.

With the total mass of dry air known to be 5.1×10^{21} g (Schlesinger, 1997; Sarmiento and Gruber, 2006), the present-day atmospheric inventory of each gas can be calculated given the molar weight and atmospheric relative composition (Table 2). For Kr, the reference value of the mixing ratio is calculated to be

$$\left(\frac{I_{atm}^{Kr}}{I_{atm}^{N_2}}\right)_{reference} = 1.46 \cdot 10^{-6}. \quad (11)$$

The present-day oceanic inventory can be calculated from the control simulation under pre-industrial conditions. The sum of these two gives the conserved value of total gas inventory, which can then be used to calculate the corresponding noble gas mixing ratio anomaly given the modelled noble gas concentration in ocean.

3.1.3 Simulation Setup

All simulations performed in this project are steady state simulations. The model was spun up for 35 kyr in total for each run. Spinup 1 is a 10 kyr physical-ocean-only spinup with restoring boundary conditions; spinup 2 includes the energy balance model

Table 2: Atmospheric features of noble gases and N_2. Comparisons between observations (Schlesinger, 1997; Sarmiento and Gruber, 2006) and the Bern3D 2.0 model control simulation.

Gas	Molar weight (g mol^{-1})	Atomspheric relative composition in dry air	Mean Ocean Conc. obs. (μmol m^{-3})	Mean Ocean Conc. Bern3D 2.0 modelled (μmol m^{-3})
Dry air	28.9644	1		
N_2	28.0134	0.78084	575,000	578316
Ar	39.948	$0.934 \cdot 10^{-2}$	16,000	15,698
Kr	83.8	$1.14 \cdot 10^{-6}$	3.8	3.78
Xe	131.3	$8.7 \cdot 10^{-8}$	0.5	0.57

(EBM) with prescribed ice sheets and climate sensitivity and runs for 15 kyr; spinup 3 runs for 10 kyr where all noble gas and biogeochemical tracers are enabled. There are two orbital parameter set-ups for the EBM: pre-industrial (PI) and the Last Glacial Maximum (LGM).

Sensitivity studies of δKr_{atm} were conducted on atmospheric CO_2, diapycnal diffusivity, wind stress and ice leak to examine the response of δKr_{atm} to temperature change in the Bern3D 2.0 model. Simulations were also run with varying Earth climate sensitivities, aerosol forcings and salt fluxes to investigate the ocean temperature and circulation state under different conditions.

Pre-industrial (1765 CE) conditions in the Bern3D 2.0 model are set by radiative forcings represented by greenhouse gas concentrations of CO_2=278.05 ppm, CH_4=721.89 ppb, and N_2O=272.96 ppb. This pre-industrial simulation is referred to in the following as the control simulation and used as the reference when calculating anomalies (ΔMOT, δKr_{atm} etc.) of all other simulations.

Last Glacial Maximum simulations were conducted for MOT comparisons between the Bern3D 2.0 model simulation and ice core measurements. All LGM simulations take physics-only restart from the PI spin-up simulations and were run over 25 kyr to reach steady states. Orbital parameters were set to values at 20 kyr before present (1950 CE) (Berger, 1978), radiative forcings were set to CO_2=191.26 ppm, CH_4=370.46 ppb, and N_2O=208.26 ppb. The ice sheet was not explicitly simulated in the model but the impact of ice sheet extent was accounted in the form of changing surface albedos. The ice sheet extent record was taken from Peltier (2004), with the first 2 kyr of ice sheet linearly scaled from the modern state to the LGM state (Ritz et al., 2010). This linear scaling is important for the freshwater relocation.

Wind Stress exerts direct impacts on the ocean through surface wind-driven circulations. Together with the change it induces in the deep ocean circulation, wind stress affects the ocean heat content distribution and thus the MOT. In the Bern3D 2.0 model, wind stress is a prescribed field from present-day climate records (Kalnay et al., 1996). A global scaling factor (scf=2.0) is applied to this wind stress field after tuning the model to observational fields of modern climate (Ritz et al., 2010). For wind stress sensitivity tests, the wind stress field scaling factor scf was varied between 5% -200% of the control simulation.

Diapycnal Diffusivity describes the mixing perpendicular to the isopycnals. Unlike the wind stress exerting direct impacts on the surface, change in diapycnal diffusivity has influence on vertical shear and convective instabilities inside the ocean (MacKinnon et al., 2013; Alford and Pinkel, 2000). In this thesis, diapycnal diffusivity was chosen to vary between 10^{-6} to 10^{-4} m^2/s and the value in the control simulation is 2×10^{-5} m^2/s.

Atmospheric CO_2 affects the atmospheric temperature by varying the radiative

forcing (RF) as described below:

$$RF(pCO_2) = 5.35\frac{\mathrm{W}}{\mathrm{m}^2} ln(\frac{pCO_2}{pCO_{2,ctrl}}). \tag{12}$$

where $pCO_{2,ctrl}$=278.05 ppm in the control simulation. In atmospheric CO_2 sensitivity tests, values of pCO_2 were chosen so that RF altered from –10 W/m^2 to 5 W/m^2 with 1 W/m^2 steps. This results in a pCO_2 ranging from 42 to 708 ppm. Other factors can also cause change in radiative forcing (pCH_4, pN_2O, ice albedo etc.), here we only conducted pCO_2 sensitivity tests as a representative of radiative forcing sensitivity studies.

Ice Leak is a parameter in the Bern3D model which describes the impact of sea-ice on preventing the air-sea gas exchange. It is a combination of impacts from the gas permeability of sea-ice and the structural fractures in the sea-ice covered regions. In the control simulation, ice leak is set to 0 by default, assuming the air-sea gas exchange is completely prohibited within the sea-ice covered regions. The maximum value of ice leak is 1, when sea-ice has no influence on the air-sea gas exchange. Ice leak parameter is implemented as a term *iceleak* multiplied to the gas transfer velocity k and varies between 0 and 1 in sensitivity tests.

Dye Tracers in the Bern3D model track water that forms at a certain region of surface ocean (Fig. 8). In simulations involved in this study, two dye tracers are restored to 100% at the surface ocean of the prescribed North Atlantic basin and southward of 52°S respectively and 0% elsewhere to track the formation of NADW and AABW.

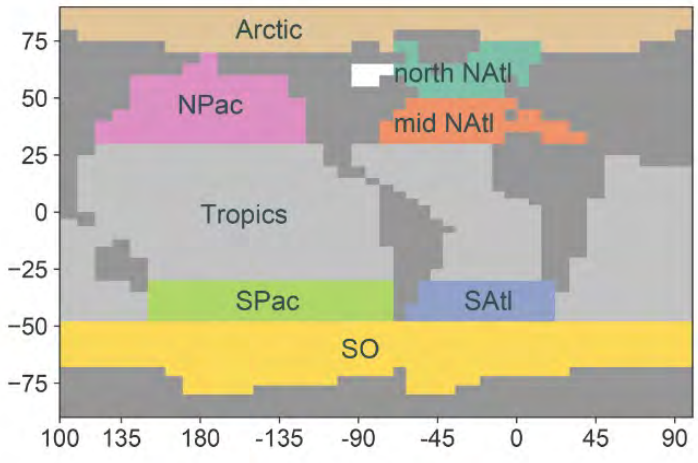

Figure 8: Dye tracer map for the Bern3D 2.0 model. Different colours mark the regions where different dye tracers originate. SO: Southern Ocean, N/SPac: North/South Pacific, N/SAtl: North/South Atlantic (Scheen and Stocker, 2020).

Equilibrium Climate Sensitivity (ECS) is the temperature change after a doubling of atmospheric CO_2 concentration. In the Bern3D 2.0 model control simulation, ECS is 2.98°C. This can be modified by varying a feedback parameter, λ=0.71 W m^{-2} K^{-1} in the control simulation, which acknowledges all physical feedbacks not accounted for (Ritz et al., 2010). A more sensitive climate response can result in a colder LGM. Sensitivity tests were performed on the ECS to investigate the conditions needed for the modelled LGM MOT to approach the ice core reconstructed value.

Aerosol Forcing in the Bern3D 2.0 represents the impacts of mineral dust aerosols on Earth's radiation balance. According to some LGM reconstructions, this forcing is

expected to be around -1W/m^2 (Baggenstos et al., 2019; Hopcroft et al., 2015). However, aerosol forcing is usually ignored in climate modelling (Hopcroft et al., 2015), so it is in the Bern3D default setup. In this thesis, LGM simulations with aerosol forcing of 0 W m^{-2}, –1 W m^{-2}, and –1.5 W m^{-2} are carried out.

Salt Flux in the Bern3D model can be additionally added (removed) to simulate fresh water removal (hosing). An additional 0.5 Sv of salt flux was added to the Southern Ocean in LGM simulation to investigate the possible state of AMOC during the LGM as the past state of AMOC is not yet fully understood.

3.2 The 5-Box Model

Simple box model is a type of model that has uniform properties within each box (temperature, salinity etc.) and their volumes remain constant over time. In this thesis, a conceptual 5-box model was developed to qualitatively understand the dynamics and steady-state abundances of noble gas (Kr) in the climate system.

3.2.1 Model Description

This conceptual model consists of five boxes, out of which two represent low-latitude and high-latitude atmosphere (LA and HA), and the other three represent the surface ocean (SO), the polar ocean (PO) and the deep ocean (DO). The boundary between the high-latitude and LA boxes is set at 60°. The HA box comprises atmospheres at both south and north hemisphere high-latitude regions. The PO box corresponds to the oceans from 0 to 5000 m whose surface have direct exchange to the high-latitude atmosphere box. The SO represents oceans between 0 to 500 m in the low-latitude regions below 60°. The DO box represents the rest ocean in the low-latitude region between 500 to 5000 m.

The box distribution was inspired by the 4-box model described in section 2.3 by Bereiter et al. (2018b). In this 5-box model, the PO box corresponds to the NADW box in the 4-box model, the DO corresponds to the AABW box, and the SO corresponds to the residual ocean. There are mass and heat exchanges between any two ocean boxes, and heat exchanges between atmosphere and ocean boxes in this 5-box model.

This 5-box model is governed by mass conservation and an EBM. The core equation describing physical dynamics came from the Stommel 2-box model, where the water flux q between each two ocean boxes has temperature and salinity dependency described by the Stommel model equation (Stommel, 1961; Titz et al., 2002):

$$q = k[\alpha(T_2 - T_1) + \beta(S_2 - S_1)] \tag{13}$$

where k is the hydraulic constant in m^3 s^{-1}, α is set as -5.4×10^{-5} K^{-1}, β as 7.6×10^{-4} psu^{-1}. T_1 and T_2 are the temperatures of the two adjacent water masses and S_1 and S_2 the salinities.

In order to distinguish between different circulation directions, it is defined that

$$q_{<+>} = \frac{q + |q|}{2} \tag{14}$$

$$q_{<->} = \frac{q - |q|}{2}. \tag{15}$$

The positive sign in $q_{<+>}$ indicates that the flux flows in the same direction as represented by the blue arrows in Fig 9. This is when water flows from low-latitude to high-latitude

region, overturns at the pole and returns in the deep ocean, similar to the AMOC in reality. Whereas $q_{<->}$ indicates an opposite circulation direction.

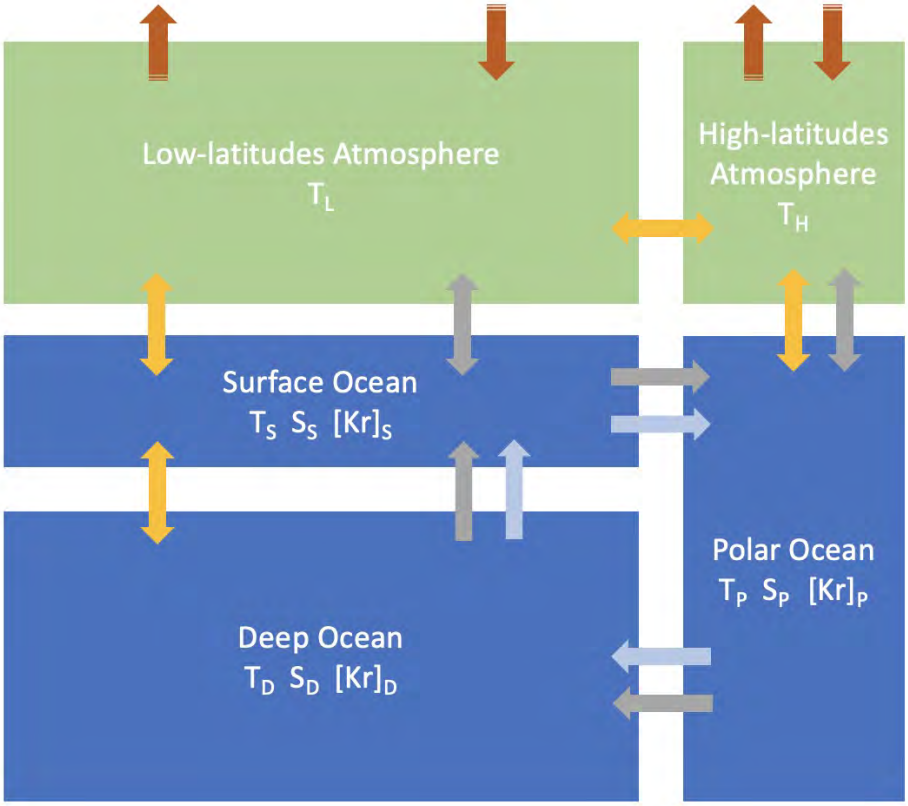

Figure 9: Schematic of the newly formulated 5-box model. Light blue arrows indicate the water exchange between boxes and yellow arrows represent diffusive heat exchange. Red arrows indicate the incoming solar radiation and the outgoing long-wave emission. Grey arrows indicate Kr transport in the Earth system. The deep ocean box does not have any direct mass or heat exchange with the atmosphere.

The conservation equations for heat of the low and high-latitude atmosphere boxes are given by:

$$C_{atm}\rho_{atm}V_L\cdot\frac{dT_L}{dt} = sin\phi[\pi R^2(1-\alpha_L)S_0-4\pi R^2\sigma\epsilon T_L^4]+D_1A_1(T_S-T_L)+kB_1(T_H-T_L) \quad (16)$$

$$C_{atm}\rho_{atm}V_H\cdot\frac{dT_H}{dt} = (1-sin\phi)[\pi R^2(1-\alpha_H)S_0-4\pi R^2\sigma\epsilon T_H^4]+D_2A_2(T_P-T_H)-kB_1(T_H-T_L) \quad (17)$$

Accordingly, the conservation equations for heat in the SO, PO and DO boxes are:

$$C_{ocn}\rho_{ocn}V_S\cdot\frac{dT_S}{dt} = C_{ocn}\rho_{ocn}\left[\left(q_{<+>}T_D+q_{<->}T_S\right)+\left(-q_{<+>}T_S-q_{<->}T_P\right)\right] - D_1A_1(T_S-T_L)+D_3A_1(T_D-T_S) \quad (18)$$

$$C_{ocn}\rho_{ocn}V_P \cdot \frac{dT_P}{dt} = C_{ocn}\rho_{ocn}\left[\left(q_{<+>}T_S + q_{<->}T_P\right) + \left(-q_{<+>}T_P - q_{<->}T_D\right)\right] - D_2A_2(T_P - T_H) \quad (19)$$

$$C_{ocn}\rho_{ocn}V_D \cdot \frac{dT_D}{dt} = C_{ocn}\rho_{ocn}\left[\left(q_{<+>}T_P + q_{<->}T_D\right) + \left(-q_{<+>}T_D - q_{<->}T_S\right)\right] - D_3A_1(T_D - T_S) \quad (20)$$

Salt transport comprises of a convective flux and a diffusive flux. Restoring salinity values were defined for SO and PO boxes respectively (Table 3) to guarantee that salt fluxes lead to a defined equilibrium. The time derivative of the salinity of each ocean box is given as:

$$\rho_{ocn}V_S \cdot \frac{dS_S}{dt} = \rho_{ocn}\left[\left(q_{<+>}S_D + q_{<->}S_S\right) + \left(-q_{<+>}S_S - q_{<->}S_P\right)\right] + \mu_1A_1(S_{Href} - S_S) + \mu_2A_1(S_D - S_S) \quad (21)$$

$$\rho_{ocn}V_P \cdot \frac{dS_P}{dt} = \rho_{ocn}\left[\left(q_{<+>}S_S + q_{<->}S_P\right) + \left(-q_{<+>}S_P - q_{<->}S_D\right)\right] + \mu_1A_2(S_{Lref} - S_P) \quad (22)$$

$$\rho_{ocn}V_D \cdot \frac{dS_D}{dt} = \rho_{ocn}\left[\left(q_{<+>}S_P + q_{<->}S_D\right) + \left(-q_{<+>}S_D - q_{<->}S_S\right)\right] + \mu_2A_1(S_S - S_D) \quad (23)$$

With the fundamental energy and mass conservation equations given, three parameters (k,ϵ and α_L) in the model were tuned so that the temperature of each box meets the reference temperature under present-day conditions (SO: 284 K, PO: 277 K, DO: 276 K). The atmosphere-box reference temperatures are then calculated from the global energy budget. A global mean albedo of 0.3 was set as the mean value of α_L and α_H. In this study, α_L was tuned and α_H was calculated with this constraint on the mean value.

Residuals are calculated as the simulated temperatures over the reference temperatures minus 1. Parameter values with the least residual are the optimal values. With k,ϵ and α_L tuned to present day conditions, all parameters used in the 5-box model are listed in Table 3.

It takes around 3 kyr for all boxes to reach their target tuning temperatures. The 5-box model was run for 3.5 kyr for all tracers to reach equilibrium under pre-industrial setup as the control simulation.

Currently the 5-box applies the explicit Runge-Kutta scheme. For temperature and salinity tracers, the maximum time step is 1 day for simulations to stay stable. However, with Kr tracer implemented, the maximum time step became 1 hour as the surface exchange flux has approximately 20 times faster speed. For a 4 kyr simulation, the current box model takes around 3.5 to 4 hours. A possible improvement would be replacing

the explicit scheme with an implicit scheme, which will allow for a bigger time step and largely shorten the simulation time.

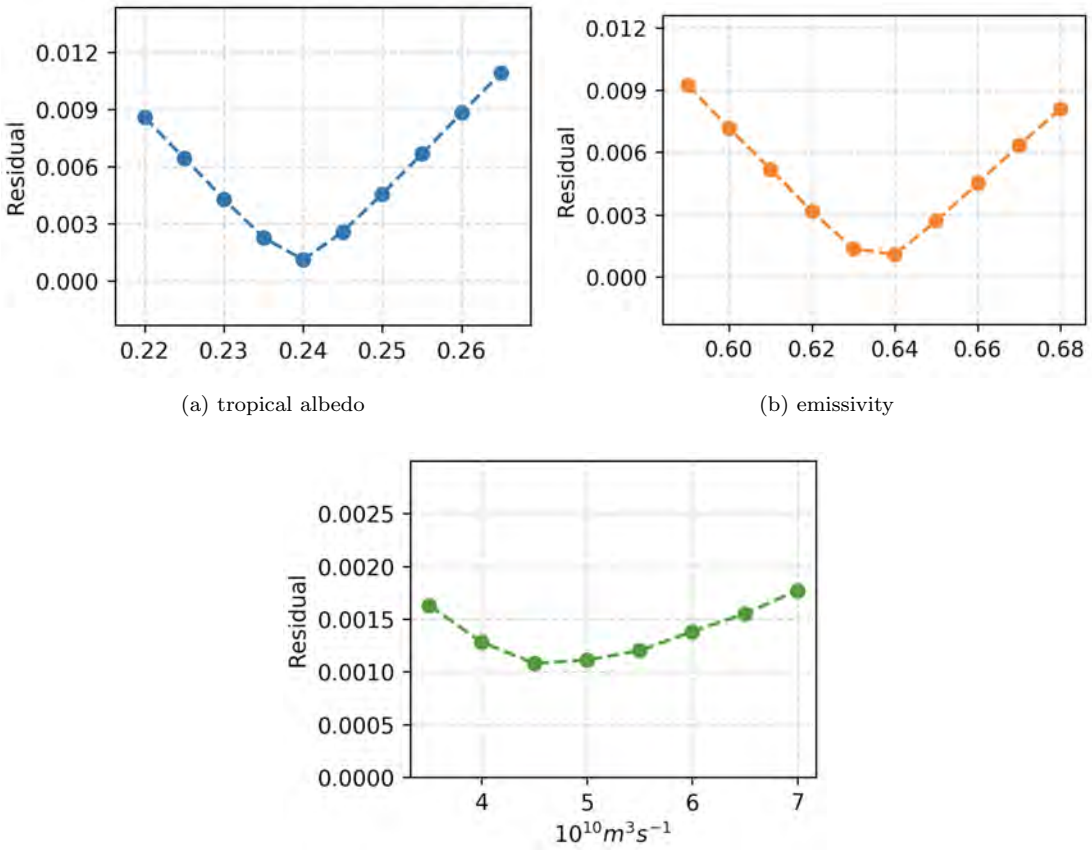

(a) tropical albedo

(b) emissivity

(c) hydraulic constant

Figure 10: Tuning of three parameters in the 5-box model. Parameter value with the smallest residual value is the optimal tunned value.

3.2.2 Kr Implementation

Kr tracer is implemented in the 5-box model with a similar approach as in the Bern3D 2.0 model. The air-sea gas exchange flux is calculated using Eq. 4, based on the assumption that the atmosphere is an infinite reservoir for Kr. Instead of the linear fit for the gas transfer velocity with a scaling factor to tune the radiocarbon tracers in the Bern3D 2.0 model, here in the 5-box model, k_{gas} is given as:

$$k_{gas} = 0.251 < U^2 > (Sc/660)^{-0.5}. \tag{24}$$

This quadratic relation holds for wind speed between 3-15 m s^{-1}. Note that the wind speed U has the unit of m s^{-1} and k_{gas} is in cm h^{-1} (Wanninkhof, 2014). For simplification, a global mean wind of 7.3 m s^{-1} from the Cross Calibrated Multi-Platform (CCMP) is substituted into the equation. The Schmidt number calculation is the same as in Eq. 6. For the solubility equation, a more recent study was used (Jenkins et al., 2019):

$$lnC^* = A_1 + A_2\,(100/T) + A_3 ln\,(T/100) + A_4\,(T/100) + S\left[B_1 + B_2\,(T/100) + B_3\,(T/100)^2\right] + C_1 S^2. \tag{25}$$

The values of coefficients and a detailed justification of using this equation are mentioned later in Section 5.2.1.

Apart from the air-sea gas exchange at the air-sea interface of the surface and polar ocean boxes, there are also Kr fluxes between each two ocean boxes due to the mixing process. The mass conservation for Kr in the surface, polar and deep ocean boxes are given as:

$$V_S \cdot \frac{d[Kr]_S}{dt} = A_1 k_{gas}([Kr]^*_S - [Kr]_S) + \left[\left(-q_{<+>}[Kr]_S - q_{<->}[Kr]_P\right) + \left(q_{<+>}[Kr]_D + q_{<->}[Kr]_S\right)\right] \quad (26)$$

$$V_P \cdot \frac{d[Kr]_P}{dt} = \left((1 - F_{ice}) + (F_{ice} \cdot iceleak)\right) A_2 k_{gas}([Kr]^*_P - [Kr]_P) + \left[\left(q_{<+>}[Kr]_S + q_{<->}[Kr]_P\right) + \left(-q_{<+>}[Kr]_P - q_{<->}[Kr]_D\right)\right] \quad (27)$$

$$V_D \cdot \frac{d[Kr]_D}{dt} = \left[\left(q_{<+>}[Kr]_P + q_{<->}[Kr]_D\right) + \left(-q_{<+>}[Kr]_D - q_{<->}[Kr]_S\right)\right]. \quad (28)$$

The PO box has two parameters describing the impact of sea ice on air-sea gas exchange. F_{ice} is the percentage of surface PO box being covered by sea ice and *iceleak* is the ice leak parameter, same as in the Bern3D 2.0 model (Eq. 5). F_{ice}=1 represents a PO box fully covered by sea ice.

Table 3: Parameters in the tuned 5-box model.

Parameter	Value	Description
h_{atm}	8000 m	atmospheric scale height
h_{ocn}	5000 m	ocean depth
h_1	500 m	surface ocean depth
ρ_{atm}	1.225 kg m^{-3}	atmospheric density
ρ_{ocn}	1028 kg m^{-3}	sea water density
C_{atm}	1028 J kg^{-1} K^{-1}	atmosphere specific heat capacity
C_{ocn}	3900 J kg^{-1} K^{-1}	sea water specific heat capacit
S_0	1360 W m^{-2}	solar constant
ϵ	0.64	grey body emissivity (tuned)
α_L	0.24	albedo at low latitudes (tuned)
α_H	0.69	albedo at high latitudes
k	4.5×10^{10} m^3 s^{-1}	hydraulic constant (tuned)
A_1	2.58×10^{14} m^2	horizontal contact area between SO and LA
A_2	3.99×10^{13} m^2	horizontal contact area between PO and HA
B_1	1.6×10^{11} m^2	meridional contact area between LA and HA
D	400 W m^{-2}	atmospheric heat transfer rate
D_1	5 W m^{-2}	air-sea heat transfer rate at low lattitudes
D_2	10 W m^{-2}	air-sea heat transfer rate at high lattitudes
D_3	0.2 W m^{-2}	heat transfer rate between DO and SO
μ_1	6×10^{-5} kg m^{-2} s^{-1}	salt restoring rate
μ_2	3×10^{-5} kg m^{-2} s^{-1}	salt transfer rate between DO and SO
S_{Lref}	36 psu	restorting salinity at low-latitude SO
S_{Href}	33 psu	restorting salinity at high-latitude PO

4 Results and Analysis

4.1 Impacts of the Sea Ice

A series of sensitivity tests were performed where wind stress, diapycnal diffusivity and atmospheric CO_2 concentration were varied. The resulting MOT anomalies are between –3 and +3.5°C relative to the control simulation. Varying atmospheric CO_2 concentration generates the largest change in the MOT anomalies, as it affects the global radiation balance (Fig. 11c). Changing the physical ocean circulation alone and not the global radiation balance leads to an MOT cooling by only less than 1°C (Fig. 11a and Fig. 11b).

Changes in these three parameters exert different impacts on the ocean circulations respectively and hence affect the MOTs differently as described in Section 3.1.3. Even though the boundary conditions differ substantially, $\delta \mathrm{Kr}_{atm}$ to MOT relation in different sensitivity tests remains the same (Fig. 11d).

There are two exceptional regimes: one occurs in simulations with wind stress less than 70% of the control simulation, the other occurs in atmospheric CO_2 sensitivity tests when ΔMOT is lower than –3°C. Exceptional simulations in the atmospheric CO_2 sensitivity tests are discussed later in this section and the different $\delta \mathrm{Kr}_{atm}/\Delta$MOT pattern appeared in the low-wind-stress simulations is further discussed in section 4.2.

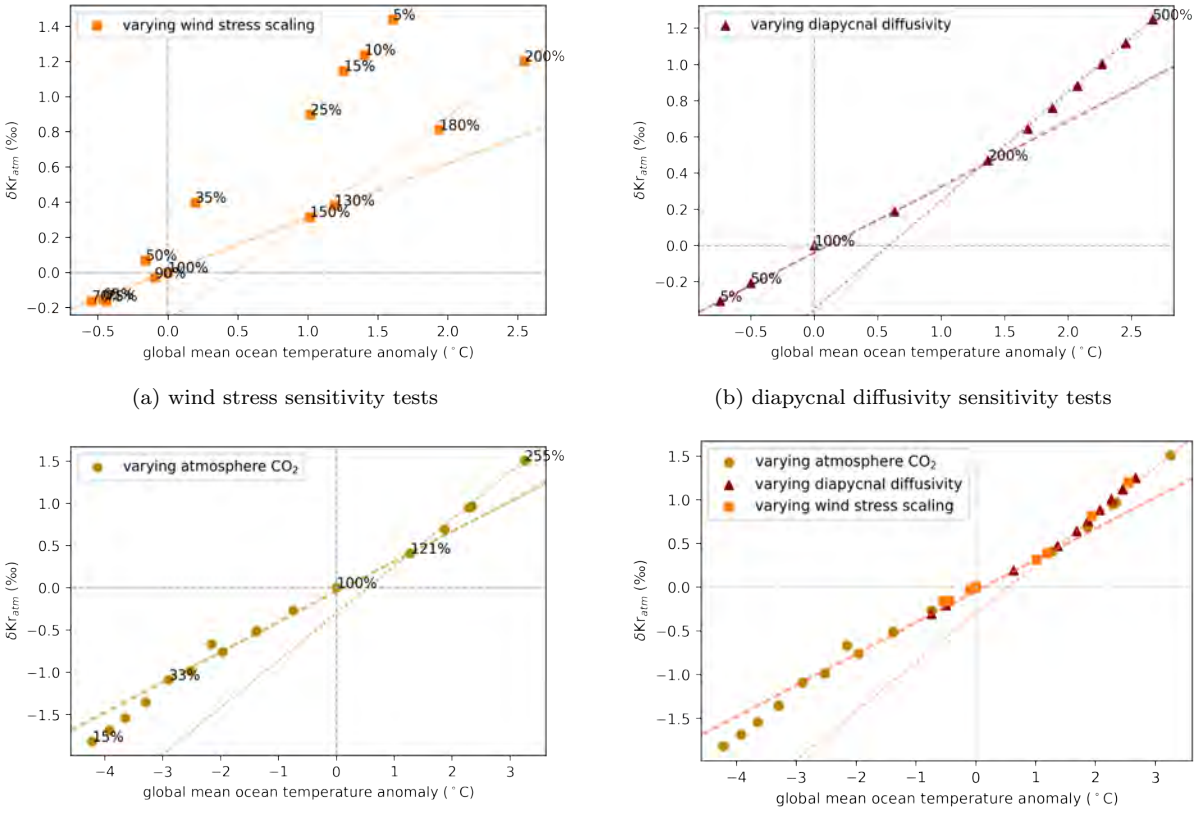

(a) wind stress sensitivity tests

(b) diapycnal diffusivity sensitivity tests

(c) atmospheric CO_2 sensitivity tests

(d) all simulations apart from low wind stress regime

Figure 11: Sensitivity tests in the Bern3D 2.0 model. Dotted lines and dashed lines are drawn for a rough illustration of change in the $\delta \mathrm{Kr}_{atm}/\Delta$MOT ratio. The cross point of grey dashed lines marks the control simulation. Diapycnal diffusivity and atmospheric CO_2 concentrations are positively correlated with the MOTs and hence the parameter values relative to the control simulation are not specifically labeled in the plots.

Within a reasonable temperature range for MOT (below 10°C), it is expected that $\delta Kr_{atm}/\Delta MOT$ in all simulations should fall on one close-to-linear relation based on the temperature-dependent solubility of Kr and non-temperature dependence in N_2 solubility (Fig. 2). However, a noticeable change in the gradients of $\delta Kr_{atm}/\Delta MOT$ occurred when MOT is between 1 and 1.5°C in all three sensitivity tests (Fig. 11).

The assumption that $\delta Kr_{atm}/\Delta MOT$ should follow the same form as the solubility to temperature is based on the prerequisite that the surface gas concentrations are equal to the saturated concentrations. Therefore, processes that lead to undersaturation or supersaturation of Kr can contribute to deviation of $\delta Kr_{atm}/\Delta MOT$ from the theoretically expected relation. δKr_{atm} decouples from ΔMOT signal in this situation. This can be caused by a layer of freshwater or ice at ocean surface blocking the air-sea gas exchange.

While the impact from large area of surface fresh water on Kr saturation is not particularly investigated here, change of sea-ice extensions in these simulations are plotted for the Arctic and the Southern Ocean separately (Fig. 12).

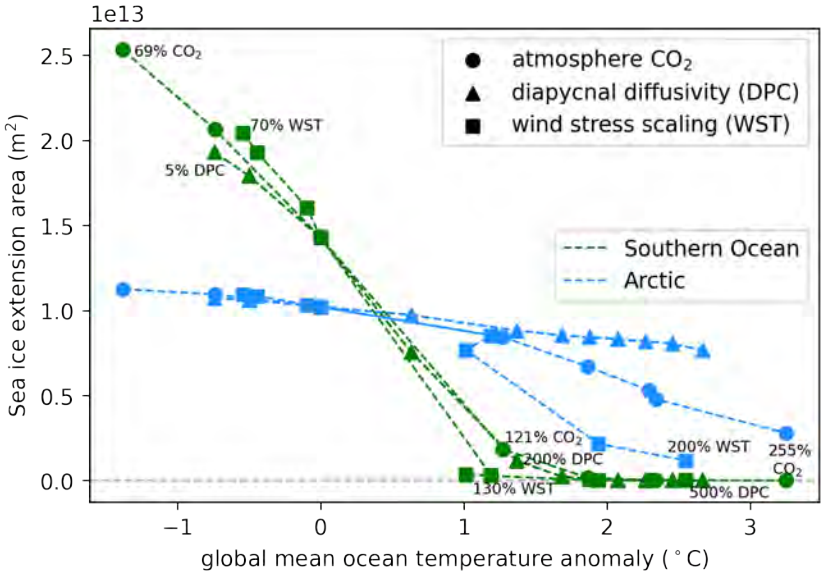

Figure 12: Change of sea-ice extent in Arctic and the Southern Ocean to different forcings in the Bern3D 2.0 model sensitivity tests. Percentages of different parameters to the control simulation are marked on the plot for simulations with the highest and lowest ice area in each sensitivity test and also the turning point around 1.3°C.

As the MOT increases with changing boundary conditions, overall sea-ice area keeps decreasing in all simulations. The sea-ice extent in Arctic decreases rather smoothly with increasing temperature, and some sea ice remains even with an MOT of 3°C warmer than the control simulation. Meanwhile, ice area over the Southern Ocean drops faster as MOT rises than in Arctic and almost vanishes between 1 and 1.5°C in all simulations, same as when the gradient change occurred in Fig. 11.

The impact of sea ice can be observed in the Bern3D 2.0 model control simulation, where the surface ocean Kr undersaturation (in blue) is highly overlapping with the sea-ice covered region, both around the Southern Ocean and the Arctic (Fig 13). As the ice leak parameter is set to be 1 in all simulations involved in Fig. 11d and completely prohibits any air-sea gas exchange, this generates undersaturation of Kr in the ocean.

Meanwhile, surface ocean is slightly supersaturated with Kr in the warm tropics and around the coasts (Fig 13), where upwelling takes place (Cury et al., 2000). In these

regions, cold deep water upwells to the surface and Kr solubility decreases as the water gets warmed up by surface radiation.

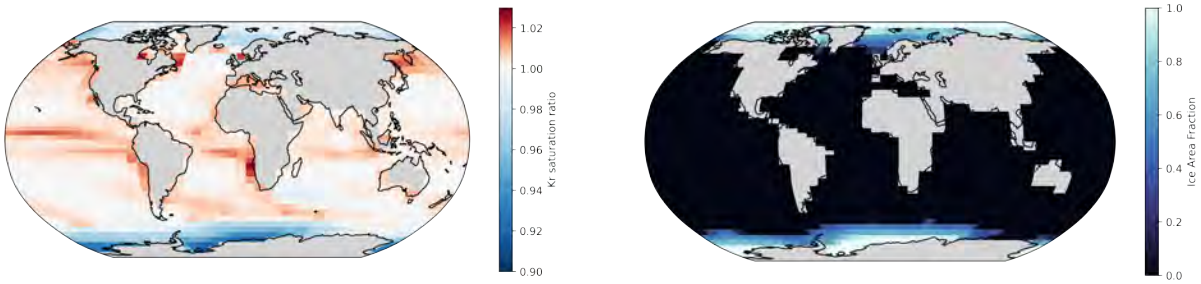

(a) Surface Kr saturation ratio

(b) Ice area fraction

Figure 13: Global distribution of Kr surface saturation ratio and ice area fraction global map in the Bern3D 2.0 model control simulation. Land is masked in grey.

Sea ice leading to decoupling of $\delta \mathrm{Kr}_{atm}$ and ΔMOT signals can be observed directly in the 5-box model results with its highly simplified ocean interior setup. As described in section 2.2, Kr dissolves at the surface and gets transported into ocean interior. This is reflected in the 5-box model control simulation result (Fig 14a), where the PO box is ice-free. The PO and DO boxes have the same Kr concentrations because Kr in the DO box is downwelled directly from the PO box.

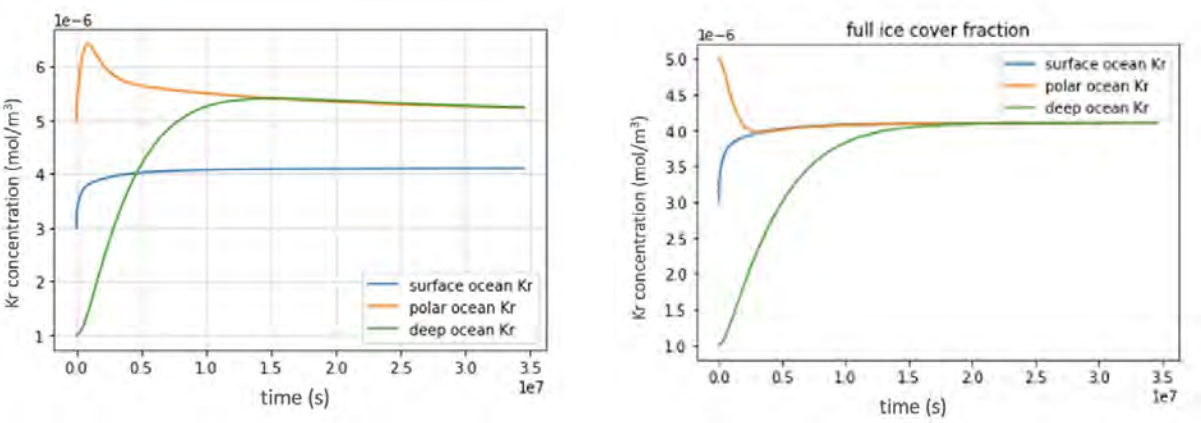

(a) Kr concentrations in control simulation

(b) Kr concentrations in ice-covered simulation

Figure 14: Kr concentrations from the 5-box model control simulation (left) and simulation with fully ice-covered PO box. Kr concentrations here are at the same order of magnitude as the Bern3D 2.0 model mean Kr concentration (10^{-6} mol m^{-3}).

When the PO box is set to be fully covered by sea ice, all three ocean boxes reach the equilibrium with the same Kr concentration as that of the SO box in the control simulation (Fig. 14b). In this setup, heat transport is the same as in the control simulation and only the gas exchange is affected by sea ice. Kr in the ocean only dissolves at the SO box and carries only the temperature signal of the SO. At the PO box, there is free exchange of heat fluxes between the atmosphere and ocean, but no Kr flux. The resulting temperatures of each box is still the same as in the control simulation, but the oceanic Kr inventory is different. This indicates that blocking air-sea gas exchange at the surface can decouple the temperature and Kr signals.

In reality, sea ice obstructs the air-sea gas exchange to some extent but does not completely block it. In Fig. 15a and Fig. 15b, $\delta \mathrm{Kr}_{atm}$ sensitivity to the ice leak parameter is investigated using both the Bern3D 2.0 model and the 5-box model. Simulations were performed with *iceleak* varying from 0 to 1 and other setup remains as in the control simulation. In both models, $\delta \mathrm{Kr}_{atm}$ responds non-linearly to change in ice leak. $\delta \mathrm{Kr}_{atm}$ is highly sensitive to small change in the ice leak when *iceleak* is close to 0.

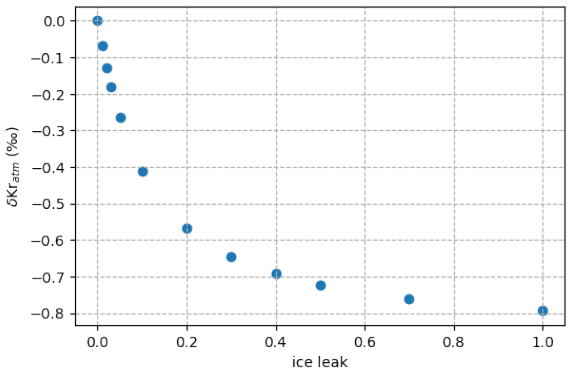

(a) ice leak sensitivity tests in the Bern3D 2.0 model

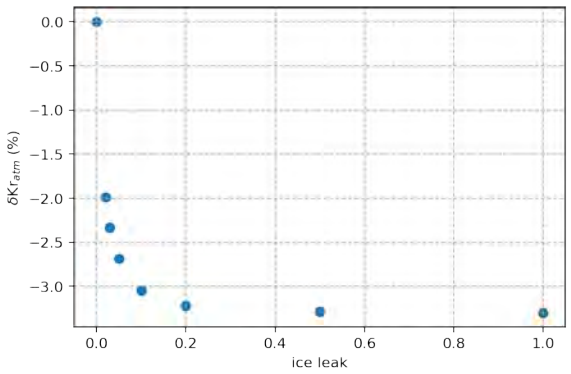

(b) ice leak sensitivity tests in the 5-Box model

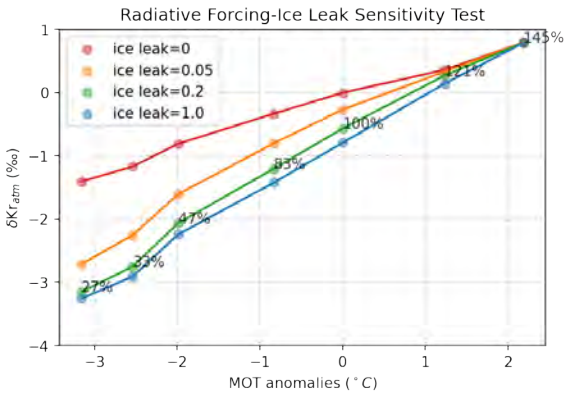

(c) ice leak - atm. CO_2 sensitivity in the Bern3D 2.0 model

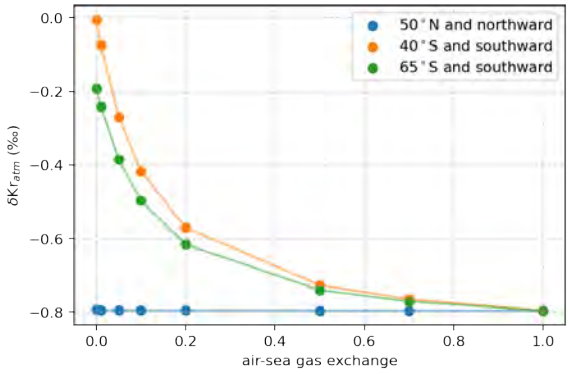

(d) ice leak influence at different regions in the Bern3D 2.0 model

Figure 15: Ice leak sensitivity tests in the Bern3D 2.0 model and the 5-box model. (0,0) refers to the control simulation. In the Bern3D 2.0 model, atmospheric CO_2 is being varied to generate different boundary conditions. The red dots in (c) are from the same simulations in Fig. 11c. The red line connecting the red dots represents the $\delta \mathrm{Kr}_{atm}/\Delta$MOT relation in Fig. 11d. Percentages marked in (c) shows the corresponding atmospheric CO_2 to the control simulation. In the 5-box model (b), $\delta \mathrm{Kr}_{atm}$ is calculated under the assumption that oceanic N_2 concentration is 0.582 mol m^{-3} independent of temperature change.

In the Bern3D 2.0 model control simulation, sea ice fully blocks air-sea gas exchange at ice covered regions. When *iceleak* varies from 0.2 to 1, the change in $\delta \mathrm{Kr}_{atm}$ is approximately 0.22‰ (Fig. 15a), which is close to the current 0.2‰ measurement error of the $\delta \mathrm{Kr}_{atm}$ measured in ice core samples (Haeberli et al., 2020).

The decrease in $\delta \mathrm{Kr}_{atm}$ when allowing 20% of air-sea gas exchange through ice leak is more than 70% of the decrease caused by allowing completely free air-sea gas exchange under pre-industrial conditions and around 90% during LGM when MOT is 2-3°C colder (Fig. 15c).

The ice leak sensitivity test result in the 5-box model is not quantitatively comparable to that in the Bern3D 2.0 model due to the difference in total ocean volume, ocean interior

setup and simplification on physical processes. However, δKr_{atm} in the 5-box model also shows a similar pattern to change in the ice leak as in the Bern3D 2.0 model (Fig. 15b). This further confirms the non-linear influence of sea ice on δKr_{atm}. With a 0.2 ice leak, change in δKr_{atm} is over 90% of the change induced by allowing free air-sea gas exchange.

Within the ΔMOT range of –3 to 0°C and assuming 10% to 20% air-sea gas exchange allowed in ice covered regions, the error caused by omitting the sea ice is between 0.1‰ and 0.4‰. This justifies the omission of the sea ice existence in the 4-box model when interpreting measured δKr_{atm} to corresponding ΔMOT, since the error is smaller to assume free air-sea gas exchange when the state of sea ice is not fully understood in a past period.

However, it cannot be excluded that there are regions covered by continuous sea ice with more than 80% of air-sea gas exchange blocked especially during glacial periods. The ice leak value describes the overall result of gas permeability of sea ice and percentages of fractures in a sea-ice covered region. Further studies on sea ice and other boundary conditions in the past are required to determine an empirical ice leak value that can more precisely parameterise this impact.

In Fig. 15d, the impact of sea-ice blocking air-sea gas exchange on δKr_{atm} is examined in different regions separately. Different from the 5-box model where all high-latitude oceans are represented by one uniform box, in the Bern3D 2.0 model, *iceleak* can be prescribed for different regions individually. Since sea ice in the Bern3D model has influences on the ocean circulation, ice leak in simulations involved in Fig. 15d is prescribed as scalar field independent of the sea ice area. The ice-leak field does not influence the physical circulation but only the air-sea gas exchange. Other boundary conditions remain the same as in the control simulation. The value of *iceleak* is varied from 0 to 1 in three prescribed regions respectively: northward of 50°N (representing the NADW formation region, including the Arctic and part of the North Atlantic), southward of 40°S (representing the Southern Ocean) and southward of 65°S (representing the main AABW formation region). Other regions have free air-sea gas exchange in the simulations. Change in sea-ice leak over the NADW formation region has negligible impact on δKr_{atm} comparing to the Southern Ocean (Fig. 15d). By setting the *iceleak* over the Southern Ocean as 0, the resulting δKr_{atm} is nearly the same as in the control simulation. By fixing *iceleak* over the main AABW formation region (65°S and southward) as 0, δKr_{atm} decreases by around 0.2‰. This difference is generated by Kr being allowed to dissolve at the ice-free surface ocean between 40°S and 65°S.

Large volume of undersaturated water exists in the deep ocean when sea ice exists in the Southern Ocean in the control simulation (Fig. 16c). Ocean is close to saturation of Kr everywhere when no sea ice exists in the Southern Ocean under strong wind stress (Fig. 16d). Sea ice in the AABW formation region has predominant impacts on δKr_{atm} compared to that in the NADW formation region due to the following reasons.

First and most importantly, AABW takes up the major volume of the deep ocean and hence plays a more important role in the MOT change. The volume comparison between NADW and AABW can be roughly seen in Fig. 16. Sea ice over the AABW formation region generates large volume of undersaturation in AABW (Fig. 16c) and decouples noble gases from deep ocean temperature signal, and hence decouples from the MOT signal.

Besides the volume difference, NADW and AABW differ in the mechanisms of their formation. AABW formation is more associated with brine rejection and therefore existence of sea ice has large influence on the Kr saturation ratio. Whereas NADW is mostly

formed by convection. Water bodies can still be exposed to the atmospheric Kr reservoir at lower latitudes before sinking down in the north. In the Bern3D 2.0 model, the location where water mass sinks and forms NADW is further down south comparing to observations. For some grids at the boundary of NADW formation region in the model, sea ice does not persist throughout the year but varies seasonally, allowing Kr to dissolve during warm seasons. This makes the Kr saturation ratio of NADW even less affected by sea ice in the model.

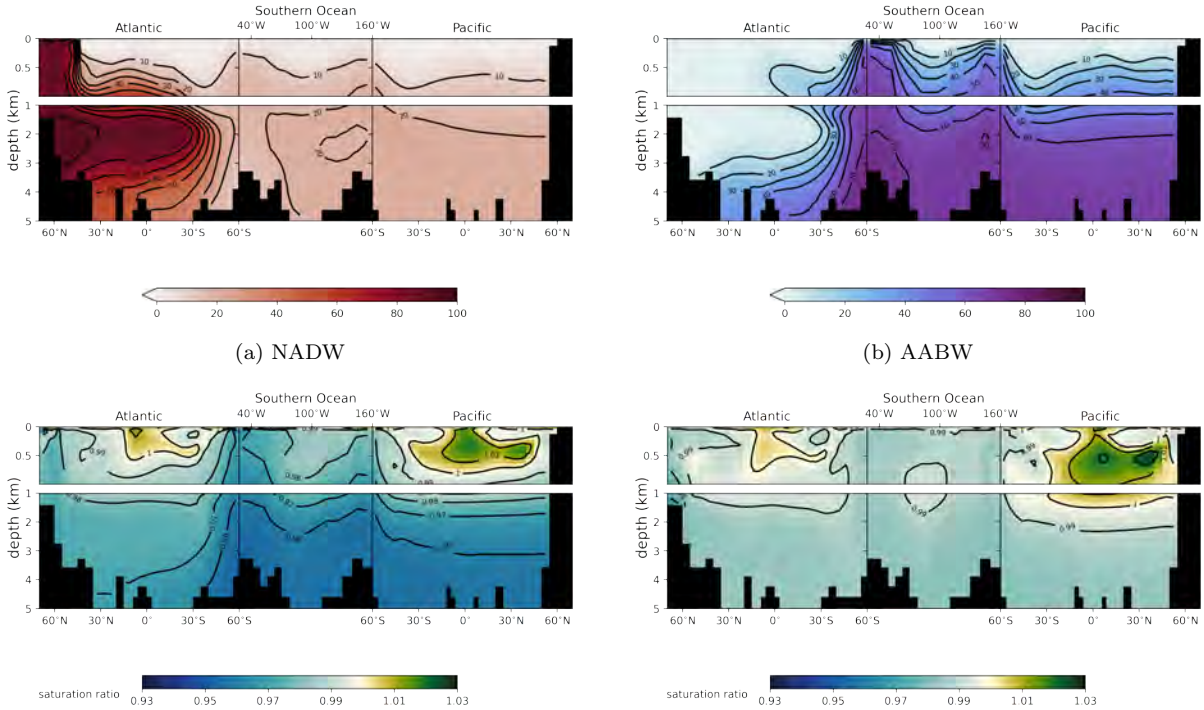

(a) NADW

(b) AABW

(c) Kr saturation ratio in the control simulation

(d) Kr saturation ratio at ΔMOT=+2°C

Figure 16: Deep water formation in the Bern3D 2.0 model control simulation (a, b) and Kr saturation ratio with (c) and without (d) sea ice over the Southern Ocean.

The most undersaturated water masses in Fig. 16c highly overlaps the AABW volume in Fig. 16b. This confirms our statement that a significant undersaturation of Kr propagates down from the surface Southern Ocean to the deep ocean via AABW formation. Therefore, the existence of sea ice over the Southern Ocean has crucial influence on the Kr saturation ratio of AABW formed in this region, and hence is crucial to the global Kr saturation state.

The global mean value of Kr saturation ratio are calculated to show how the overall Kr saturation state varies as sea ice expands (Fig. 17). When the global sum of sea-ice area is smaller than 1×10^{13} m^2, global mean Kr saturation ratio is around 99%, very close to the fully saturated ideal situation. As sea ice starts to form over the Southern Ocean and extends, global mean Kr saturation ratio decreases proportionally. This negative correlation between global sea ice area and mean Kr saturation ratio dilutes once AABW formation region is fully covered by sea ice. Further extension of sea ice in other regions has much weaker influence on Kr saturation ratio. Simulations with sea ice area larger than 5×10^{13} m^2 in Fig. 17a corresponds to simulations in Fig. 11c with ΔMOT<3°C. These exceptional points represent the $\delta\mathrm{Kr}_{atm}/\Delta$MOT gradient under the situation when global mean Kr saturation ratio no longer decreases rapidly and proportionally as sea ice expands after the Southern Ocean is fully ice-covered, but rather stabilises around 94%.

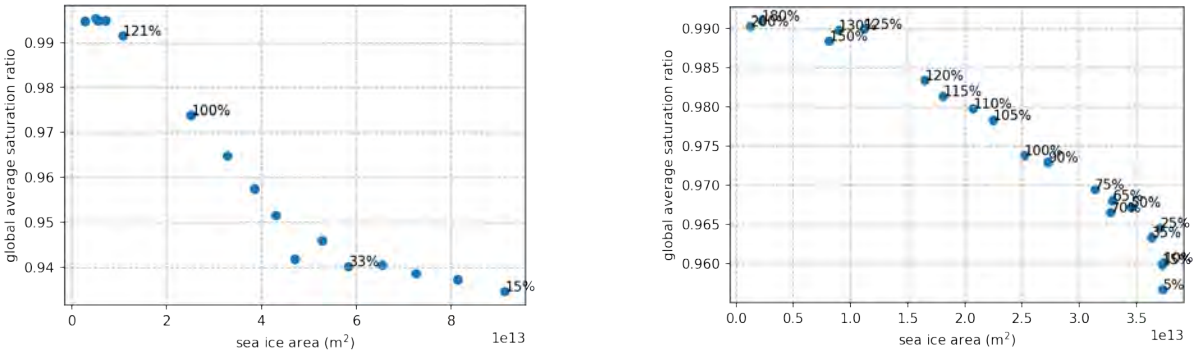

(a) Atmospheric CO_2 simulations

(b) wind stress simulations

Figure 17: Global mean Kr saturation ratio versus the global sum of sea-ice area in atmospheric CO_2 concentration and wind stress sensitivity tests. Percentages in the plot represent the values of varying parameters to the control simulation value.

The same negative correlation between Southern Ocean sea ice expansion and global mean Kr saturation ratio is also seen in the wind stress sensitivity tests (sea ice area between 1-3.5×10^{13} m^2 in Fig. 17b). However, sea ice ceases to expand with decreasing wind stress when ice area exceeds 3.5×10^{13} m^2, but global mean Kr saturation ratio still keeps decreasing. In atmospheric CO_2 sensitivity tests, sea-ice expansion experiences twice larger change than in the wind stress simulations, but the global average Kr saturation ratio to sea-ice area relation does show the same abrupt change that occurred around 50% wind stress. δKr_{atm} did not decouple from MOT signal in Fig 11c with larger sea-ice area when decoupling happened in wind stress simulations. This indicates that another factor besides the sea ice extension has influenced the $\delta Kr_{atm}/\Delta MOT$ relation in wind stress simulations.

4.2 Impacts of the AMOC

The existence of the Southern Ocean sea ice contributes to the $\delta Kr_{atm}/\Delta MOT$ gradient change at $\Delta MOT \approx 1.3°C$ (Fig 18). However, this cannot solely explain the additional decoupling of δKr_{atm} from ΔMOT occurring in simulations with wind stress lower than 70%. By comparing simulations in the low-wind-stress regime to all other simulations in the sensitivity tests, it is seen that $\delta Kr_{atm}/\Delta MOT$ forms a third gradient (the blue dash-dotted line) different from relations represented by the dotted pink line (without sea ice over the Southern Ocean) and dashed pink pink line (with sea ice over the Southern Ocean).

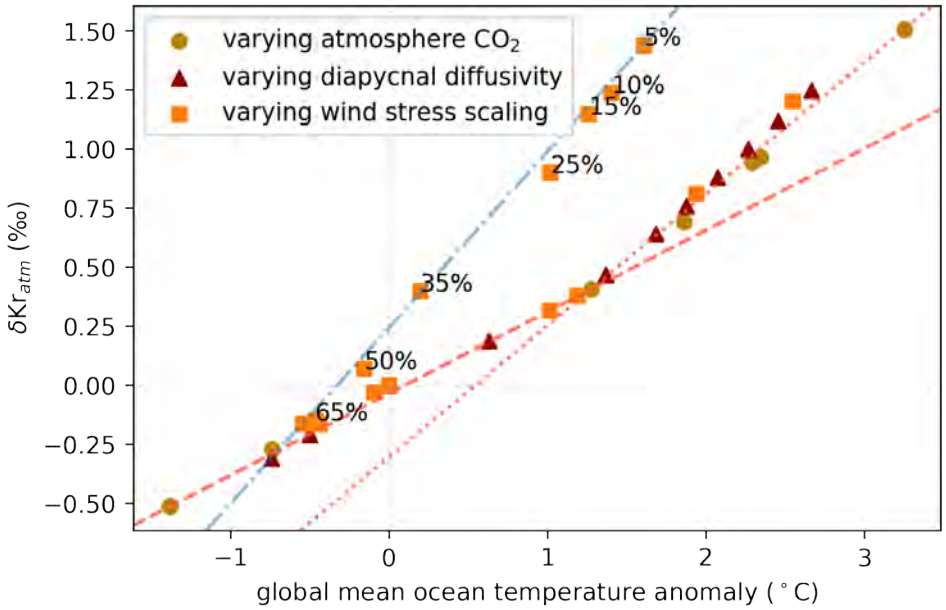

Figure 18: Bern3D 2.0 model sensitivity tests with low-wind-stress simulations. The drawn lines are for rough indications of $\delta Kr_{atm}/\Delta MOT$ relations in different regimes.

Although sea-ice-induced undersaturation generates deviation in the $\delta Kr_{atm}/\Delta MOT$ relation in simulations with $\Delta MOT < 1.3°C$, for all simulations on the pink dotted and dashed lines, a given δKr_{atm} value only corresponds to one ΔMOT value, and a higher δKr_{atm} value indicates a warmer MOT. However, when the low-wind-stress simulations (blue dotted-dashed line) are also taken into consideration, ocean states with same MOT may correspond to different δKr_{atm} values under different boundary conditions. For instance, simulations with 25% and 150% wind stress both have an $\Delta MOT \approx +1°C$, but their δKr_{atm} values have a difference of approximately 0.65‰. A higher δKr_{atm} value does not necessarily indicate a warmer ocean anymore.

In the low-wind-stress simulations, δKr_{atm} is further decoupled from MOT signals comparing to the sea-ice-induced undersaturated scenario. It is important to understand the mechanism leading to this decoupling as it indicates a regime in which δKr_{atm} can no longer be used as a reliable MOT proxy.

A major difference between the atmospheric CO_2 and wind stress simulations is that ocean circulations experience larger changes in latter simulations as the circulation is directly affected by the wind stress. In order to further inspect the change in the ocean circulations, the AMOC under different wind stress and atmospheric CO_2 conditions are illustrated (Fig 19).

The change in the AMOC when atmospheric CO_2 varies from 127 ppm (46% of the control simulation) to 708 ppm (255% of the control simulation) is smaller than the difference between the AMOCs in 50% and 130% wind stress simulations (Fig. 19). When atmospheric CO_2 concentration is 127 ppm, although very weak, the AMOC (indicated in red) is still present in the ocean below 1 km. At 50% wind stress, however, the deep ocean branch of the AMOC vanished, leaving only the wind-driven Ekman transport at surface ocean (Fig. 19a).

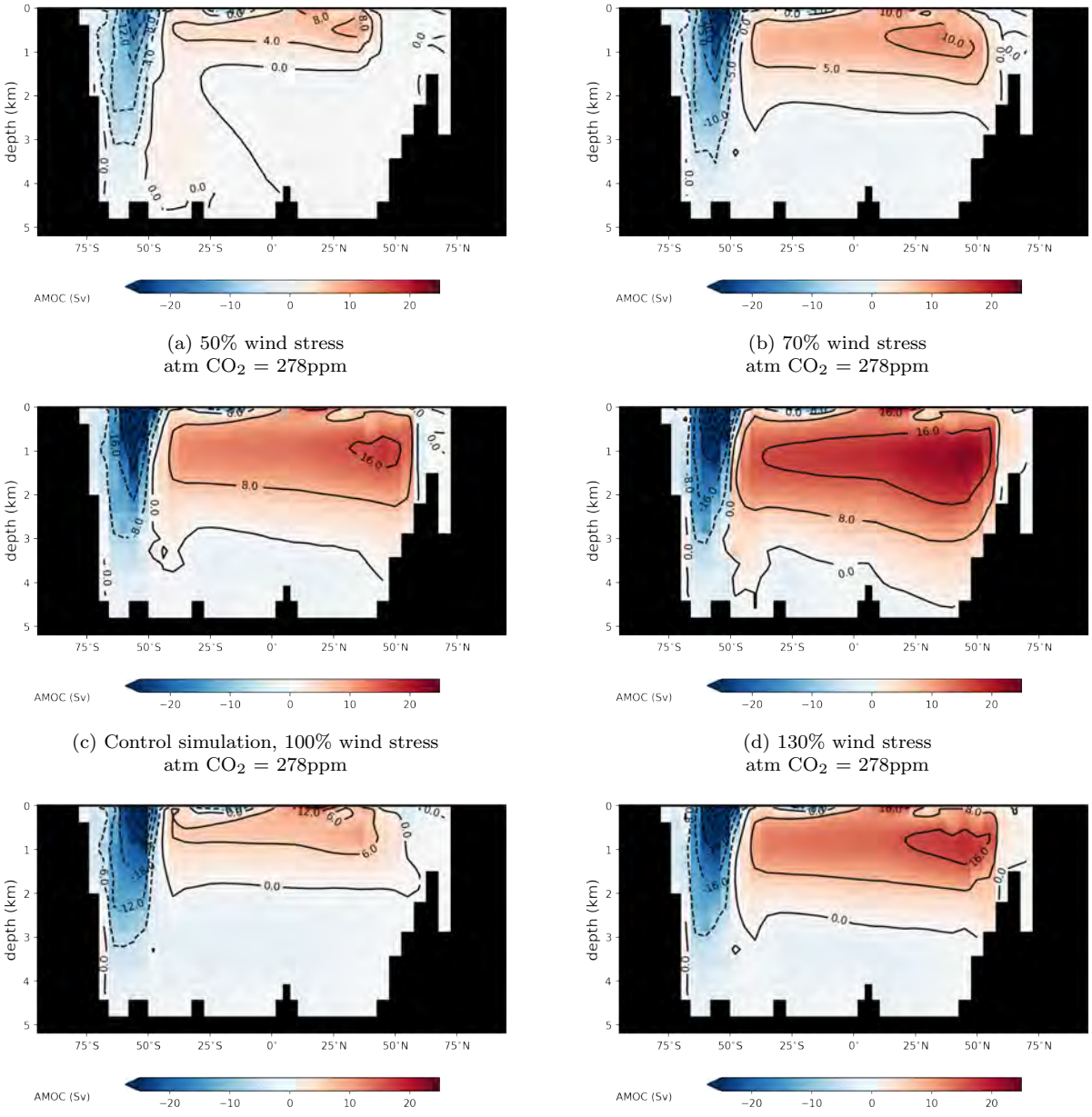

(a) 50% wind stress
atm CO_2 = 278ppm

(b) 70% wind stress
atm CO_2 = 278ppm

(c) Control simulation, 100% wind stress
atm CO_2 = 278ppm

(d) 130% wind stress
atm CO_2 = 278ppm

(e) 100% wind stress
atm CO_2 = 127 ppm

(f) 100% wind stress
atm CO_2 = 708 ppm

Figure 19: AMOC under different wind stress and atmospheric CO_2 conditions. Colours indicate the different directions of meridional transport stream function: red for clockwise and blue for anticlockwise.

To exclude surface wind-driven gyres, location of the maximum AMOC in the control simulation (45°N, 1158 m) is selected for illustrating the change of AMOC strengths in deep ocean under different wind stresses. When the wind stress is larger than 70%,

strengths of AMOC at this location smoothly decreases as the wind stress drops. As the wind stress drops from 70% to 50%, AMOC at the chosen location experiences a complete shutdown (Fig. 20a).

MOT increases when wind stress changes from 65% to 5% and from 70% to 200%, both leading to an increase in $\delta\mathrm{Kr}_{atm}$ (Fig. 11a). However, patterns of $\delta\mathrm{Kr}_{atm}$ change divide into two regimes: one with collapsed or very weak (< 5 Sv) AMOC, and one with stable AMOC (Fig. 20b). For an MOT anomaly of 1°C in the 25% and 150% wind stress simulations (Fig. 11a), $\delta\mathrm{Kr}_{atm}$ is larger in the collapsed AMOC regime under low wind stress (Fig. 20b).

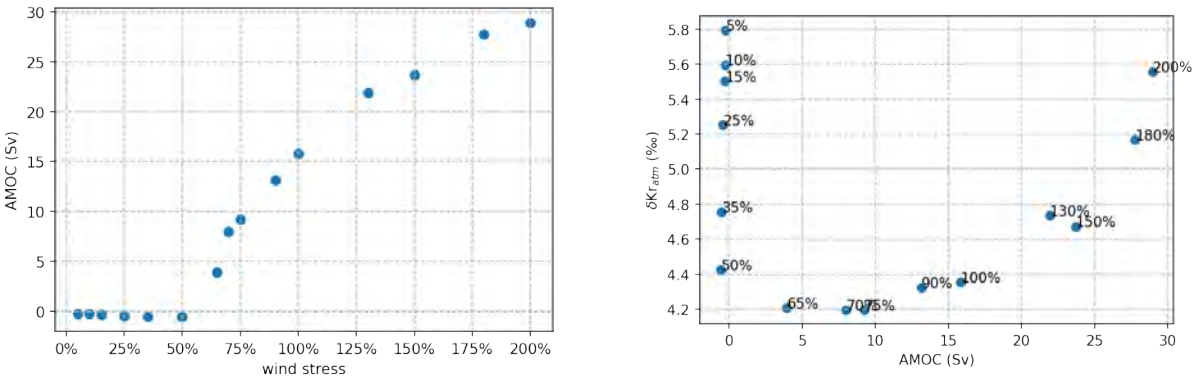

(a) AMOC at 45°N 1158 m depth vs wind stress

(b) $\delta\mathrm{Kr}_{atm}$ vs AMOC at 45°N 1158 m depth

Figure 20: AMOC at 45°N 1158 m depth versus wind stress and $\delta\mathrm{Kr}_{atm}$ versus AMOC at 45°N 1158 m.

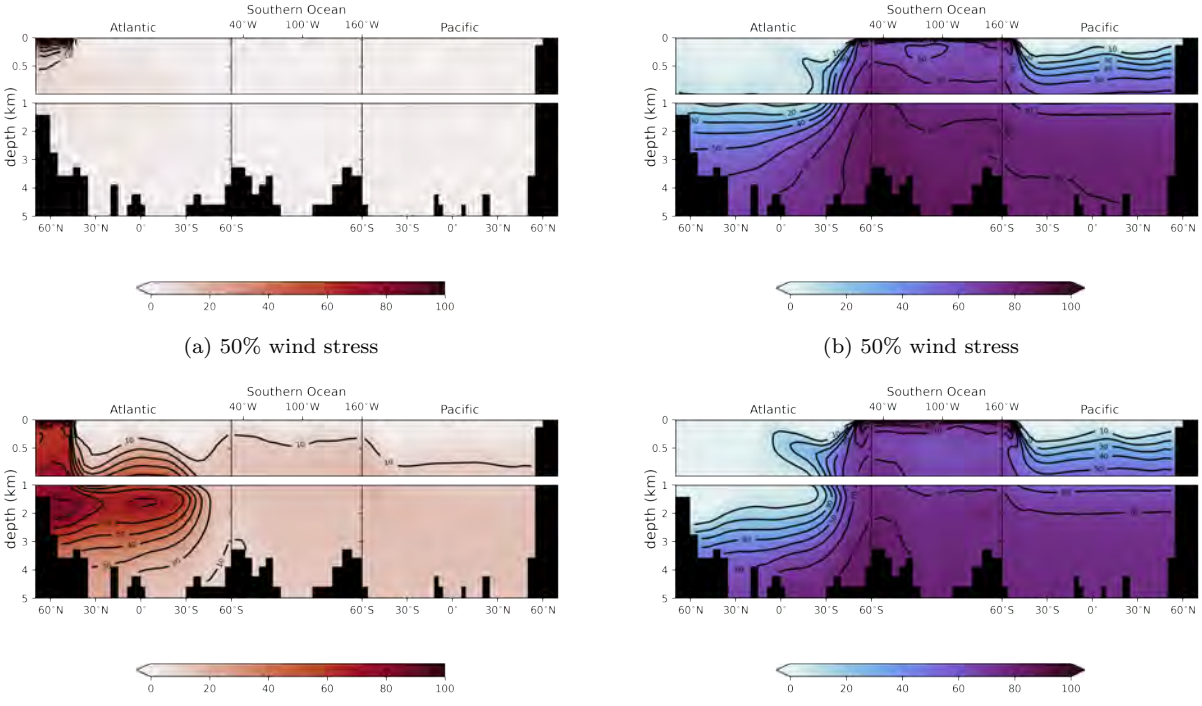

(a) 50% wind stress

(b) 50% wind stress

(c) 70% wind stress

(d) 70% wind stress

Figure 21: NADW (left) and AABW (right) volume percentage in the ocean under 50% and 70% wind stress.

Deep ocean branch of AMOC in the North Atlantic basin is directly related to the formation of NADW. With 20% change in the wind stress, the difference in deep water

formation is exceptionally stark between the 50% and 70% wind stress simulations. A collapsed AMOC in the deep ocean under 50% wind stress corresponds to a vanished NADW. Meanwhile, AABW takes up almost the entire deep ocean below 1 km depth (Fig 21).

As described in section 4.1, when sea ice exists in the Southern Ocean, AABW formed in this region is undersaturated with Kr. Increase in AABW volume percentage therefore implies an increase in undersaturated water masses in the deep ocean. When there is a stable AMOC in the deep ocean, undersaturation in the deep ocean increases as sea ice expands in the Southern Ocean. When AMOC is collapsed, disappearance of NADW in deep ocean further contributes to the expansion of undersaturated water mass in the deep ocean.

The Kr sensitivity tests of AMOC strengths were also performed with the 5-box model. By changing the hydraulic constant k, the absolute value of water flux $|q|$ can be adjusted. However, this further decoupling caused by a collapsed state of AMOC in deep ocean is not observed in 5-box model simulations. This is expected because the setup of the 5-box model determines that there will always be a stable deep ocean circulation as long as $|q| \neq 0$ and water transport exists between the PO and DO boxes.

To further investigate the decoupling in the low-wind-stress regime, 25% and 150% wind stress simulations in the Bern3D 2.0 model are taken as a specific example to be analysed as they have the same MOT. Some important features are compared to understand the difference in the state of oceans in these two simulations (Fig. 22).

The two simulations have roughly similar pattern in their vertical ocean temperature profiles (Fig. 22c and Fig. 22d), which results in their same MOT value. Both have warm surface oceans (above 1 km depth) in the Atlantic and Pacific basins and the coldest water in the bottom of the Southern Ocean.

Nonetheless, when combining the absolute temperature profiles together with their vertical and surface temperature anomaly profiles, prominent differences can be observed in the heat distribution of the two simulations. These anomaly patterns are almost exactly the opposite in the meridional heat distribution.

In the 25% wind stress simulation, heat is centered around low-latitude regions and not transported to the high latitudes due to the weak wind stress and collapsed AMOC. A massive amount of heat is transported downwards from the tropics, especially in the Atlantic basin, resulting in the +1°C MOT anomaly. The Southern Ocean and Arctic surface oceans are cold and covered by sea ice from 60°S (Fig. 22i). Vast extension of sea ice decouples Kr exchange from the cold temperature signal in the Southern Ocean. Kr exchange happens only at the relatively warm surface oceans. The Atlantic basin is highly stratified and does not transport the surface ocean Kr into the deep ocean, leading to higher abundances of Kr in the atmosphere.

In the vertical ocean temperature profile of the 150% wind stress simulation, heat propagates down at mid-latitude region of the Atlantic and Pacific basins. It exhibits a meridionally symmetric pattern dominated by wind-driven circulation. This is also seen in the SST pattern in Fig. 22h, where heat from the low-latitude region is transferred further polewards by strong wind stress. Thus, the poles are warmer and sea ice extension is reduced. The Southern Ocean becomes ice-free (Fig. 22j), which results in a close-to-saturated global ocean (Fig. 22b).

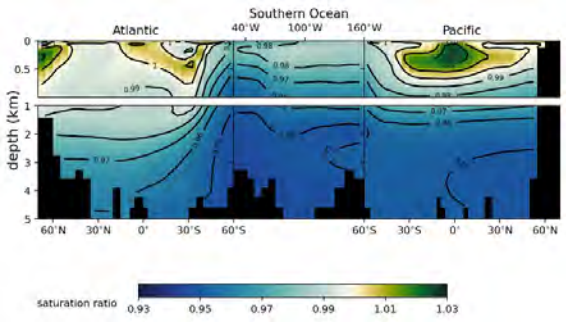

(a) Kr saturation ratio under 25% wind stress

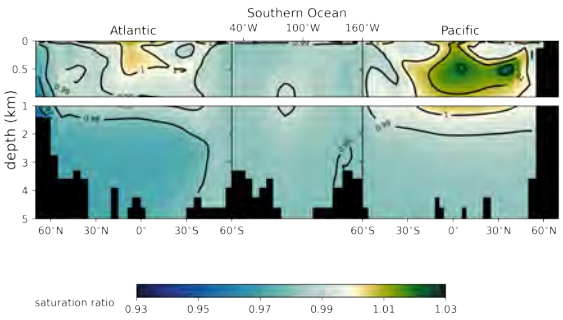

(b) Kr saturation ratio under 150% wind stress

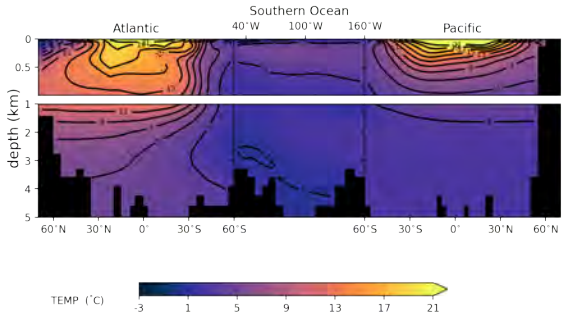

(c) Temperature under 25% wind stress

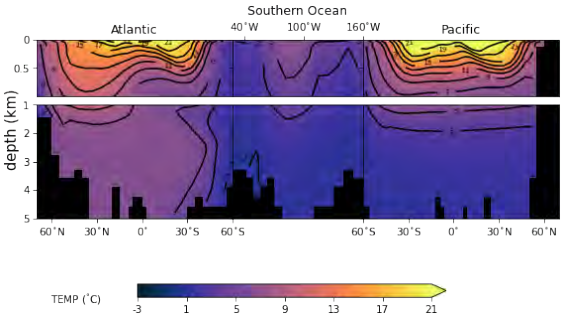

(d) Temperature under 150% wind stress

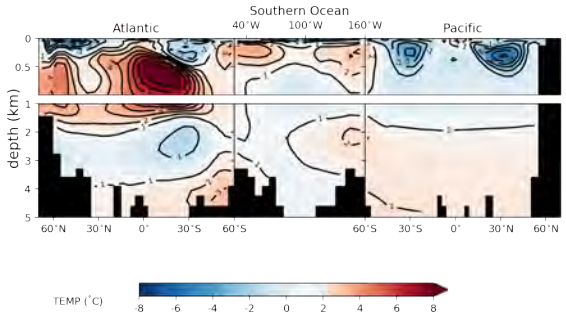

(e) Temperature anomaly under 25% wind stress

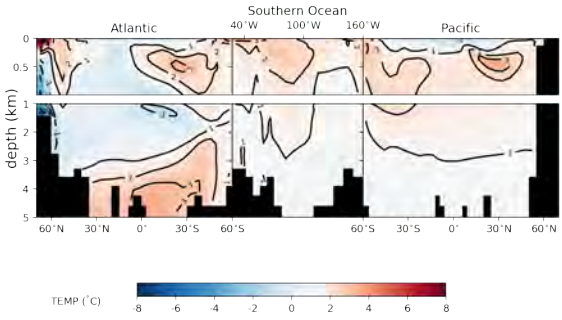

(f) Temperature anomaly under 150% wind stress

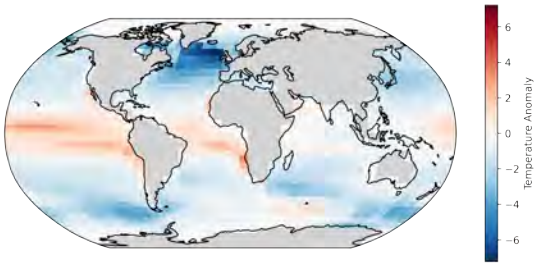

(g) SST anomaly under 25% wind stress

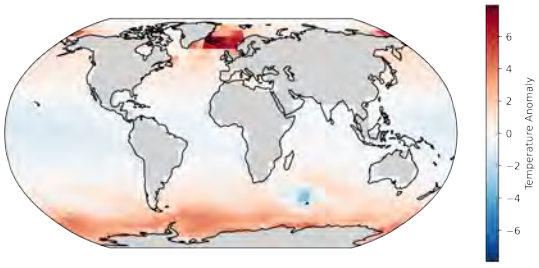

(h) SST anomaly under 150% wind stress

(i) Ice fraction under 25% wind stress

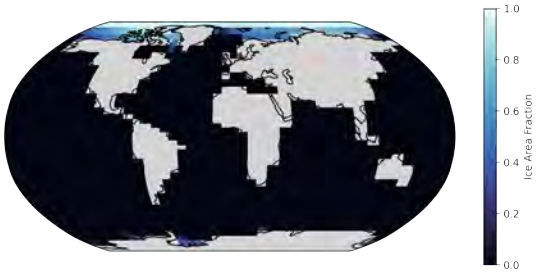

(j) Ice fraction under 150% wind stress

Figure 22: Kr saturation, vertical ocean temperature, temperature anomaly, SST anomaly and ice fraction distribution under 25% and 150% wind stress.

When a stable AMOC exists, supersaturation appears around the equator in both the Atlantic and Pacific basins in the upwelling regions. Cold deep water is being warmed up as it rises to the surface, resulting in a lower Kr solubility. This leads to packets of supersaturated water before excessive Kr can be released at the surface. When AMOC is collapsed, mid-latitude surface oceans are cold as no heat is transported pole-wards. Instead, they are being warmed up from below by the large amount of heat absorbed at the tropics (the dark red blob in Fig. 22e). Therefore, supersaturated region in the Atlantic switched from equatorial region to the mid-latitude.

The fundamental difference between the Kr saturation ratio distribution in the two cases leads to the different $\delta \mathrm{Kr}_{atm}$ values under the same MOT. Therefore, it can be concluded that Kr saturation state instead of the Kr atmospheric abundances is crucial when considering Kr as an MOT proxy. When ocean is 100% saturated everywhere, $\delta \mathrm{Kr}_{atm}$ records the true MOT anomaly via temperature-dependent solubility regardless of the AMOC state.

The opposite heat distribution leading to the same MOT under different AMOC state in the 25% and 150% simulations is an interesting feature. Normally we expect sea surface temperature (SST), MOT and atmosphere temperature to be positively correlated. Just as in the atmospheric CO_2 sensitivity tests, a warmer (colder) atmosphere always corresponds to a warmer (colder) surface ocean or global ocean mean temperature (Fig. 23a). In terms of the amplitude of temperature anomaly change, atmosphere experiences the largest temperature change, MOT anomaly has the smallest amplitude, and the amplitude of SST anomaly change is in between This is expected as seawater has a larger heat capacity than air, and therefore oceans experience a smaller temperature change than the atmosphere in the same simulation.

In the wind stress sensitivity tests, however, this positive correlation among the three temperatures does not hold any more under low wind stress (Fig. 23b). When wind stress is lower than 70%, a collpased AMOC decouples MOT from SST and atmosphere temperature. MOT increases as wind stress decreases below 70%, despite decreasing SST and atmosphere temperature.

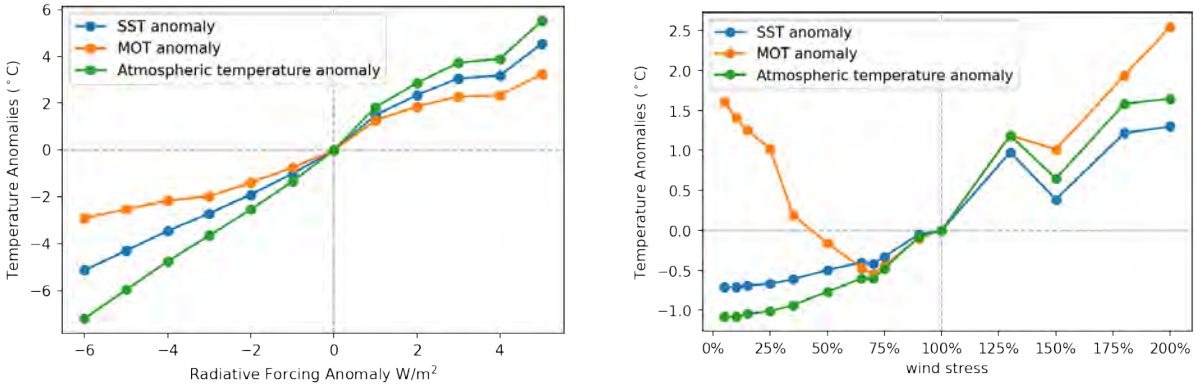

(a) atmospheric CO_2 simulations

(b) wind stress simulations

Figure 23: Anomalies of SST, MOT and atmospheric temperature under different boundary conditions. The cross point of the grey dashed lines marks the control simulation.

According to the change of global mean Kr saturation ratio to the MOT anomaly, dynamics of atmospheric Kr inventories can be roughly divided into three regimes (Fig. 24). In the first regime (indicated by the red dashed line), no sea ice or very little area

of sea ice exists over the Southern Ocean. Global mean Kr saturation ratio remains stable above 98.5%, meaning the global ocean is close to full saturation. In this regime, $\delta\mathrm{Kr}_{atm}/\Delta\mathrm{MOT}$ is the closest to the relation expected from Kr solubility equation.

When global mean saturation ratio is lower than 98.5%, situation distinguishes depending on whether there is a stable AMOC. In the wind stress sensitivity tests where AMOC collapsed below 70% wind stress, the second regime ends at a global mean Kr saturation ratio of around 96.5% (Fig. 24). In the atmospheric CO_2 sensitivity test, nonetheless, where AMOC remains stable, this second regime continues to a much lower global mean Kr saturation ratio of 94% (Fig. 17a).

The second regime (yellow dashed line) represents the process of sea ice gradually expanding until completely covering the AABW formation region. $\delta\mathrm{Kr}_{atm}$ increases as a consequence of MOT decreasing and more Kr dissolving into colder oceans. But less Kr dissolves into the ocean than expected from the solubility equation since saturation ratio decreases proportionally as the Southern Ocean sea ice expands. $\delta\mathrm{Kr}_{atm}$ responds less sensitive to the same MOT change comparing to in the first regime. In this regime, impacts of ice leak and sea ice area, especially of sea ice over the Southern Ocean need to be taken into consideration. Although $\delta\mathrm{Kr}_{atm}/\Delta\mathrm{MOT}$ deviates from the direct calculation from the solubility equation, a firm correlation still exists between $\delta\mathrm{Kr}_{atm}$ and $\Delta\mathrm{MOT}$ signals with calibration on sea-ice impacts accounted for.

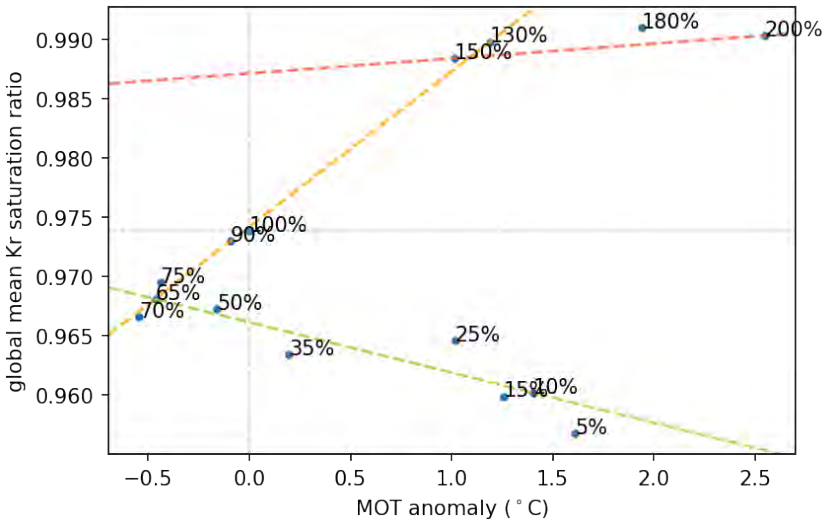

Figure 24: Different phases of global mean Kr saturation ratio in the Bern3D 2.0 model wind stress sensitivity test. Percentages in the plot represent the wind stress to the control simulation.

The third regime (green dashed line) represents a state when the AMOC is collapsed. As MOT rises, less Kr dissolves into warmer ocean. In addition, the decreasing saturation ratio also allows less Kr to dissolve. Jointly, this leads to a much faster increase of atmospheric Kr abundances. No unequivocal evidence show that multi-millennial complete shut-downs of AMOC happened in the 800 kyr time-scale of the ice core measurement concern, nor has the existing noble gas ice core measurements shown strong mismatch of MOT from other temperature reconstructions (Baggenstos et al., 2019; Bereiter et al., 2018b). Therefore, this regime is not considered when interpreting the measured $\delta\mathrm{Kr}_{atm}$ for MOT reconstructions. Nevertheless, the potential of having a short period of collapsed AMOC and its impact on using noble gases as MOT proxies are further discussed in section 5.2.2.

4.3 The LGM Steady State

In recent studies, noble gas mixing ratios are being measured from different ice core samples to reconstruct a reliable MOT record during the past glacial-interglacial cycles (Bereiter et al., 2018b; Shackleton et al., 2019; Haeberli et al., 2020). As the model simulations showed different regimes of $\delta\mathrm{Kr}_{atm}/\Delta\mathrm{MOT}$ relation under different boundary conditions, it is important to inspect the applicability of the temperature-dependent-only $\delta\mathrm{Kr}_{atm}/\Delta\mathrm{MOT}$ relation under glacial period conditions, and determine if additional correction terms need to be added.

Temperature, as directly related to the heat content, is one of the most fundamental features of the state of oceans. Comparing to the PI condition control simulation, oceans are colder everywhere in the LGM simulation. Surface North Atlantic experiences the largest temperature change. The cooling temperature signal from the atmosphere propagates dwon to the deep Atlantic via AMOC. The Southern Ocean has little change in temperature as its temperature is already close to seawater freezing point in the control simulation.

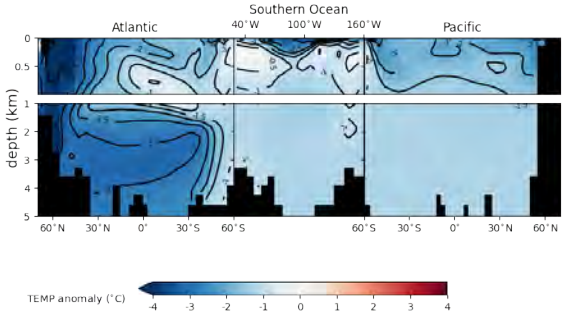

(a) Temperature anomaly

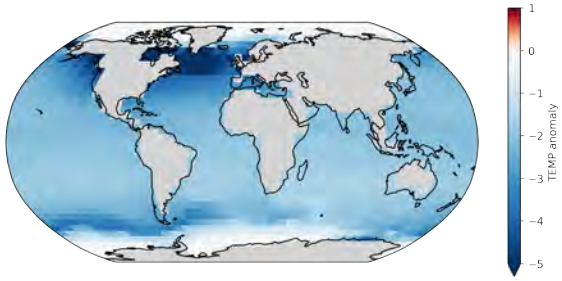

(b) SST anomaly

Figure 25: Bern3D modelled LGM to control simulation temperature anomaly (left) and SST anomaly (right) distribution.

As a consequence of colder SST, sea-ice extension in the LGM simulation expands further equatorwards in both the Southern Ocean and Arctic (Fig 26a) comparing to in the PI control simulation (Fig 13b). This large sea-ice expansion generates large volume of undersaturated water in the LGM deep ocean (Fig 26b). A large part of AABW is even around 6% undersaturated, which leads to a non-negligible deviation from the temperature-dependent-only $\delta\mathrm{Kr}_{atm}/\Delta\mathrm{MOT}$ relation.

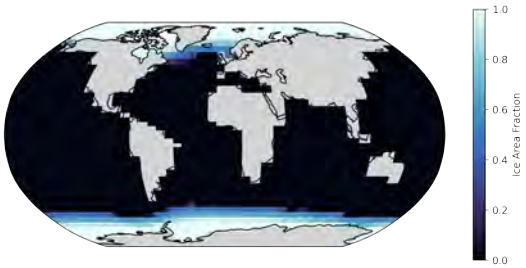

(a) LGM sea-ice area fraction

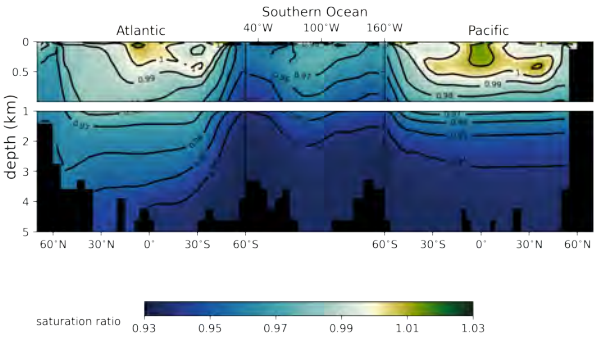

(b) LGM Kr saturation ratio

Figure 26: Modelled fraction of sea-ice area fraction (left) and Kr saturation ratio (right) in the standard LGM simulation.

In terms of the state of deep water formation, NADW under the standard LGM conditions (Fig. 27a) possesses smaller volume in the deep ocean comparing to in the control simulation (Fig. 16a). The presence of NADW in deep ocean indicates that a relatively stable AMOC in the LGM simulation exists.

A scenario with stronger brine rejection during the LGM can be simulated by adding extra salt flux into the Weddell Sea. AABW formation is enhanced with more dense water sinking, and NADW takes up less in the deep ocean. With 0.5 Sv salt flux added, NADW is very weak in the deep ocean but still exists (Fig. 27d). This salt flux sensitivity test shows that a steady AMOC forming NADW during glacial period exists, as it is unlikely to have a situation with so much stronger AABW formation in the Weddell Sea than it already is in the standard LGM simulation.

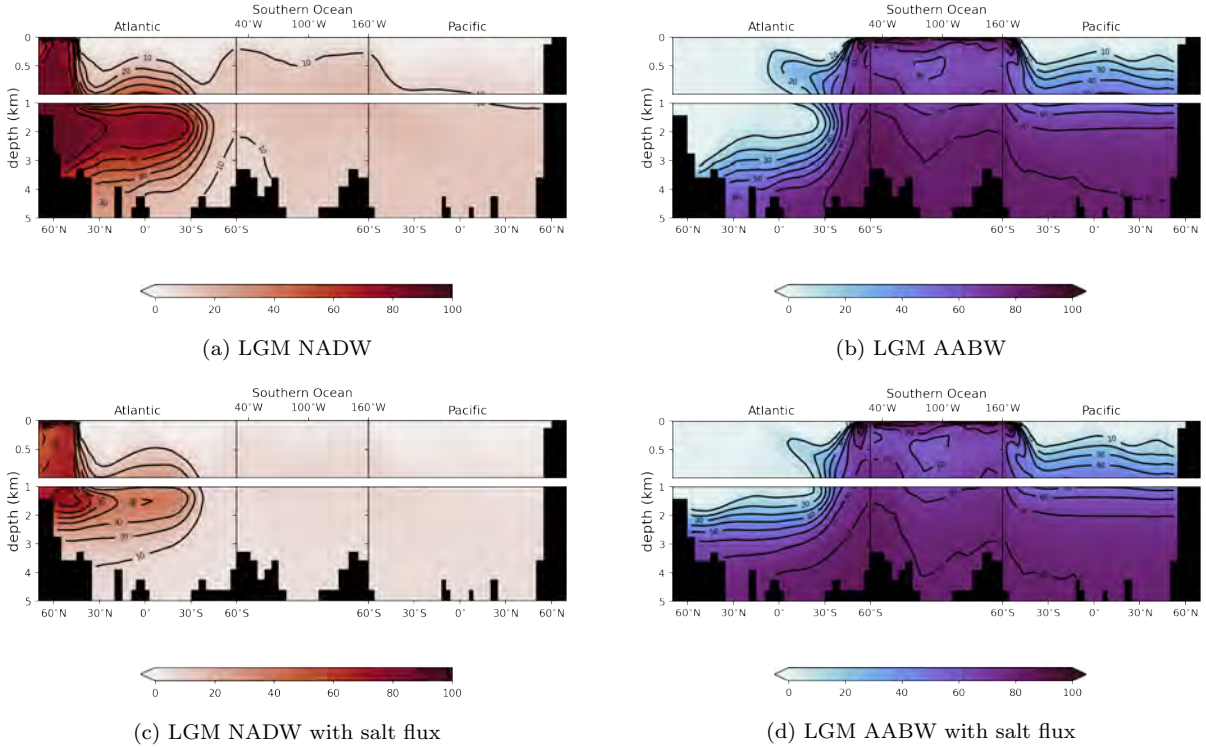

(a) LGM NADW

(b) LGM AABW

(c) LGM NADW with salt flux

(d) LGM AABW with salt flux

Figure 27: Deep water formation in the Bern3D 2.0 model standard LGM simulation (upper row) and LGM simulation with 0.5 Sv extra salt flux added to the Weddell Sea (lower row).

With sea ice over the Southern Ocean and a stable AMOC existing, $\delta \mathrm{Kr}_{atm}/\Delta\mathrm{MOT}$ relation in a standard LGM simulation in the Bern3D 2.0 model falls into the second regime in Fig. 24. It can be therefore assumed that Kr can be used as a reliable proxy for MOT during the LGM with a correction on sea-ice impact made.

It could be argued, though, adding an extra flux of fresh water in the North Atlantic, instead of the salt flux in the Weddell Sea, would be a more realistic way to reduce NADW formation in the past. While adding extra salt flux to enhance AABW formation imitates the situation of more ice formation in the Southern Ocean during glacial period, in Heinrich events the reduction of NADW was caused by the massive amount of iceberg discharges in the North Atlantic (Heinrich, 1988; Rahmstorf, 2002). Fresh water hosing experiments were performed in the Bern3D 2.0 model previously to test the AMOC stability (Pöppelmeier et al., 2021). AMOC did not collapse in LGM simulations even with freshwater relocations larger than 0.1 Sv. Although this result is highly model dependent, we assume here that AMOC remains stable during the LGM.

Another LGM simulation was performed with *iceleak*=1, where there is no sea-ice impact on the noble gas air-sea exchange. The results of LGM simulations are plotted among the wind stress simulations (Fig. 28). $\delta\mathrm{Kr}_{atm}/\Delta\mathrm{MOT}$ in the standard LGM simulation is close to the sensitivity in simulations with wind stress between 70% and 130%. This is the second regime where Kr undersaturation ratio increases as sea-ice expands in the Southern Ocean. For the no-sea-ice-impact LGM simulation, $\delta\mathrm{Kr}_{atm}/\Delta\mathrm{MOT}$ is parallel to the first regime where the Southern Ocean has zero or very little sea ice. Kr undersaturation has not decoupled the deep ocean temperature from Kr atmospheric abundances.

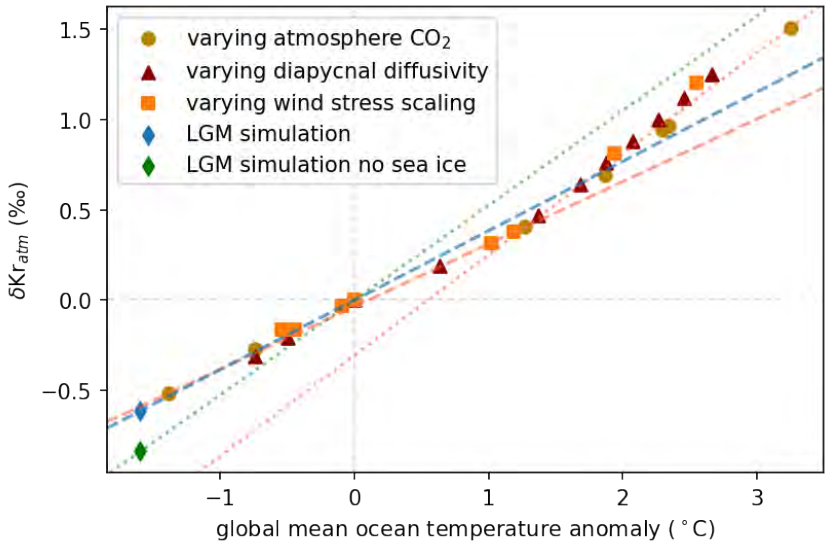

Figure 28: The Bern3D 2.0 model $\delta\mathrm{Kr}_{atm}/\Delta\mathrm{MOT}$ relation comparisons between LGM simulations and sensitivity tests. Dashed blue line indicates the $\delta\mathrm{Kr}_{atm}/\Delta\mathrm{MOT}$ relation in standard LGM simulation. Dotted green line ndicates the $\delta\mathrm{Kr}_{atm}/\Delta\mathrm{MOT}$ relation in an LGM simulation with no sea-ice impact on air-sea exchange.

$\delta\mathrm{Kr}_{atm}$ from two ice-core measurements and the corresponding MOT anomalies converted from the 4-box model are plotted with results from the Bern3D 2.0 model LGM simulations with and without sea-ice impact (Fig. 29). While the two measurements are relatively close to each other, the modelled LGM is around 0.5 to 1.7°C warmer than the ice-core reconstructions considering the measurement uncertainties.

The dashed lines represent the $\delta\mathrm{Kr}_{atm}$ sensitivity to MOT anomaly under the corresponding boundary conditions (LGM simulation with/without sea-ice impact), and indicate the potential $\delta\mathrm{Kr}_{atm}$ values if lower MOTs could be achieved in the Bern3D 2.0 model simulation. The two ice-core reconstructions fall within the sensitivity range of standard LGM and no-sea-ice LGM simulations, and are closer to the no-sea-ice-impact line. This validates that the $\delta\mathrm{Kr}_{atm}/\Delta\mathrm{MOT}$ relation in the Bern3D 2.0 model is close to reality, as impact of sea ice is omitted in the 4-box model by Bereiter et al. (2018b). It is therefore arguable that the current ΔMOTs reconstructed from noble gas proxies all have a constant offset due to the omission of sea-ice impacts. With this offset calibrated, measured $\delta\mathrm{Kr}_{atm}$ may lead to a slightly colder LGM MOT.

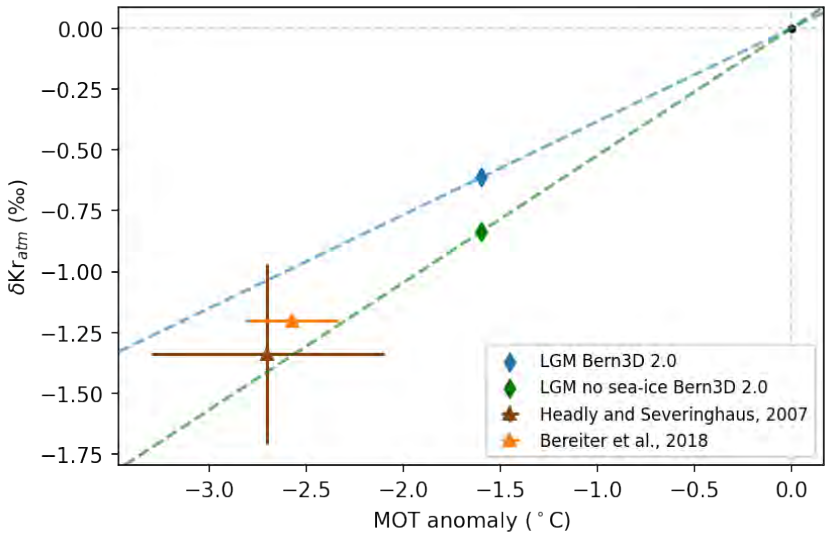

Figure 29: δKr_{atm} and the corresponding estimate of MOT anomalies from Bern3D 2.0 model simulations and ice-core measurements (with error bars). MOT anomaly from (Bereiter et al., 2018b) is between LGM (20 kyr BP) and Holocene (10 kyr BP) instead of the present, and is used as an approximated estimate of the LGM anomaly to present.

MOT in the Bern3D 2.0 standard LGM simulation is around –1.6°C. This is about 1°C warmer on average comparing to the LGM MOTs reconstructed from various noble gas ice-core measurements (Bereiter et al., 2018b; Baggenstos et al., 2019; Haeberli et al., 2020). This is likely due to some missing processes, for instance, aerosol forcing, in the Bern3D 2.0 model because of its reduced complexity. For the purpose of reproducing a colder LGM in model simulation, MOT sensitivity tests are performed with different equilibrium climate sensitivities (ECS) and aerosol forcings (Fig. 30).

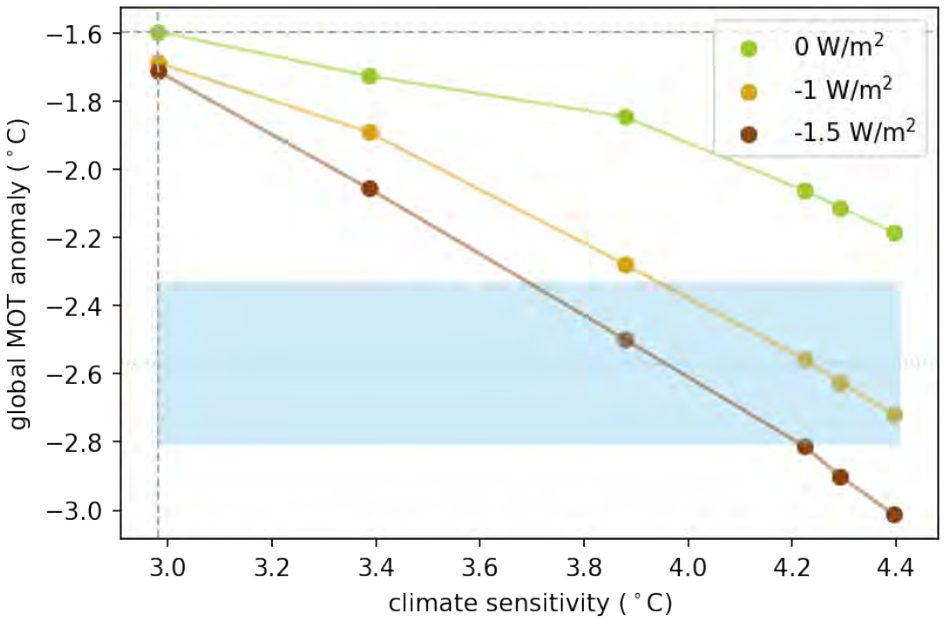

Figure 30: LGM MOT sensitivity tests. Different colours of scatters represent different aerosol forcings. Blue dotted line represents the ice-core reconstructed LGM MOT anomaly of –2.57°C and blue range shows the corresponding measurement uncertainty of ±0.24°C (Bereiter et al., 2018b).

Aerosol forcing is certainly needed for the Bern3D 2.0 model to achieve the LGM MOT from ice-core reconstructions. Studies show that aerosol forcing in the past was around –1W/m^2 (Baggenstos et al., 2019). However, an aerosol forcing of –2.5W/m^2 is required to force LGM MOT to –2.4°C in the Bern3D 2.0 model. For aerosol forcings within the range of –1.5 to –1W/m^2, a climate sensitivity of larger than 3.6°C (under PI condition) is required to obtain the LGM MOTs from ice-core reconstructions. Another possibility of lowering the modelled LGM MOT is by having a higher albedo. The expansion of ice sheet was considered in the Bern3D model but uncertainties in the albedo value may exist. A small increase in the albedo of ice sheet and snow extent can efficiently cool down the simulated LGM.

None of these parameters (ECS, aerosol forcing, albedo) has direct impacts on the physical ocean circulation as the wind stress. Therefore, the colder LGM achieved by varying these parameters has the same stable AMOC as in the standard LGM simulation. The same $\delta\mathrm{Kr}_{atm}/\Delta$MOT relation retains and the modelled $\delta\mathrm{Kr}_{atm}$-ΔMOT point at LGM steady state can fall within the uncertainty range of the ice-core measurements.

5 Conclusion and Discussion

5.1 Conclusion

Sensitivity studies on δKr_{atm} in the Bern3D 2.0 model and the new 5-box model revealed that two factors may influence the reliability of using noble gases as MOT proxies during glacial-interglacial cycles.

The first factor is the sea ice extension, in particular, over the formation region of AABW, which takes up a large percentage of the ocean volume. Air-sea gas exchange is attenuated by sea ice, causing undersaturation of noble gases in the ocean. Global mean saturation ratio of Kr decreases linearly as sea ice expands in the AABW formation region. This undersaturation deviates the $\delta Kr_{atm}/\Delta MOT$ relation from its temperature-dependent-only state.

The impact of sea ice on blocking air-sea gas exchange decrease non-linearly as ice leak increases, and decreases the most rapidly when little gas exchange is allowed from a full-prohibition state. Currently sea ice has been omitted when interpreting measured noble gas mixing ratios in ice cores to MOT anomalies. If 20% of gas exchange is allowed in sea-ice covered regions, omission of sea ice can lead to an offset of around –0.1‰ to –0.2‰ on δKr_{atm} depending on the MOT. This offset is around similar value as the current ice core measurement uncertainty. Although justified, omission of sea ice will result in a constant offset in the ΔMOT interpretation, and with the enhancement in measurement precision, time will soon come that this impact of sea ice may not be negligible anymore. In addition, further study needs to be done on quantitatively defining the ice leak parameter. This would help in better parameterising the process of air-sea gas exchange being blocked by the sea ice in models.

The second factor is the state of AMOC. A collapsed AMOC leads to further decoupling of δKr_{atm} from temperature signals due to surface heat flux distribution. However, the collapse of AMOC alone cannot compromise the reliability of noble gas proxies without a physical process that blocks the air-sea gas exchange. Sea ice or freshwater layers in certain regions can block the noble gas from recording the temperature signals from this region. When AMOC is collapsed, surface temperature distribution is more centred in the tropics and have larger meridional gradient. Noble gas proxies not recording the temperature signals of certain regions can lead to strong decoupling from the MOT. The deficit can be particularly prominent if deep water was formed in this region and hence a much greater volume is affected.

The state of AMOC in history is still being argued, while some proxy studies suggest a collapse of AMOC during certain periods, neither PMIP or the Bern3D model was able to reproduce it in LGM simulations (Pöppelmeier et al., 2021). From the comparisons between the currently available ice-core reconstructions and the modelled LGM, it can be concluded that noble gas proxies can be used as reliable MOT proxies during the LGM, although an offset may exist in the noble gas interpreted ΔMOT if not the impact of sea ice is not properly considered. Potential scenarios when noble gases may not remain reliable anymore during short periods of abrupt change in AMOC are further discussed in section 5.2.2.

Overall, in an ideal situation where noble gases are 100% saturated in the ocean, noble gas mixing ratios reflect the true MOT signals, regardless of any factors. The saturation state decides the reliability of noble gases as MOT proxies for paleocean reconstructions.

5.2 Discussion and Outlook

5.2.1 The Bern3D Model Updates

In this section, updates on the Bern3D model since 2011 and future possible improvements, as well as their impacts on noble gas dynamics, are provided as complementary discussion.

Sensitivity tests of noble gas as MOT proxies were performed earlier by Ritz et al. (2011). Many updates were made on the model since 2011, and results of the same sensitivity tests look very different between now and then. Apart from the fundamental change in resolution described in section 3.1, ocean bottom topography is also updated according to ETOPO5. Some differences in the topography can be seen in Fig. 31 and Fig. 32. Finer resolution leads to different drags at continental edge and change in topography also changes the bottom drag. These changes in drag force have direct impact on ocean circulation.

It was noticed by Müller et al. (2006) that the modelled NADW and surface wind-driven gyre in the Bern3D model at that time was too weak. This is enhanced in the Bern3D 2.0 model. In 2011, Ritz et al. (2011) modelled Drake Passage throughflow to be 45 Sv. In the Bern3D 2.0 model, this throughflow is modelled to be 119 Sv in the control simulation, closer to the 140 Sv observational data than that in the previous Bern3D model. For the region around 40°N, 1 km depth where AMOC is maximum in both versions of the Bern3D model, AMOC strength is around 12 Sv in the earlier version and 16 Sv in the Bern3D 2.0 model (Fig 31).

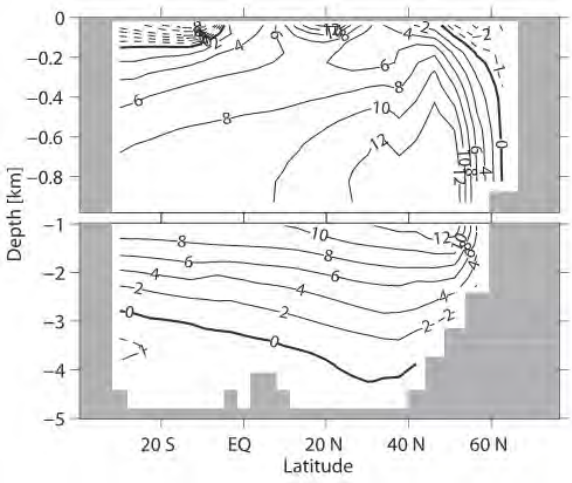

(a) Previous Bern3D AMOC (Ritz et al., 2011)

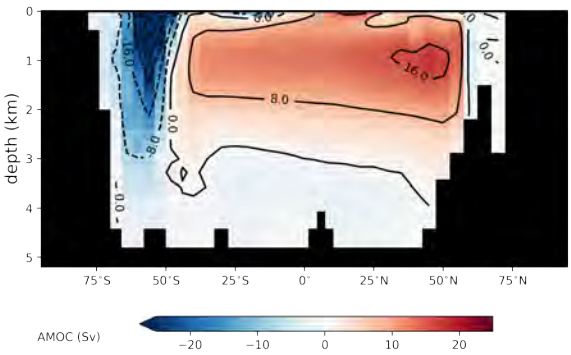

(b) Bern3D 2.0 AMOC

Figure 31: Comparison of modelled AMOC in the control simulation from the 36x36 Bern3D model (left) and the 41x40 Bern3D 2.0 model (right). Note the difference on x-axis range and y-axis scaling.

The temperature profiles are overall very similar in both versions of the model (Fig. 32). Pacific basin in the two versions are mostly the same in temperature distribution pattern and values. The Atlantic basin temperature profile retains the similar pattern after version update, but values have increased by around 3°C at multiple locations, including 3 km depth at the tropics and 1 km depth mid-latitude. This could be the result of a stronger AMOC transporting more heat to the deep ocean (Fig 32).

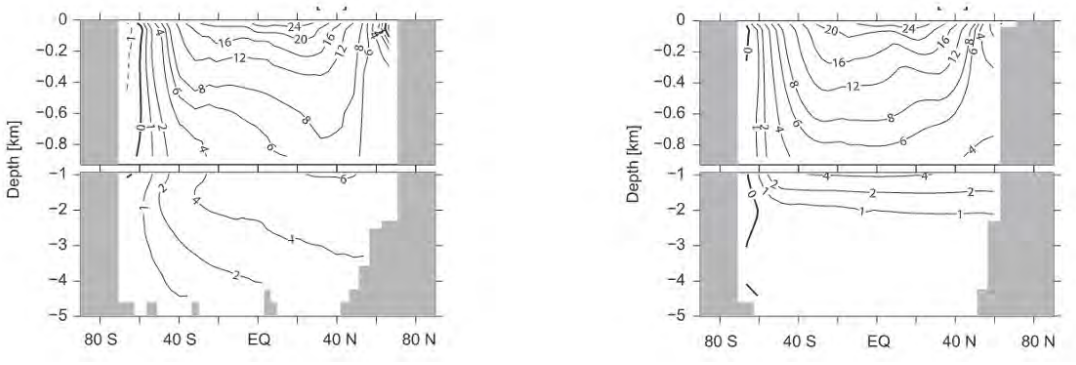

(a) Temperature modelled in the Bern3D before regridding (Ritz et al., 2010)

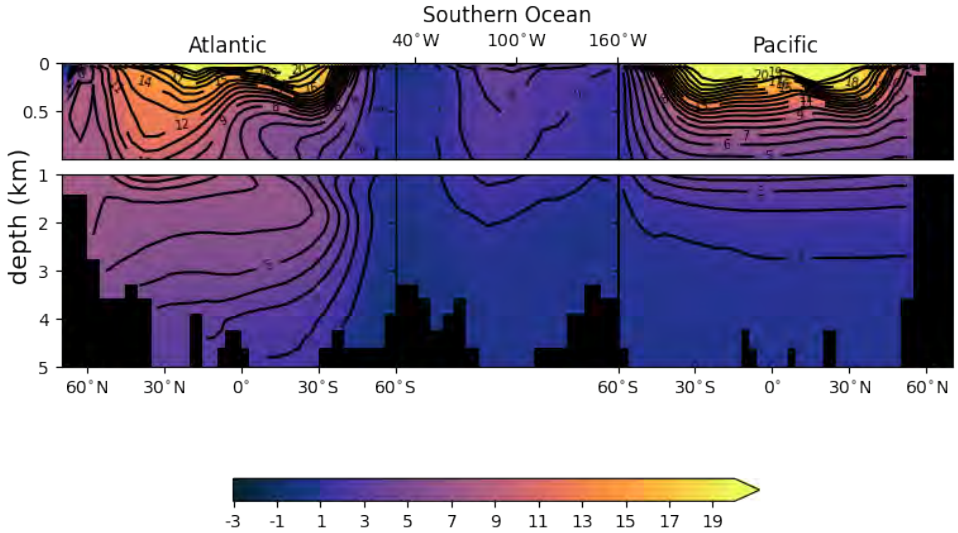

(b) Temperature in the Bern3D 2.0 model control simulation

Figure 32: Comparison of ocean temperature in the control simulation from the 36x36 Bern3D model (a) and the 41x40 Bern3D 2.0 model (b). Note the difference on x-axis range and y-axis scaling. The Atlantic basin in the upper and lower figures are reversed.

Apart from the physical ocean circulation, update was also made on the Schmidt number for gas exchange of noble gases and N_2 in the Bern3D model. The Schmidt number implementation in the 2011 Bern3D model used for the study by Ritz et al. (2011) had a different form where

$$Sc = A_{Sc} + B_{Sc}t + C_{Sc}t^2 + D_{Sc}t^3. \tag{29}$$

t is temperature in °C. The gas specific coefficients have values listed below.

Table 4: Coefficients of Schmidt number least square fit for different gases in the Bern3D model. Coefficients of N_2, Ar and Kr from Wanninkhof (1992) and that of Xe from Ritz et al. (2011). All derived from experiment data from Jähne et al. (1987) and Wilke and Chang (1955). Equation only applies to temperature range between 0°C to 30°C (Wanninkhof, 1992).

Gas	A_{Sc}	B_{Sc}	C_{Sc}	D_{Sc}
N_2	2206.1	–144.86	4.5413	–0.056988
Ar	1909.1	–125.09	3.9012	–0.048953
Kr	2205.0	–135.71	3.9549	–0.047339
Xe	2912.9	–185.99	5.5611	–0.067645

In order to visually observe the difference induced in Kr dynamics by these model updates, sensitivity test results from both versions are plotted together (Fig. 33d). In most simulations in the 2011 Bern3D model, $\delta\mathrm{Kr}_{atm}/\Delta\mathrm{MOT}$ falls on one linear relation (dotted blue lines). This linear relation has the same gradient as the $\delta\mathrm{Kr}_{atm}/\Delta\mathrm{MOT}$ relation in the Bern3D 2.0 model when MOT anomaly is warmer than 1.3°C. This may imply that the first regime, where sea ice has little influence on $\delta\mathrm{Kr}_{atm}$, appears in the range of ΔMOT>–1.5°C in the 2011 Bern3D model.

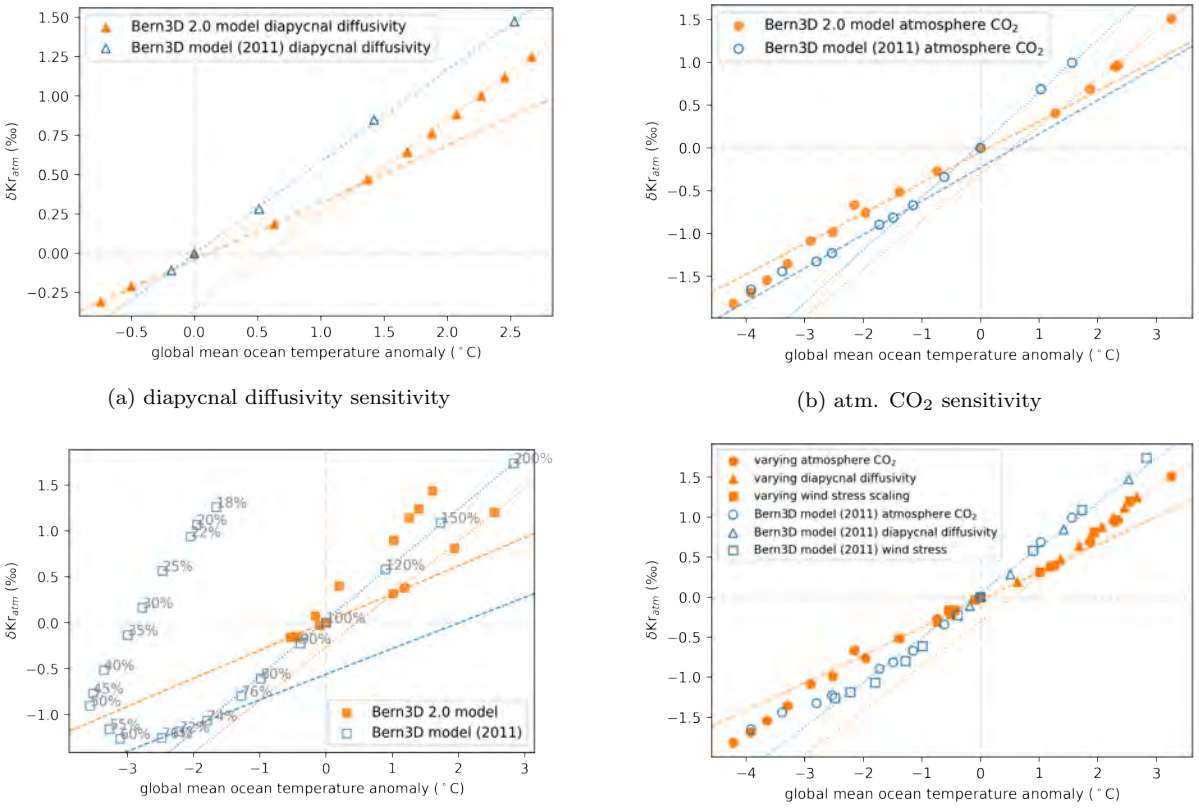

(a) diapycnal diffusivity sensitivity

(b) atm. CO_2 sensitivity

(c) wind stress sensitivity

(d) sensitivities of 3 factors, wind stress above 70% only

Figure 33: $\delta\mathrm{Kr}_{atm}$ sensitivity test comparisons between the Bern3D 2.0 (orange) and the previous 36x36 resolution Bern3D model (blue). Results of the Bern3D model simulations are from Ritz et al. (2011). Dashed and dotted orange lines are for rough indications of $\delta\mathrm{Kr}_{atm}/\Delta\mathrm{MOT}$ relation transition.

When ΔMOT is lower than –1.5°C, simulation results in the 2011 Bern3D model deviate from the dotted blue line. It is suspected that a second regime also exists in the 2011 Bern3D model simulations for –1.5°C> ΔMOT>–3°C. The dashed blue lines in Fig. 33b and Fig. 33c have similar gradient as the orange dashed lines, which represents the second regime of $\delta\mathrm{Kr}_{atm}/\Delta\mathrm{MOT}$ relation in the Bern3D 2.0 model. The enhancement in the Drake Passage throughflow may have led to this shift of temperature ranges of different regimes, as Antarctic Circumpolar Current (ACC) has direct impacts on the sea ice formation and surface air-sea gas exchange at AABW formation region. However, only a few simulations fall within that range and it is therefore difficult to determine if a separate second regime exists in the 2011 Bern3D model.

The third regime of collapsed AMOC leading to further decoupling also appeared in the 2011 Bern3D model low-wind-stress simulations, with the same starting point at 70% wind stress. In the 2011 Bern3D model, change in wind-driven circulation induces larger difference in atmospheric Kr abundances as MOT can be cooled by more than 3 °C with

wind stress change only.

Ritz et al. (2011) also examined the sensitivity of $\delta \mathrm{Kr}_{atm}$ to MOT change with varying atmospheric CO_2 under no-sea-ice conditions (Fig. 34). $\delta \mathrm{Kr}_{atm}$ is more sensitive in the Bern3D 2.0 model than the earlier version with or without sea ice due to stronger ocean circulations in the later version of the model. In both versions of the Bern3D model, $\delta \mathrm{Kr}_{atm}$ shows a stronger sensitivity to MOT with no sea-ice influence.

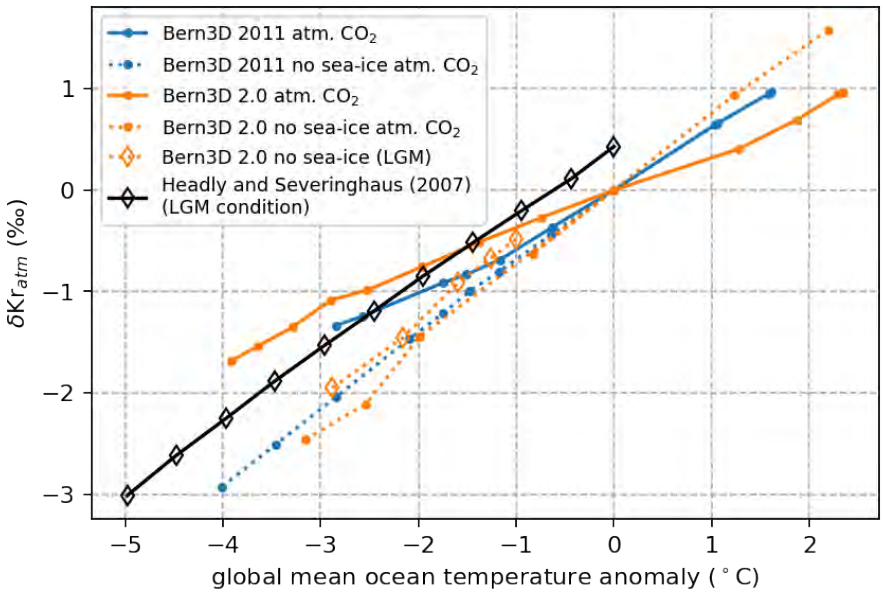

Figure 34: Dashed lines indicating simulations with no sea-ice influence. Rhombic symbols: simulations under LGM conditions. Circles: simulations under preindustrial conditions. Orange: simulations performed with the Bern3D model. Blue: simulations results from the earlier Bern3D model by Ritz et al. (2011). Black: results from the box model by Headly and Severinghaus (2007) under LGM salinity, ocean volume and sea-level pressure. Dashed lines: simulations with no sea-ice influence.

In terms of the LGM ocean, vertical temperature anomaly profiles illustrate the change between modelled LGM temperatures in the two versions of the Bern3D model (Fig. 35). According to the 4-box model set-up described by Bereiter et al. (2018b), the residual ocean during LGM is 2.1°C colder than present, NADW is 3.1°C colder and AABW is 1.1°C colder. A rough estimate can be made on the vertical temperature anomaly profile for the 4-box model, based on the water mass percentages at different depths (Fig.27).

For the surface 500 m, residual ocean takes up more than 50% of the total volume. Assuming NADW and AABW takes up the other 50% of the surface ocean, the temperature anomaly range of the top 500 m ocean is between –2.6°C and –1.6°C.

Between 500 m and 3000 m depth, NADW volume takes up the majority. Since AABW occupies no more than 50% of the volume at this depth, an estimate of temperature anomaly range at this depth is between –3.1°C and –1.1°C.

Below 3000 m, AABW becomes the majority. As NADW takes up less than 50% of the volume, the estimated temperature anomaly range is from –1.6 to –1.1°C.

Comparing to the previous Bern3D model that is too cold at all depths, modelled LGM ocean in the Bern3D 2.0 model matches better the LGM temperature anomaly set-up in the 4-box model used in ice-core studies. The curvature is more realistic with more cooling at the surface than in the deep ocean, as deep ocean is close to the freezing point in the control simulation. This could indicate that updates in the Bern3D 2.0 model overall lead to a better and more realistic ocean circulation.

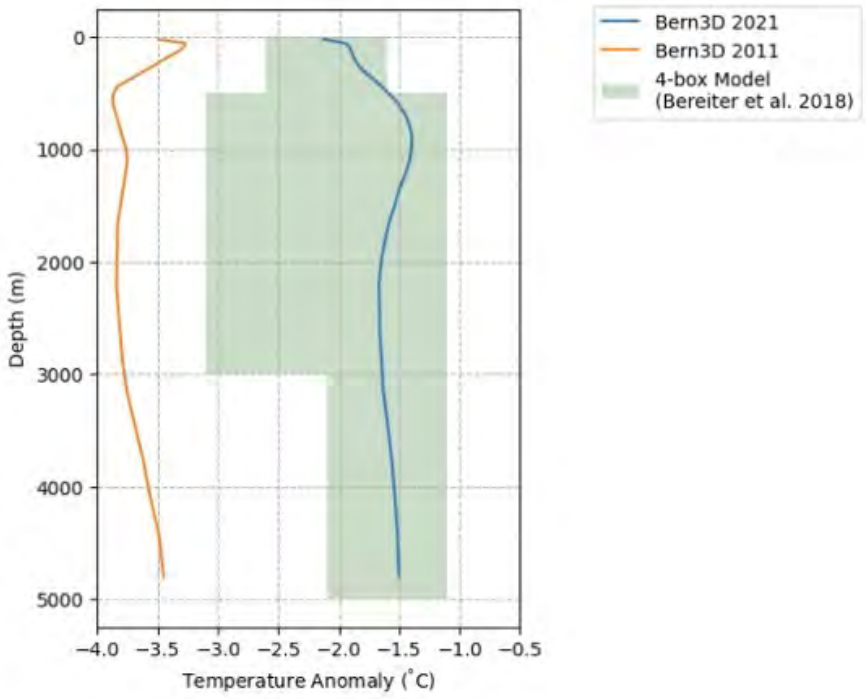

Figure 35: Vertical temperature anomaly profiles of the old and new versions of Bern3D model in comparison with the 4-box model set-up. Data of the 2011 Bern3D modelled LGM vertical temperature profile is taken from Brugger (2013).

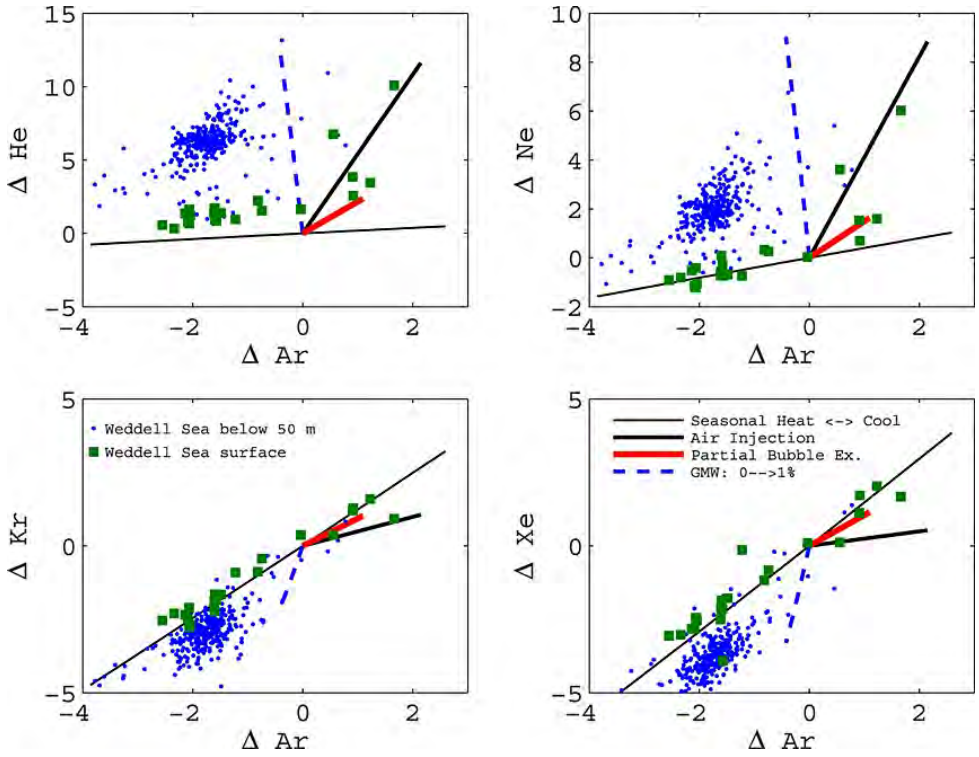

Figure 36: Quantifying impacts from different processes on noble gas saturation: seasonal heating and cooling (thin line), air bubble injection (thicker line), partial bubble exchange (thickest red line), and addition of glacial meltwater (dashed line). Squares representing noble gas samples taken in the top 50 m of Weddell Sea in 2010 and blue dots are from below 50 m (Loose and Jenkins, 2014).

Some improvements on the noble gas implementations could be made for further enhancement of noble gas tracers in the future version of the Bern3D model.

For the gas solubility functions, different forms were proposed to fit experimental data (Weiss and Kyser, 1978; Garcia and Gordon, 1992; Hamme and Emerson, 2004; Jenkins et al., 2019). This is because many processes can lead to excess or deficit anomalies in noble gas saturation, including wave breaking, glacial meltwater, bubble injections and more (Hamme and Severinghaus, 2007; Loose and Jenkins, 2014). The impacts from these processes are quantified and shown in Fig 36.

New implementations of all noble gas solubility are written in the Bern3D 2.0 model but not tested or used in simulations for this thesis. The difference in results is expected to be small, but may still be important as the change of noble gas mixing ratio is in permil. This update is based on a recent study from Jenkins et al. (2019), who suggest that notable biases can appear when applying Eq. 7 at intermediate salinity. They provided a new equation for solubilities of all noble gases with correction by adding a quadratic salinity-dependent term:

All coefficients for different gases involved in the old and new gas solubility implementations are provided in table 5.

Table 5: Solubility function coefficients for noble gases and N_2. Substituting coefficients into different equations leads to different units as noted in the table.

Gas	A_1	A_2	A_3	A_4	B_1	B_2	B_3	C_1
N_2 (μmol/kg) (Hamme and Emerson, 2004)	6.42931	2.92704	2.12504		–7.44129E–3	–8.02566E-3	–1.46775E–2	
Ar (μmol/kg) (Hamme and Emerson, 2004)	2.79150	3.17609	4.13116	4.90379	–6.96233E–3	–7.66670E–3	–1.16888E–2	
Ar (mol/kg) (Jenkins et al., 2019)	–227.4607	305.4347	180.5278	–27.99450	–0.066942	0.037201	–0.0056364	–5.30E–6
Kr (ml/kg) (Weiss and Kyser, 1978)	–112.6840	153.5817	74.4690	–10.0189	–0.011213	–0.001844	0.0011201	
Kr (mol/kg) (Jenkins et al., 2019)	–122.4696	153.5654	70.1969	–8.52524	–0.049522	0.024434	–0.0033968	4.19E–06
Xe (μmol/kg) (Ritz et al., 2011)	–7.48588	5.08763	4.22078		–8.17791E–3	–1.20172E–2		
Xe (mol/kg) (Jenkins et al., 2019)	–224.5100	292.8234	157.6127	–22.66895	–0.084915	0.047996	–0.0073595	6.69E–6

For the benefits of having all noble gas solubility functions expressed in a unified form and updating the solubility coefficients with more recent studies, new solubility equations (Jenkins et al., 2019) and Schmidt number calculations (Wanninkhof, 2014) are implemented for all three noble gases in the Bern3D 2.0 model. However, note that in all simulations involved in this thesis, it is the old solubility and Schmidt number equations implemented by Ritz et al. (2011) applied.

Comparing to solubility equations implemented by Ritz et al. (2011), the saturation concentrations calculated from the new study by Jenkins et al. (2019) are higher in full temperature range for Ar and Kr. The difference in Xe saturation concentration is less between the two different equations. Overall, implementing the new solubility equation can reduce some systematic error in the modelled noble gas tracer results.

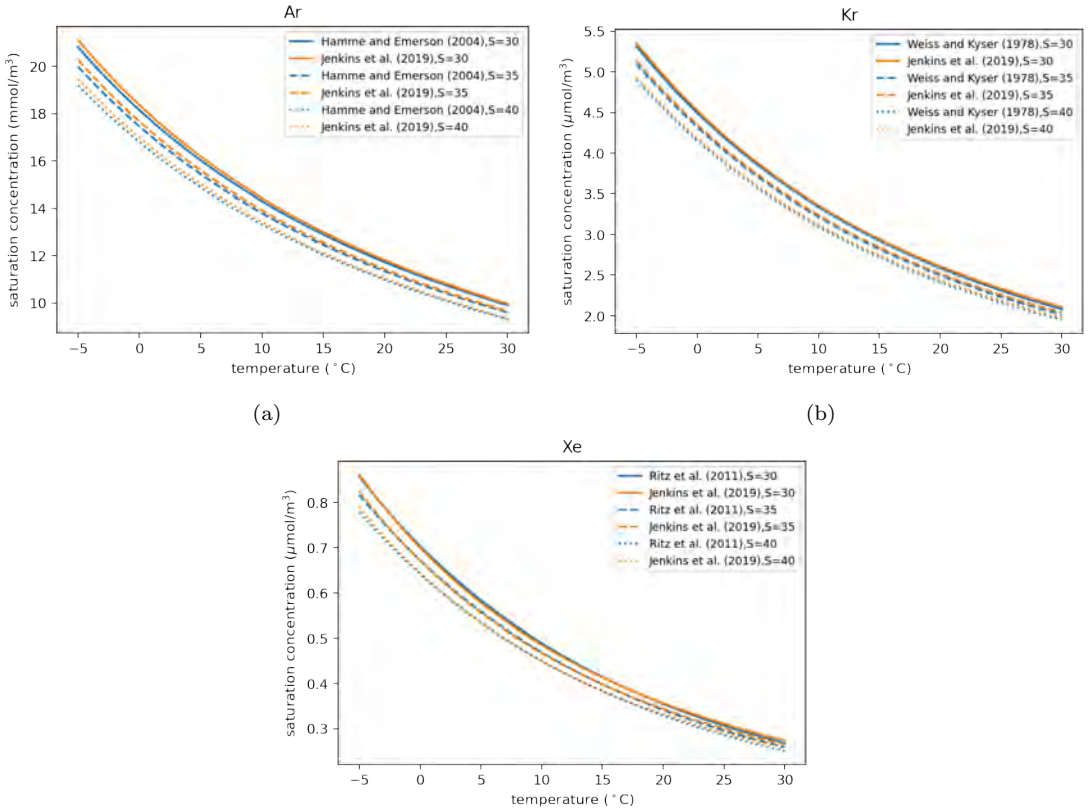

Figure 37: Saturation concentration of different noble gases in different salinities of seawater.

5.2.2 Stability of the AMOC

In order to confirm the reliability of noble gases as MOT proxies, the state of AMOC in the past is of great importance. So far, ice-core measurements mostly agree with temperatures reconstructed from other proxies for the same periods (Bereiter et al., 2018b; Haeberli et al., 2020). However, in this section the discussion is specifically focused on the possible situation when a collapsed AMOC decouples noble gas and temperature signals.

The state of AMOC is considered to be stable most of the time in history and no collapsed state of AMOC was found in the Bern3D 2.0 model LGM simulations (Pöppelmeier et al., 2021). Nonetheless, $^{231}Pa/^{230}Th$ proxy study suggests that AMOC may have experienced a complete elimination during the Heinrich event 17-18 kyr ago and a sharply weakened phase during the Younger Dryas 13 kyr ago (McManus et al., 2004).

In both studies from Shackleton et al. (2019) and Bereiter et al. (2018b), an abrupt warming of MOT during the first half of the Younger Dryas (YD) is noticed. Noble gas proxies from WAIS Divide (WD) ice cores suggest that MOT reached Holocene temperature much faster than global averaged surface temperatures (Bereiter et al., 2018b). Shackleton et al. (2019) hypothesised that this abnormal signal might be caused by some fractionation process altering the noble gas signal in ice cores, as this sudden warming signal is only seen in WD ice cores but not in the Taylor Glacier ice cores. However, evidence is not strong enough to exclude the WD ice core sample. Even the slower warming rate suggested by the Taylor Glacier sample shows 40% faster warming than in Holocene (Levitus et al., 2012).

As the warming rate of MOT during YD suggested by the WD ice core was so out-

standing that so far no model could reproduce it (Shackleton et al., 2019), this leads to a reasonable question whether noble gas proxy is still reliable during YD, or perhaps whether it is decoupled from MOT due to a weakened AMOC. Given its sharply reduced AMOC, YD may fall into the regime where $\delta \mathrm{Kr}_{atm}$ decouples from MOT in the Bern3D 2.0 model simulations with wind stress under 70% (Fig. 18). With a certain measured value of $\delta \mathrm{Kr}_{atm}$, not considering the existence of this third regime with collapsed AMOC can lead to a falsely warmer MOT as a result.

A potential interpretation could be the bipolar seesaw phenomenon, which describes the phenomenon of the phase lag in temperature change of the northern and southern hemispheres (Severinghaus, 2005). The early rise in ice-core reconstructed MOT might be due to noble gas proxies reflecting the warming signals of AABW and AAIW. Surface North Atlantic could still be in the Younger Dryas condition. If the surface of NADW formation region is covered by stratified freshwater layer, this may lead to the result that cold temperature signal at the northern hemisphere is not reflected in noble gases. Although NADW takes up rather small volume in the entire ocean, if NADW temperature signal is the opposite to the southern hemisphere and is not recorded by noble gases, it may still cause large deficit in the ice core records.

Meanwhile, the problem arises that warming rate in the first 700 yeras of YD found in the Taylor Glacier sample is 70% greater than that of Heinrich Stadial 1 (HS1), during which AMOC is expected to be weaker (Shackleton et al., 2019; Levitus et al., 2012). As discussed in section 4.2, the noble gas record is not solely determined by the AMOC state. With strong insolation at high-latitude, noble gas proxies do not necessarily decouple from temperature signal if surface of deep water formation regions are not covered by sea ice. A better understanding on other boundary conditions (SST distribution, sea ice extension etc.) during HS1 and YD is needed in order to further analyse the reliability of their noble gas records.

Current noble gas mixing ratios for MOT reconstructions are only measured for a few limited and discrete periods of time. With more measurements from different sites on YD and Heinrich Stadial periods, reliability of noble gases as MOT proxies can be further investigated in the future. Moreover, other boundary conditions during these periods need to be studied in order to understand the climate system as an entity.

Attempts were made to simulate a second equilibrium with a collapsed AMOC in the newly written 5-box model in this thesis. A conventional approach to simulate an abrupt change in AMOC would be to adjust the evaporation and precipitation fluxes in an ocean-only box model (Marotzke, 2000; Titz et al., 2002; Stocker, 2020) or in high resolution AOGCM (Ferreira et al., 2011). The 5-box model in this thesis is an atmosphere-ocean coupled box model governed by EBM with restoring salinity prescribed instead of a fixed evaporation-precipitation flux. The solution is rather complex to find comparing to in an ocean-only box model, but would certainly be interested to be carried out in the future.

List of Figures

List of Tables

References

Alford, M. H. and Pinkel, R. (2000). Observations of overturning in the thermocline: The context of ocean mixing. *Journal of Physical Oceanography*, 30(5):805 – 832.

Baggenstos, D., Häberli, M., Schmitt, J., Shackleton, S. A., Birner, B., Severinghaus, J. P., Kellerhals, T., and Fischer, H. (2019). Earth's radiative imbalance from the last glacial maximum to the present. *Proceedings of the National Academy of Sciences*, 116(30):14881–14886.

Bereiter, B., Kawamura, K., and Severinghaus, J. P. (2018a). New methods for measuring atmospheric heavy noble gas isotope and elemental ratios in ice core samples. *Rapid Communications in Mass Spectrometry*, 32(10):801–814.

Bereiter, B., Shackleton, S., Baggenstos, D., Kawamura, K., and Severinghaus, J. (2018b). Mean global ocean temperatures during the last glacial transition. *Nature*, 553:39–44.

Berger, A. (1978). Long-term variations of daily insolation and quaternary climatic changes. *Journal of Atmospheric Sciences*, 35:2362–2367.

Broecker, W. S. (1991). The great ocean conveyor. *Oceanography*, 4:79–89.

Brugger, J. (2013). Noble gases as proxies for global mean ocean temperature simulations with the new version of the bern3d model. Bachelor's thesis.

Bryan, S. P. and Marchitto, T. M. (2008). Mg/ca–temperature proxy in benthic foraminifera: New calibrations from the florida straits and a hypothesis regarding mg/li. *Paleoceanography*, 23(2).

Clark, P., Dyke, A., Shakun, J., Carlson, A., Clark, J., Wohlfarth, B., Mitrovica, J., Hostetler, S., and McCabe, A. (2009). The last glacial maximum. *Science*, 325:710 – 714.

Claussen, M., Mysak, L., Weaver, A., Crucifix, M., Fichefet, T., Loutre, M.-F., Weber, S., Alcamo, J., Alexeev, V., Berger, A., Calov, R., Ganopolski, A., Goosse, H., Lohmann, G., Lunkeit, F., Mokhov, I., Petoukhov, V., Stone, P., and Wang, Z. (2002). Earth system models of intermediate complexity: closing the gap in the spectrum of climate system models. *Climate Dynamics*, 18:579–586.

Craig, H. and Wiens, R. C. (1996). Gravitational enrichment of 84kr 36ar ratios in polar ice caps: A measure of firn thickness and accumulation temperature. *Science*, 271(5256):1708–1710.

Cury, P., Bakun, A., Crawford, R., Jarre, A., Quiñ, R., Shannon, L., Verheye, H., and Quinones, R. (2000). Small pelagics in upwelling systems: Patterns of interaction and structural changes in "wasp-waist" ecosystems. *ICES Journal of Marine Science*, 57:603–618.

Edwards, N. R., Willmott, A. J., and Killworth, P. D. (1998). On the role of topography and wind stress on the stability of the thermohaline circulation. *Journal of Physical Oceanography*, 28(5):756 – 778.

Ferreira, D., Marshall, J., and Rose, B. (2011). Climate determinism revisited: Multiple equilibria in a complex climate model. *Journal of Climate*, 24:992–1012.

Garcia, H. E. and Gordon, L. I. (1992). Oxygen solubility in seawater: Better fitting equations. *Limnology and Oceanography*, 37(6):1307–1312.

Gleckler, P. J., Durack, P. J., Stouffer, R. J., Johnson, G. C., and Forest, C. E. (2016). Industrial-era global ocean heat uptake doubles in recent decades. *Nature Climate Change*, 6(4):394–398.

Gruber, N. (2004). The dynamics of the marine nitrogen cycle and its influence on atmospheric co2 variations. In Follows, M. and Oguz, T., editors, *The Ocean Carbon Cycle and Climate*, pages 97–148, Dordrecht. Springer Netherlands.

Haeberli, M., Baggenstos, D., Schmitt, J., Grimmer, M., Michel, A., Kellerhals, T., and Fischer, H. (2020). Snapshots of mean ocean temperature over the last 700,000 yr using noble gases in the epica dome c ice core. *Climate of the Past Discussions*, 2020:1–38.

Hamme, R. and Emerson, S. (2004). The solubility of neon, nitrogen and argon in distilled water and seawater. *Deep Sea Research Part I Oceanographic Research Papers*, 51:1517–1528.

Hamme, R. C. and Severinghaus, J. P. (2007). Trace gas disequilibria during deep-water formation. *Deep Sea Research Part I: Oceanographic Research Papers*, 54(6):939–950.

Headly, M. and Severinghaus, J. (2007). A method to measure kr/n2 ratios in air bubbles trapped in ice cores and its application in reconstructing past mean ocean temperature. *Journal of Geophysical Research*, 112.

Heinrich, H. (1988). Origin and consequences of cyclic ice rafting in the northeast atlantic ocean during the past 130,000 years. *Quaternary Research*, 29:142–152.

Hopcroft, P. O., Valdes, P. J., Woodward, S., and Joshi, M. M. (2015). Last glacial maximum radiative forcing from mineral dust aerosols in an earth system model. *Journal of Geophysical Research: Atmospheres*, 120(16):8186–8205.

Jenkins, W., Lott, D., and Cahill, K. (2019). A determination of atmospheric helium, neon, argon, krypton, and xenon solubility concentrations in water and seawater. *Marine Chemistry*, 211:94–107.

Johnson, G. C. (2008). Quantifying antarctic bottom water and north atlantic deep water volumes. *Journal of Geophysical Research: Oceans*, 113(C5).

Jähne, B., Heinz, G., and Dietrich, W. (1987). Measurement of the diffusion coefficients of sparingly soluble gases in water. *Journal of Geophysical Research: Oceans*, 92(C10):10767–10776.

Kalnay, E., Kanamitsu, M., Kistler, R., Collins, W., Deaven, D., Gandin, L., Iredell, M., Saha, S., White, G., Woollen, J., Zhu, Y., Chelliah, M., Ebisuzaki, W., Higgins, W., Janowiak, J., Mo, K. C., Ropelewski, C., Wang, J., Leetmaa, A., Reynolds, R., Jenne, R., and Joseph, D. (1996). The ncep/ncar 40-year reanalysis project. *Bulletin of the American Meteorological Society*, 77(3):437 – 472.

Lake, R. A. and Lewis, E. L. (1970). Salt rejection by sea ice during growth. *Journal of Geophysical Research (1896-1977)*, 75(3):583–597.

Lambeck, K., Rouby, H., Purcell, A., Sun, Y., and Sambridge, M. (2014). Sea level and global ice volumes from the last glacial maximum to the holocene. *Proceedings of the National Academy of Sciences*, 111(43):15296–15303.

Lea, D. (2014). *Elemental and Isotopic Proxies of Past Ocean Temperatures*, volume 8, pages 373–397. Oxford: Elsevier.

Levitus, S., Antonov, J., Boyer, T., Baranova, O., Garcia, H., Locarnini, R., Mishonov, A., Reagan, J., Seidov, D., Yarosh, E., and Zweng, M. (2012). World ocean heat content and thermosteric sea level change (0–2000 m), 1955–2010. *Geophysical Research Letters*, 39:1–5.

Loose, B. and Jenkins, W. J. (2014). The five stable noble gases are sensitive unambiguous tracers of glacial meltwater. *Geophysical Research Letters*, 41(8):2835–2841.

Lüthi, D., Floch, M., Bereiter, B., Blunier, T., Barnola, J.-M., Siegenthaler, U., Raynaud, D., Jouzel, J., Fischer, H., Kawamura, K., and Stocker, T. (2008). High-resolution carbon dioxide concentration record 650,000-800,000 years before present. *Nature*, 453:379–82.

MacKinnon, J., St Laurent, L., and Naveira Garabato, A. C. (2013). Chapter 7 - diapycnal mixing processes in the ocean interior. In Siedler, G., Griffies, S. M., Gould, J., and Church, J. A., editors, *Ocean Circulation and Climate*, volume 103 of *International Geophysics*, pages 159–183. Academic Press.

Marotzke, J. (2000). Abrupt climate change and thermohaline circulation: Mechanisms and predictability. *Proceedings of the National Academy of Sciences of the United States of America*, 97:1347–50.

Masson-Delmotte, V., Schulz, M., Abe-Ouchi, A., Beer, J., Ganopolski, A., Rouco, J. G., Jansen, E., Lambeck, K., Luterbacher, J., Naish, T., Osborn, T., Otto-Bliesner, B., Quinn, T., Ramesh, R., Rojas, M., Shao, X., and Timmermann, A. (2013). *Information from Paleoclimate Archives*, page pp. 383–464. Cambridge University Press.

Masson-Delmotte, V., Zhai, P., Pirani, A., Connors, S., Péan, C., Berger, S., Caud, N., Chen, Y., Goldfarb, L., Gomis, M., Huang, M., Leitzell, K., Lonnoy, E., J.B.R., Matthews, Maycock, T., Waterfield, T., Yelekçi, O., Yu, R., and (eds.), B. Z. (2021). Cambridge University Press. In Press.

McManus, J., François, R., Gherardi, J., Keigwin, L., and Brown-Leger, S. (2004). Collapse and rapid resumption of atlantic meridional circulation linked to deglacial climate changes.

Mix, A. C., Bard, E., and Schneider, R. (2001). Environmental processes of the ice age: land, oceans, glaciers (epilog). *Quaternary Science Reviews*, 20:627–657.

Mueller, S., Joos, F., Plattner, G.-K., Edwards, N., and Stocker, T. (2008). Modeled natural and excess radiocarbon: Sensitivities to the gas exchange formulation and ocean transport strength. *Global Biogeochem. Cycles*, 22.

Müller, S. A., Joos, F., Edwards, N. R., and Stocker, T. F. (2006). Water mass distribution and ventilation time scales in a cost-efficient, three-dimensional ocean model. *Journal of Climate*, 19(21):5479 – 5499.

National Oceanic and Atmospheric Administration (2021). The global conveyor belt: Currents tutorial. Access date: 2021-11-14.

Nehrbass-Ahles, C. (2017). *Millennial-scale atmospheric CO_2 reconstructions using multiple Antarctic ice cores*. dissertation, University of Bern.

Pan, S., Contreras, M., Romero, J., Reyes, A., Chattaraj, P., and Merino, G. (2013). C5li7+ and o2li 5+ as noble-gas-trapping agents. *Chemistry (Weinheim an der Bergstrasse, Germany)*, 19.

Peltier, W. (2004). Global glacial isostasy and the surface of the ice-age earth: The ice-5g (vm2) model and grace. *Annual Review of Earth and Planetary Sciences*, 32(1):111–149.

Pöppelmeier, F., Scheen, J., Jeltsch-Thömmes, A., and Stocker, T. F. (2021). Simulated stability of the atlantic meridional overturning circulation during the last glacial maximum. *Climate of the Past*, 17(2):615–632.

Rahmstorf, S. (2002). Ocean circulation and climate during the past 120,000 years. *Nature*, 419:207–14.

Randall, D., Wood, R., Bony, S., Colman, R., Fichefet, T., Fyfe, J., Kattsov, V., Pitman, A., Shukla, J., Srinivasan, J., Ronald, S., Sumi, A., and Taylor, K. (2007). *Climate Models and Their Evaluation*.

Rhein, M., Rintoul, S., Aoki, S., Campos, E., Chambers, D., Feely, R., Gulev, S., Johnson, G., Josey, S., Kostianoy, A., Mauritzen, C., Roemmich, D., Talley, L., and Wang, F. (2013). *Observations: Ocean*, page 255–315. Cambridge University Press.

Ritz, S., Stocker, T., and Joos, F. (2010). A coupled dynamical ocean - energy balance atmosphere model for paleoclimate studies. *Journal of Climate - J CLIMATE*, 24.

Ritz, S. P. (2013). *The Bern3D Coupled Ocean-Atmosphere Climate Model*. University of Bern.

Ritz, S. P., Stocker, T. F., and Severinghaus, J. P. (2011). Noble gases as proxies of mean ocean temperature: sensitivity studies using a climate model of reduced complexity. *Quaternary Science Reviews*, 30(25):3728–3741.

Roemmich, D., Church, J., Gilson, J., Monselesan, D., Sutton, P., and Wijffels, S. (2015). Unabated planetary warming and its ocean structure since 2006. *Nature Climate Change*, 5(3):240–245.

Roth, R. (2013). *Modeling forcings and responses in the global carbon cycle-climate system: Pas, present and future*. dissertation, University of Bern.

Sarmiento, J. L. and Gruber, N. (2006). *Tracer Conservation and Ocean Transport*, pages 19–72. Princeton University Press.

Scheen, J. and Stocker, T. F. (2020). Effect of changing ocean circulation on deep ocean temperature in the last millennium. *Earth System Dynamics*, 11(4):925–951.

Schlesinger, W. (1997). *Introduction: The Ocean's Meridional Overturning Circulation*, pages 1–588. Academic Press, 2 edition.

Schmittner, A., Chiang, J. C., and Hemming, S. R. (2007). *Introduction: The Ocean's Meridional Overturning Circulation*, pages 1–4. American Geophysical Union (AGU).

Schwander, J. (1996). Gas diffusion in firn. In Wolff, E. W. and Bales, R. C., editors, *Chemical Exchange Between the Atmosphere and Polar Snow*, pages 527–540, Berlin, Heidelberg. Springer Berlin Heidelberg.

Severinghaus, J. (2005). Southern see-saw seen.

Shackleton, S., Bereiter, B., Baggenstos, D., Bauska, T. K., Brook, E. J., Marcott, S. A., and Severinghaus, J. P. (2019). Is the noble gas-based rate of ocean warming during the younger dryas overestimated? *Geophysical Research Letters*, 46(11):5928–5936.

Sigl, M., Buizert, C., Fudge, T. J., Winstrup, M., Cole-Dai, J., McConnell, J. R., Ferris, D. G., Rhodes, R. H., Taylor, K. C., Welten, K. C., Woodruff, T. E., Adolphi, F., Baggenstos, D., Brook, E. J., Caffee, M. W., Clow, G. D., Cheng, H., Cuffey, K. M., Dunbar, N. W., Edwards, R. L., Edwards, L., Geng, L., Iverson, N., Koffman, B. G., Layman, L., Markle, B. R., Maselli, O. J., McGwire, K. C., Muscheler, R., Nishiizumi, K., Pasteris, D. R., Severinghaus, J. P., Sowers, T. A., and Steig, E. J. (2019). WAIS Divide Deep ice core 0-68 ka WD2014 chronology.

Stanley, R. H. R., Jenkins, W. J., Lott III, D. E., and Doney, S. C. (2009). Noble gas constraints on air-sea gas exchange and bubble fluxes. *Journal of Geophysical Research: Oceans*, 114(C11).

Stocker, T. F. (2013). Chapter 1 - the ocean as a component of the climate system. In Siedler, G., Griffies, S. M., Gould, J., and Church, J. A., editors, *Ocean Circulation and Climate*, volume 103 of *International Geophysics*, pages 3–30. Academic Press.

Stocker, T. F. (2020). Introduction to climate modeling.

Stocker, T. F., Mysak, L. A., and Wright, D. G. (1992). A zonally averaged, coupled ocean-atmosphere model for paleoclimate studies. *Journal of Climate*, 5(8):773 – 797.

Stockli, R., NASA/Goddard Space Flight Center Scientific Visualization Studio, The Blue Marble Next Generation, and NASA's Earth Observatory (2008). The thermohaline circulation - the great ocean conveyor belt. Access date: 2021-11-14.

Stommel, H. (1961). Thermohaline convection with two stable regimes of flow. *Tellus*, 13(2):224–230.

Talley, L., Pickard, G., Emery, W., and Swift, J. (2011). Descriptive physical oceanography: An introduction: Sixth edition. *Descriptive Physical Oceanography: An Introduction: Sixth Edition*, pages 1–555.

Titz, S., Kuhlbrodt, T., Rahmstorf, S., and Feudel, U. (2002). On freshwater-dependent bifurcations in box models of the interhemispheric thermohaline circulation. *Tellus A*.

Veres, D., Bazin, L., Landais, A., Toyé Mahamadou Kele, H., Lemieux-Dudon, B., Parrenin, F., Martinerie, P., Blayo, E., Blunier, T., Capron, E., Chappellaz, J., Rasmussen, S. O., Severi, M., Svensson, A., Vinther, B., and Wolff, E. W. (2013). The antarctic ice core chronology (aicc2012): an optimized multi-parameter and multi-site dating approach for the last 120 thousand years. *Climate of the Past*, 9(4):1733–1748.

Wanninkhof, R. (1992). Relationship between wind speed and gas exchange over the ocean. *Journal of Geophysical Research: Oceans*, 97(C5):7373–7382.

Wanninkhof, R. (2014). Relationship between wind speed and gas exchange over the ocean revisited. *Limnology and Oceanography: Methods*, 12(6):351–362.

Weiss, R. F. and Kyser, T. K. (1978). Solubility of krypton in water and sea water. *Journal of Chemical and Engineering Data*, 69-72.

Wilke, C. R. and Chang, P. (1955). Correlation of diffusion coefficients in dilute solutions. *AIChE Journal*, 1(2):264–270.

Winckler, G. and Severinghaus, J. (2013). *Noble Gases in Ice Cores: Indicators of the Earth's Climate History*, pages 33–53.

Wood, D. and Caputi, R. (1966). Solubilities of kr and xe in fresh and sea water. page 20.

Appendix A Figures

For Kr sensitivity tests, simulations were run under pre-industrial conditions for 10 kyr to reach equilibrium. This time is justified (Fig. A1) as the time for Kr to reach equilibrium is around 6 kyr and an extra 4 kyr was run to guarantee a full equilibrium is reached.

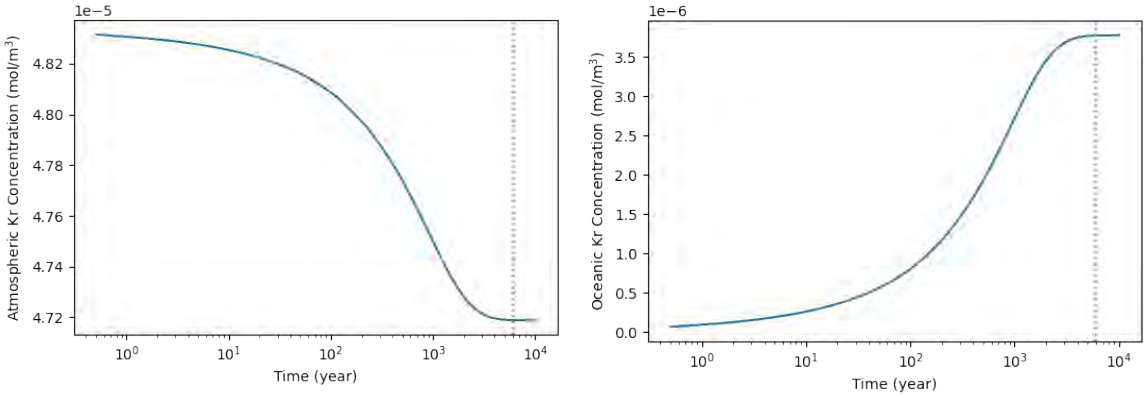

(a) Atmospheric Kr inventory

(b) Oceanic Kr inventory

Figure A1: Krypton inventories equilibrium in the Bern3D 2.0 model control simulation with logarithmically scaled time. Dotted grey lines mark 6 kyr in the simulation time.

Ideal age of the ocean under 50% and 70% wind stress are plotted to track the time when water masses were last in contact with the atmosphere. With only 20% change in the wind stress, ideal age of water in the 50% wind stress simulation appears to be much older and almost doubled compared to in the 70% wind stress simulation. This shows how slowly deep ocean is being ventilated after AMOC collapses. Under stronger wind stress, a well ventilated ocean can quickly dissolve Kr again at the surface and hence is less undersaturated.

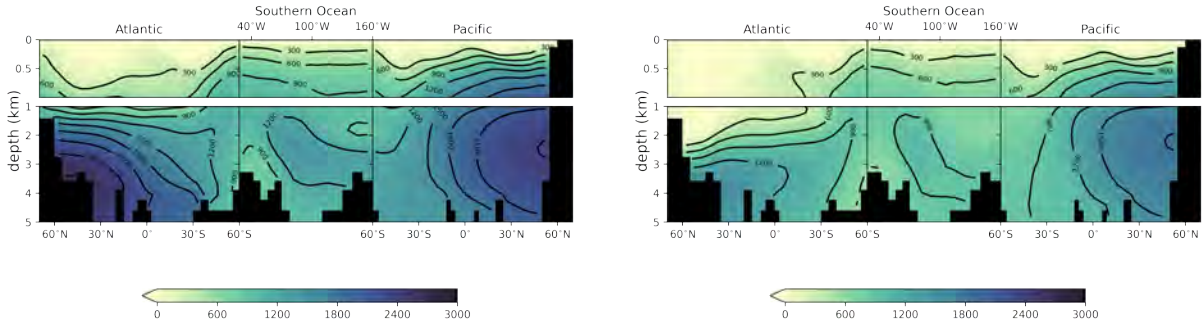

(a) ideal age at 50% wind stress

(b) ideal age at 70% wind stress

Figure A2: Ideal age of water masses under 50% and 70% wind stress in the Bern3D 2.0 model.

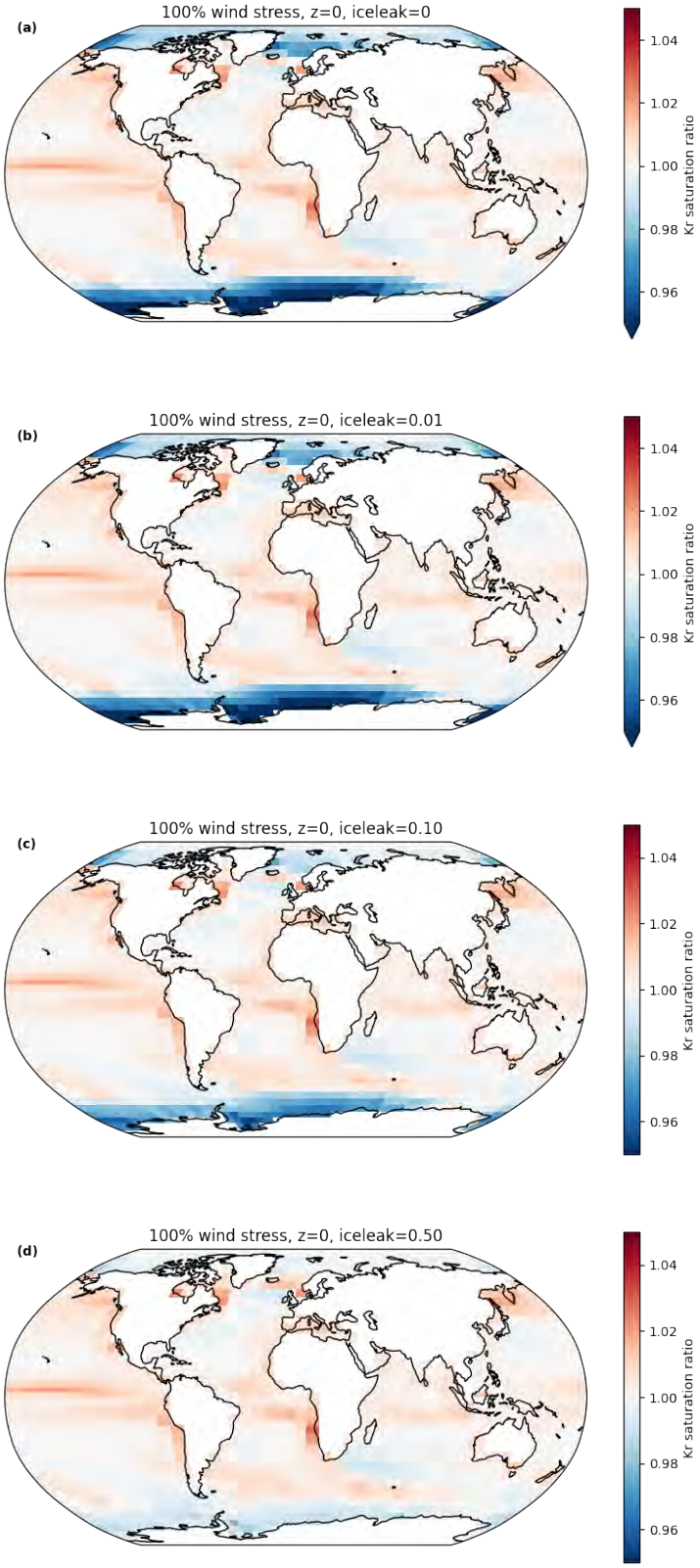

Figure A3: Surface Kr saturation ratio in the Bern3D 2.0 model simulations with different ice leak values.

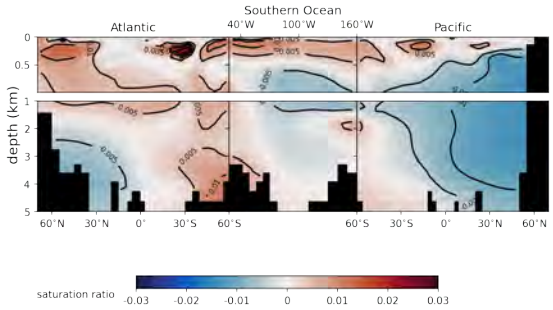

(a) 25% minus 50% wind stress Kr saturation ratio

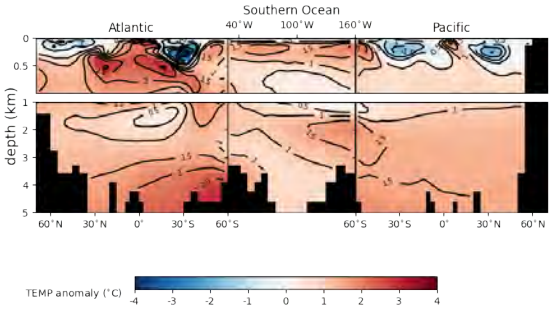

(b) 25% minus 50% wind stress temperature

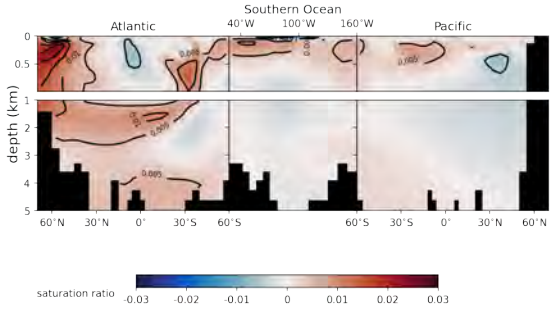

(c) 50% minus 70% wind stress Kr saturation ratio

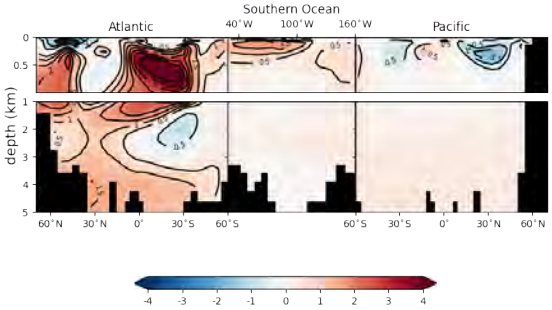

(d) 50% minus 70% wind stress temperature

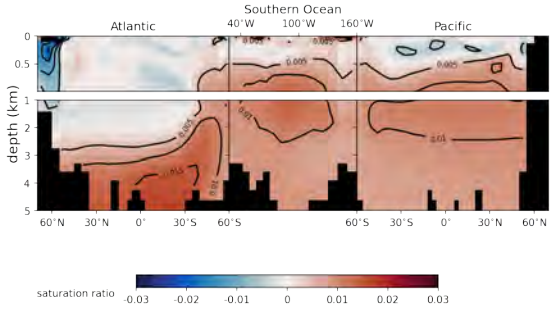

(e) 100% minus 70% wind stress Kr saturation ratio

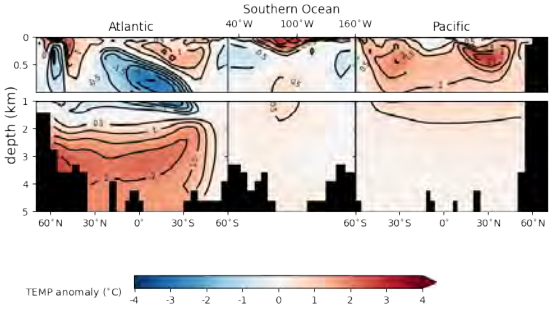

(f) 100% minus 70% wind stress temperature

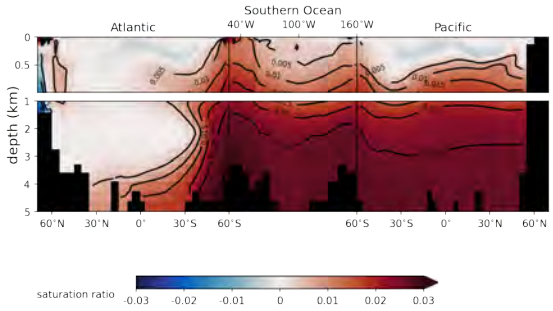

(g) 130% minus 100% wind stress Kr saturation ratio

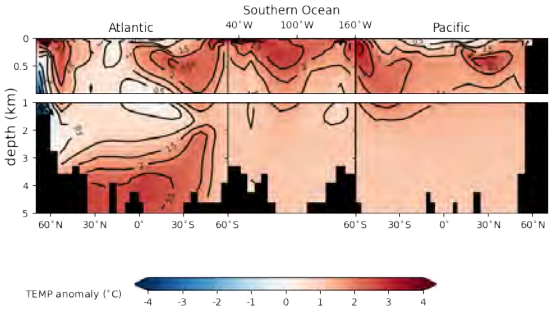

(h) 130% minus 100% wind stress temperature

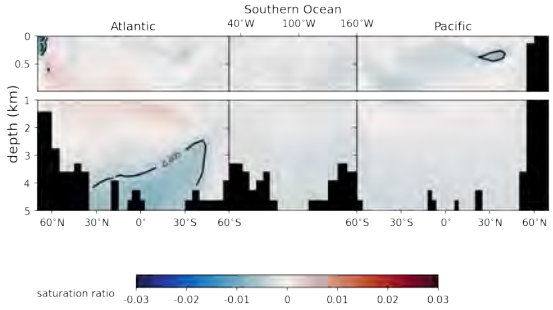

(i) 150% minus 130% wind stress Kr saturation ratio

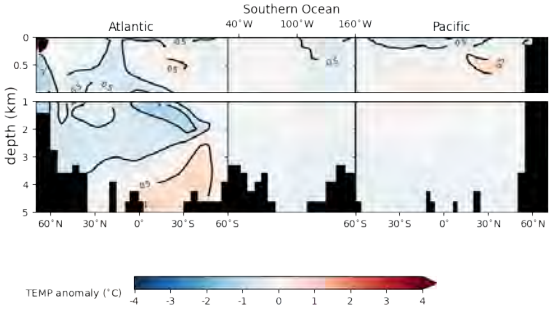

(j) 150% minus 130% wind stress temperature

Figure A4: Change in Kr saturation ratio (left) and temperature (right) by each wind stress change

Declaration of consent

on the basis of Article 30 of the RSL Phil.-nat. 18

Name/First Name: LIU Zhijun

Registration Number: 19-101-401

Study program: MSc Climate Sciences

Bachelor ☐ Master ☑ Dissertation ☐

Title of the thesis: Noble Gases as Mean Ocean Temperature Proxies in Preindustrial and Last Glacial Maximum Simulations

Supervisor: Prof. Thomas F. Stocker

I declare herewith that this thesis is my own work and that I have not used any sources other than those stated. I have indicated the adoption of quotations as well as thoughts taken from other authors as such in the thesis. I am aware that the Senate pursuant to Article 36 paragraph 1 litera r of the University Act of 5 September, 1996 is authorized to revoke the title awarded on the basis of this thesis.

For the purposes of evaluation and verification of compliance with the declaration of originality and the regulations governing plagiarism, I hereby grant the University of Bern the right to process my personal data and to perform the acts of use this requires, in particular, to reproduce the written thesis and to store it permanently in a database, and to use said database, or to make said database available, to enable comparison with future theses submitted by others.

Bern 26,12,2021

Place/Date

Signature